

GROWTH OF 1.5-1.55 μm GaInNAsSb LASERS BY MOLECULAR
BEAM EPITAXY

A DISSERTATION
SUBMITTED TO THE DEPARTMENT OF ELECTRICAL
ENGINEERING
AND THE COMMITTEE ON GRADUATE STUDIES
OF STANFORD UNIVERSITY
IN PARTIAL FULFILLMENT OF THE REQUIREMENTS
FOR THE DEGREE OF
DOCTOR OF PHILOSOPHY

Hopil Bae
March 2009

© Copyright by Hopil Bae 2009
All Rights Reserved

I certify that I have read this dissertation and that, in my opinion, it is fully adequate in scope and quality as a dissertation for the degree of Doctor of Philosophy.

(James S. Harris, Jr.) Principal Advisor

I certify that I have read this dissertation and that, in my opinion, it is fully adequate in scope and quality as a dissertation for the degree of Doctor of Philosophy.

(Robert L. Byer)

I certify that I have read this dissertation and that, in my opinion, it is fully adequate in scope and quality as a dissertation for the degree of Doctor of Philosophy.

(David A. B. Miller)

Approved for the University Committee on Graduate Studies.

Abstract

With the advent of new internet services for exchanging not only texts and pictures but also home-made videos and high-definition movies, the appetite for more internet bandwidth is still growing at a fast pace. Satisfying these demands require extending the high-speed fiber optical networks all the way to the end users. This approach will require high-performance lasers, detectors, and modulators that are also very inexpensive and power-efficient. VCSELs are ideal light sources for this application due to their low power consumption, easier fiber coupling, ease of fabrication, and the possibility of dense 2-D integration.

A new GaAs-based gain material, GaInNAsSb, can be an enabling technology for VCSELs in the 1.3-1.6 μm wavelength range appropriate for optical communications. It can also enable high-power lasers for pumping Raman amplifiers, which can significantly increase the usable bandwidth of optical fibers. Growth of GaInNAsSb by molecular beam epitaxy has been very challenging, but various improvements in growth and annealing conditions have led to very low-threshold 1.55 μm edge-emitting lasers and the first GaAs-based pulsed-mode 1.534 μm VCSELs. Improving their temperature stability and achieving room-temperature continuous-wave(CW) VCSELs was the main objective of this thesis work.

This thesis first discusses additional improvements in annealing and growth conditions, which led to a factor of 4 increase in the peak photoluminescence intensity. Edge-emitting lasers employing different numbers and structures of GaInNAsSb QWs were compared, and the carrier leakage to the GaNAs barriers has been identified to be the dominant source of carrier recombination, by measurements using segmented contacts.

Using the same triple QW structures and carefully designed AlGaAs/GaAs DBR mirrors, the first-ever all-epitaxial near-room-temperature CW VCSELs at 1528nm are realized on GaAs substrates.

Acknowledgement

The work described in this thesis would have been literally impossible without a great many people. First and foremost, I would like to thank my advisor Professor James Harris, also known as "The Coach", for giving me the opportunity to work on this project and showing an example of a good researcher by always being enthusiastic and optimistic about our research and its eventual success. Not only his academic excellence but also his personality is something that I would be really happy to emulate even a fraction of.

I would also like to thank Professors David Miller and Robert Byer for not only taking time out of their busy schedule to serve as readers, but also for teaching me tremendously about quantum mechanics and device physics. I also owe a special gratitude to Professor John Gill for agreeing to serve as my orals chair at the last minute, when most of department professors were out of town on summer vacation.

I would like to thank Mark Wistey, Seth Bank, and Homan Yuen for teaching me the dark secrets of MBE, also known as Mostly Broken Equipments, and training me hard enough to survive the tyranny of the machine on my own. They and Lynford Goddard were kind enough to answer my questions about the MBE machine and the laser testing setup, even years after their graduation. Tomas Sarmiento and Evan Pickett spent a lot of nights with me in our efforts to revive the dead MBE machine for many months on end. I cannot thank them enough for their help. Tomas and I spent so many nights together in the MBE lab and the SNF fab, and nothing could have been possible without him.

I would also like to thank Tomas O'Sullivan for his help with the fabrication of the VCSELs. Without his help, Tomas and I might still be wandering in the fab wondering

what to do with the wafers. I'd like to thank Robert Kudrawiec of Wroclaw University and James Ferguson of Cardiff University for their excellent characterization work of our materials and devices. Sarah Zou of Santur was instrumental in the laser fabrication for her help with wafer thinning, and Ji-Dih Hu of Luxtron provided us with the Photrix pyrometer that has been crucial for our research. Robert Wheeler saved System4 by his excellent UHV welding, thereby also saving our lives, and James McVittie helped us immensely with plumbing and power supply issues when we had to install a new RTA to replace an old one. Leonard Chan, Jose Padilla and Tony Solorzano were very helpful with resolving many issues around the MBE lab. I cannot thank Gail Chun-Creech enough for her help with countless purchase orders, Fedex invoices and other forms.

My friends in the Korean mafia, Joongho, Donghyun, Sangho, Taesang, Jongho, Yangjin, Hyunsik, and Hyunsoo, helped me keep going rather than collapsing under the heavy weight of the MBE machine, by spending time with me at our dorms, on ski slopes and in the CIS lounge.

I would like to thank my parents, without whom I would not be where I am today, for raising me and supporting me through all those years. Lastly, I would like to thank my 5-month-old son Alex Hyungzu and my lovely wife Jin-Kyoung, for providing me with a better motivation than anything else to finish this thesis. In addition, I cannot thank my parents-in-law enough for bringing her to this world, and Pandolnim for introducing her to me.

Contents

Abstract	v
Acknowledgement	vii
1 Introduction	1
2 MBE growth of GaInNAs(Sb)	10
2.1 Molecular Beam Epitaxy for GaInNAsSb growth	10
2.2 RF plasma cell for nitrogen	12
2.3 Photoluminescence	16
2.4 Annealing	19
2.5 Overcoming the Nitrogen Penalty	20
2.5.1 Addition of Antimony	21
2.5.2 GaNAs barrier	22
2.5.3 Impurities in the Nitrogen Beam and the MBE chamber . . .	23
2.5.4 Avoiding ion damage	26
2.5.5 Laser results	27
3 Advances in GaInNAsSb growth	30
3.1 Substrate temperature	30
3.1.1 Bandgap Thermometry	31
3.1.2 Pyrometry	34
3.2 Improvement in annealing conditions	45
3.3 Improvement by Lower group-V flux	52

3.4	Effects of self-annealing	62
4	Edge-emitting lasers	70
4.1	Laser structure	70
4.2	SQW laser performance	71
4.3	Recombination mechanisms	75
4.4	Temperature stability : Theory	80
4.5	Measurement/Origin of nonradiative recombination	84
5	1528nm VCSEL	94
5.1	Structure and design	96
5.2	Growth and fabrication	103
5.3	Measurements	106
6	Conclusion	111
	Bibliography	113

List of Tables

5.1	Shutter operations (o/c for open/closed) and composition grading . . .	102
5.2	Current cell configurations for the two MBE chambers used for this thesis work	103

List of Figures

1.1	Bandwidth usage in Japan [1]	2
1.2	Loss spectrum of optical fibers and CWDM/DWDM wavelengths	3
1.3	Repeater-less transmission distance for different sources	3
1.4	Schematics of an edge-emitting laser vs. a VCSEL	5
1.5	Bandgap versus lattice constant for III-V compounds, including GaInNAs	6
1.6	Illustration of band anti-crossing model	7
1.7	Higher thresholds for longer wavelength(more N) for early GaInNAs lasers, called "Nitrogen Penalty"	9
2.1	Schematic of an MBE chamber	11
2.2	Schematic of the rf plasma cell and nitrogen delivery system	13
2.3	Nitrogen content as a function of growth rate for GaNAs	14
2.4	Trajectories of foreline pressure and reflected power before rf cell rebuild	15
2.5	Improved plasma cell stability after rebuild	16
2.6	Room-temperature PL spectrum of a GaInNAsSb QW surrounded by GaNAs barriers	18
2.7	PL intensity and wavelength vs annealing temperature	19
2.8	PL spectra illustrating the benefits of antimony	21
2.9	Improvement in PL intensity by GaNAs barriers	23
2.10	PL spectra before and after purification of the nitrogen source.	24
2.11	PL improvement by using deflection plates.	26
2.12	Ion current measured as a function deflection voltage.	27
2.13	CW L-I curve and spectrum for the lowest-threshold $1.55\mu\text{m}$ laser.	28
2.14	Pulsed spectrum and L-I curve for a $14\mu\text{m}$ -aperture VCSEL	28

3.1	Peak PL intensity, as a function of postgrowth annealing temperature. Inset shows the peak emission energy (as-grown) at room temperature. From [2]	31
3.2	Reflectivity spectrum for an undoped wafer at various thermocouple temperatures in 50°C steps	32
3.3	Reflectivity spectrum for an n-type wafer at various thermocouple temperatures in 50°C steps	33
3.4	Sensitivity of reflectivity measurement to wafer wobble	35
3.5	Reflectivity of different substrate structures(at 440°C). Also shown is the pyrometer response spectrum, in arbitrary unit.	36
3.6	$1/(e^{\frac{hc}{\lambda kT}} - 1)$ vs. temperature, $\lambda=886\text{nm}$	37
3.7	Pyrometer measurement fluctuations for a 3-inch wafer	39
3.8	Pyrometer measurement fluctuations for a 2-inch wafer	39
3.9	Pyrometer measurement fluctuations for a quarter of 3-inch wafer	40
3.10	Schematic of typical wafers sizes when loaded on the substrate heater	41
3.11	Pyrometer measurement during cool-down and then heat-up, for a quarter of 3-inch wafer	41
3.12	Pyrometer measurement during heat-up, for a 3-inch n-type wafer. Small bumps are due to wafer tilting for easier RHEED observation	43
3.13	Pyrometer measurement during heat-up, for a 3-inch undoped wafer	44
3.14	TC readings at deox in sys4 and at QW growth in sys5	44
3.15	Result of 1-minute annealing at different temperatures for GaInNAsSb QW	47
3.16	PL intensity and wavelength vs. annealing duration for GaInNAsSb QW	48
3.17	PL intensity and wavelength vs. annealing duration for GaInNAsSb QW	49
3.18	PL intensity vs. annealing duration for $\text{Ga}_{0.7}\text{In}_{0.3}\text{N}_{0.012}\text{As}_{0.968}\text{Sb}_{0.02}$ QW.	50
3.19	PL intensity vs. annealing duration for lattice-matched 150nm-thick $\text{Ga}_{0.92}\text{In}_{0.08}\text{N}_{0.02}\text{As}_{0.98}$ layer.	51
3.20	Ga and As equivalent pressures for which segregation-free growth happens for $\text{Ga}_y\text{In}_{1-y}\text{N}_x\text{As}_{1-x}$ [3]	53
3.21	PL results for GaInNAsSb QWs, as a function of the As/III flux ratio	54

3.22	PL results versus Sb flux from [4]	54
3.23	PL intensity for different (As+Sb)/III flux ratios annealed for 1 minute	56
3.24	PL intensity at the optimum annealing temperature vs. (As+Sb)/III flux ratio. Annealed for 1 minute	56
3.25	PL peak intensity(solid circles) and wavelength(open circles) versus As/III ratio [5]	57
3.26	PL wavelength for different (As+Sb)/III flux ratios. Annealed for 1 minute	59
3.27	XRD result for different (As+Sb)/III flux ratios, grown at 440°C . . .	59
3.28	SIMS result for $\times 4, \times 9$, and $\times 15$ (As+Sb)/III ratio growths, at 440°C	60
3.29	PL result for low As+Sb flux growths, after one-minute annealing . .	60
3.30	PL result for low As+Sb flux growths, after long annealing	61
3.31	PL sample and laser structures studied for this thesis	62
3.32	Laser result and PL for high-indium QW	63
3.33	PL intensity and wavelength after self-annealing of plain PL samples	65
3.34	Results of additional ex-situ 1-minute annealing of 41%-In plain PL samples after 0-, 2.5-, and 6.5-hour self-annealing	66
3.35	Results of additional ex-situ 1-minute annealing on "Laser-like" PL samples with 41%-In QW	67
3.36	Results of long-annealing at 620°C on laser-like PL samples with 41%- In QW	68
4.1	Results of long-annealing at 620°C on laser-like PL samples with 41%- In QW	71
4.2	Schematic of the edge-emitting laser.	72
4.3	CW and Pulsed L-I curve for a $2050\mu\text{m} \times 20\mu\text{m}$ laser.	73
4.4	CW spectrum of the a $2050\mu\text{m} \times 20\mu\text{m}$ laser at thermal rollover at a chuck temperature of 15°C	73
4.5	PL intensity versus laser threshold current density [5]	74
4.6	Band offsets of GaInNAsSb/GaNAs QWs	78
4.7	Band offsets of InGaAs/GaAs and InGaAsN/GaAs [6]	78

4.8	Hole distribution at 300K.	80
4.9	Pulsed L-I curve for a $2050\mu\text{m}\times 20\mu\text{m}$ laser.	84
4.10	T_0 for a $2050\mu\text{m}\times 20\mu\text{m}$ laser.	85
4.11	3 different QW structures	86
4.12	T_0 for a thin-barrier laser, $2050\mu\text{m}\times 20\mu\text{m}$	86
4.13	T_0 for a 3QW laser, $2050\mu\text{m}\times 20\mu\text{m}$	87
4.14	T_0 and J_th for all 6 sets of lasers.	88
4.15	Non-radiative current divided by the number of wells.	89
4.16	Non-radiative current divided by total barrier width.	89
4.17	Definition of the absorption edge and transparency point extracted from the modal gain and loss spectra	90
4.18	PL intensity of GaInNAsSb QW for 20nm, 10nm, and 0 GaNAs barrier thicknesses	91
4.19	Two approaches to reduce leakage problem.	93
5.1	Round-trip gain for different number of QWs	97
5.2	Results of the single-pass estimate for scattering loss for laterally abrupt aperture	98
5.3	Conventional PIN, intra-cavity, and tunnel-junction VCSEL structures	100
5.4	Pulsed LI curve for $17\mu\text{m}$ diameter aperture.	107
5.5	Spectrum of a pulsed 1528nm VCSEL at $1.2\times$ threshold.	108
5.6	CW LI curve of a $7\mu\text{m}$ -aperture VCSEL	108

Chapter 1

Introduction

In the early 1990's, people were excited to exchange messages and texts through e-mails and text-based WWW pages. Only 10 years ago, people were happy to exchange high quality pictures and music files over the internet. Now with the advent of new generations of internet services such as YouTube and BitTorrent, people want to share home-made videos, download/watch HD-quality movies, or play online video games. Despite the public notion that the internet boom of the late 1990's ended with a burst bubble, the actual bandwidth consumption has never stopped its exponential increase, increasing by orders of magnitude over the last decade as shown in Fig.1.1 for Japan's case, as consumers' appetite for internet services 'evolved' from text to pictures, and to video. The Discovery Institute, a think-tank, went as far as warning in early 2007 of a coming deluge of data that today's networks are not remotely prepared to handle, and named it 'exaflood', the flood of exabytes (10^{18} bytes, or 1 billion gibabytes). Nemertes, a market-research firm, also warned in November 2007 that user demand for the internet could outpace capacity by 2010 [7].

The most critical part of the internet that needs upgrading is metro-area and local area networks (MANs/LANs) that comprise the last portion of the network connecting individual homes and offices (the so-called "the last mile"), while the optical backbone networks utilizing wavelength division multiplexing (WDM) can provide data rates exceeding terabits per second over a single fiber. Currently, the last mile links, composed of mainly ADSL (Asymmetric Digital Subscriber Line) and

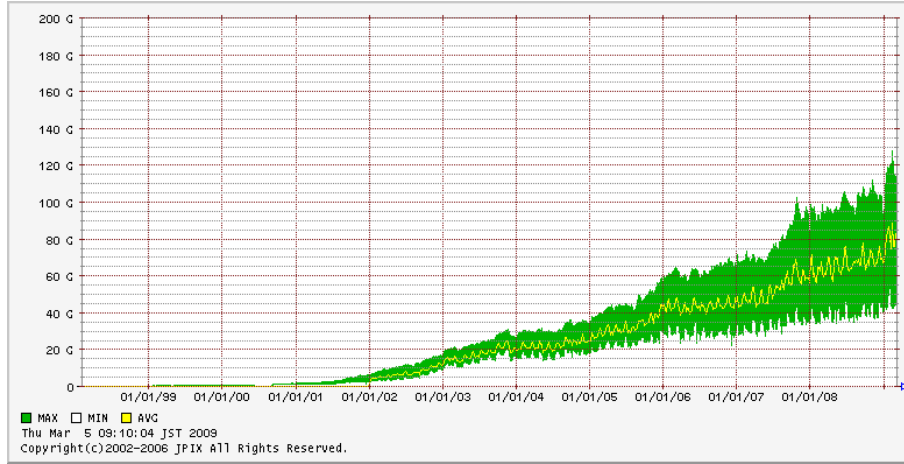


Figure 1.1: Bandwidth usage in Japan [1]

cable internet, present a bottleneck to the end user, as their bandwidth is at most tens of Mbps and degrades even further for longer distances or more users. This issue can be solved by expansion of the optical network all the way to the end users, in an approach generally called FTTx (Fiber To The Home, Premise, Node, Building, Desk, Curb, and so on). Such an approach absolutely requires low-cost and reliable optical components that can send high-speed data over optical fibers, while consuming as little power as possible.

Optical fibers, which are the data transmission medium for optical networks, dictate the wavelength of operation and the kind of optical components that are required. Optical fibers support the highest data rate and the longest distance at $1.3\mu\text{m}$ and $1.55\mu\text{m}$, because of minimum dispersion at $1.3\mu\text{m}$ and minimum attenuation at $1.55\mu\text{m}$, as shown in Fig.1.2. While $1.55\mu\text{m}$ was the clear winner for long-haul links across continents or oceans, $1.3\mu\text{m}$ and $1.55\mu\text{m}$ are both adequate and relatively comparable for MANs or LANs (i.e., a few or tens of kilometers at several tens of Gbps) as shown in Fig.1.3. However, $1.55\mu\text{m}$ is still slightly better and also can benefit from the availability of more advanced optical components that have been developed for $1.55\mu\text{m}$ long-haul links.

While InGaAsP/InP-based Bragg grating and distributed feedback(DFB) lasers

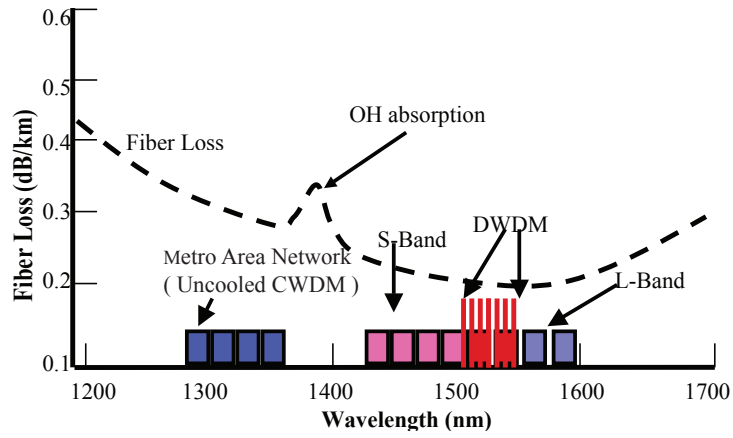


Figure 1.2: Loss spectrum of optical fibers and CWDM/DWDM wavelengths.

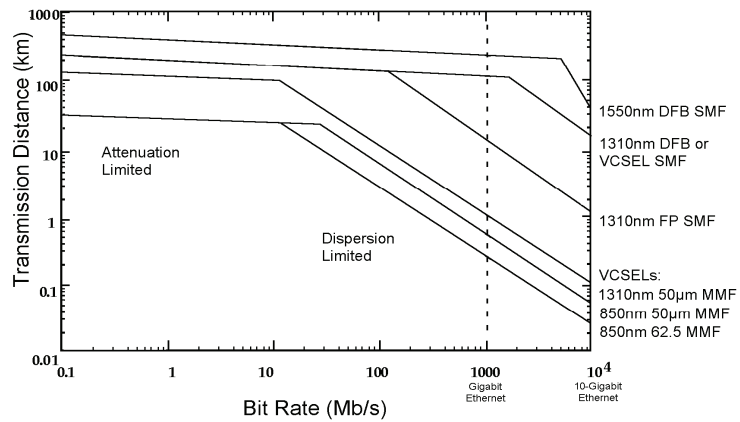


Figure 1.3: Repeater-less transmission distance for different sources

have been the sources for long-haul, $1.55\mu\text{m}$ optical fiber backbone networks for the past three decades and clearly meet the distance criteria in Fig.1.3, their cost is still far too high to meet the demands of hundreds of million lasers that need to be deployed in MANs, LANs, and FTTx in a modern communications network architecture. Vertical-cavity surface-emitting lasers (VCSELs), which amplify and emit light in the vertical direction perpendicular to the wafer surface as shown in Fig.1.4, are ideal for this purpose, as they possess many advantages over traditional edge-emitting Bragg-grating or DFB lasers, such as:

- Low threshold current and low power consumption due to small mode volume
- Single longitudinal mode due to the short cavity length
- Slow change in wavelength with temperature change
- Easier and more efficient coupling into single-mode fibers, reducing alignment/packaging costs
- Simple and robust fabrication, requiring no e-beam lithography, wafer thinning, or facet coating
- High-density 2-D arrays for parallel interconnects
- On-wafer testing before cleaving/packaging, resulting in significant cost reduction in testing and packaging
- More devices per wafer, due to much smaller device foot-print

Despite these advantages, VCSELs at $1.3\text{-}1.6\mu\text{m}$ have been slow in coming. InP-based GaInAsP edge-emitting lasers have been available for decades now, but compatible materials for making good DBR mirrors on InP have been very hard to find. Despite this difficulty, InGaAsP QW based VCSELs have been fabricated using metal mirrors [8], wafer bonded AlAs/GaAs mirrors [9], combined InGaAsP/InP and AlAs/GaAs metamorphic mirrors [10], AlGaAsSb/AlAsSb mirrors [11] and dielectric

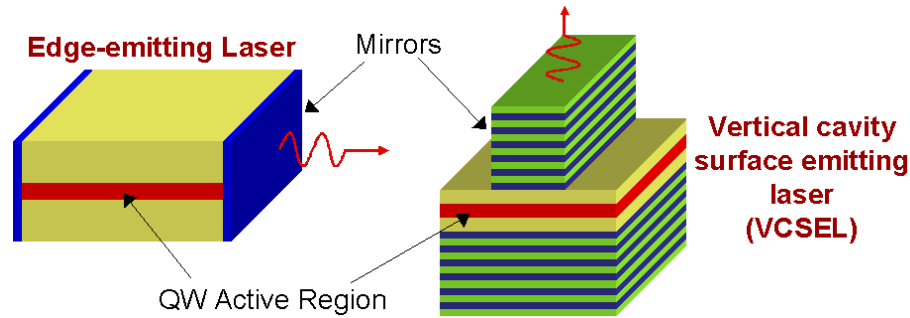


Figure 1.4: Schematics of an edge-emitting laser vs. a VCSEL. The mirrors for an edge-emitting laser can be cleaved/coated facets, Bragg grating, or DFB distributed over the cavity.

mirrors [12]. However, these VCSELs fall short of commercial viability, due to difficulties in growth, poor thermal/electrical conductivity, lack of manufacturability, etc.

On the other hand, the pair of AlAs and GaAs layers grown on GaAs provides an easy-to-grow and reliable (due to lattice-matching) DBR system, with high index contrast, high electrical/thermal conductivities and good electrical/optical lateral confinements by AlAs oxidation. However, realizing a gain material on GaAs substrates that emits at $1.3\text{-}1.6\mu\text{m}$ was challenging, and approaches such as InAs quantum dots [13] and GaAsSb/InGaAs Type II quantum wells [14] had difficulty going over $1.3\mu\text{m}$.

The situation changed when Weyers et al. [15] first reported reduction of bandgap with incorporation of a small amount of nitrogen in GaAs while also reducing the lattice constant, and later, the proposal of GaInNAs by adding nitrogen to InGaAs [16,17] as a new optical gain material for long-wavelength lasers on GaAs substrates. This discovery was far from obvious from the known properties of all other III-V materials, where a smaller lattice constant usually leads to a larger bandgap, as shown in Fig.1.5. By incorporating a proper amount of In (increasing lattice constant and decreasing bandgap) and N (decreasing both bandgap and lattice constant), we can reduce the bandgap much lower than had been possible before, while maintaining relatively small lattice mismatch on GaAs, which is indicated as the vertical line

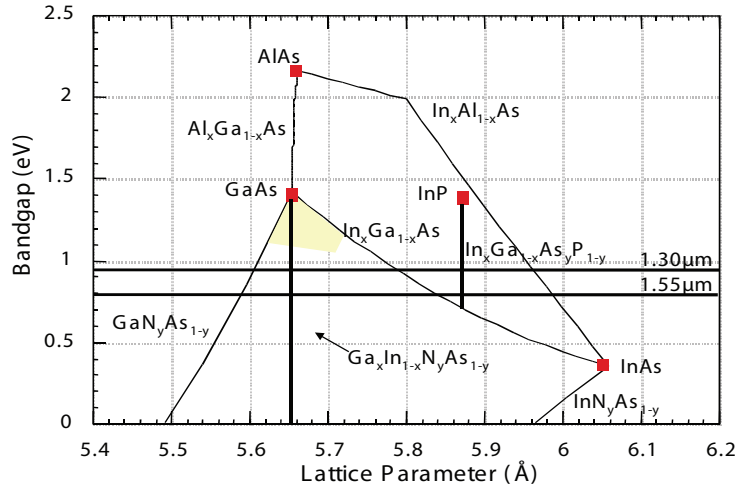


Figure 1.5: Bandgap versus lattice constant for III-V compounds, including GaInNAs

extending downward from GaAs in Fig.1.5.

This unusual bandgap reduction with smaller lattice constant for a small amount of nitrogen incorporation is explained by the band-anticrossing model (BAC) proposed by W. Shan et al. [18]. According to this model, the large electronegativity of N and its small covalent radius cause a localized level within the band structure, which is above the conduction band minimum of GaAs. Strong interaction of this N-level with the GaAs conduction band leads to a splitting of the conduction band into two subbands, with one subband higher and the other lower than the GaAs conduction band, as shown in Fig.1.6. Thus, instead of forming a conventional III-V alloy with a larger bandgap, one achieves a very dramatic decrease in bandgap with a smaller lattice constant. This enables optical gain at 1.3-1.6 μm on GaAs that had not been possible before, opening the possibility of all-epitaxial VCSELs at long wavelengths using AlAs/GaAs DBR technology on GaAs.

Research on GaInNAs has also revealed that it has a larger conduction band offset and a larger electron effective mass than GaInAsP [17, 19], thus providing better confinement for electrons and better match of the conduction and valence band densities of states. This leads to a higher T_0 (better temperature stability), higher operating temperature, higher efficiency and higher output power [20]. This can open up

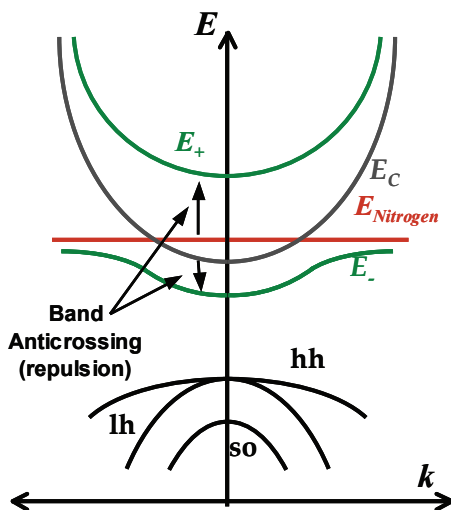


Figure 1.6: Illustration of band anti-crossing model

another possibility of dramatically increasing the usable bandwidth over the optical fibers, by making it possible to use Raman amplifiers instead of the EDFA (Erbium-Doped Fiber Amplifiers) that are currently used to amplify optical signals over dense wavelength division multiplexing (DWDM) systems in the fiber backbone. Raman amplifiers can work over a much wider wavelength range than EDFAs, making it possible to use wavelengths not covered by EDFAs (Fig.1.2 ¹). Wider spectral range covered by Raman amplifiers can allow use of coarse WDM (CWDM), which can eliminate the stringent requirements on wavelength stability and the need for temperature control for the lasers, leading to a significant cost reduction. Alternatively, DWDM can be employed over the wider spectrum, resulting in much higher aggregate data rate over a single fiber. However, good pump lasers for Raman amplifiers in the 1.3-1.6 μm wavelength region have not been available, while 980nm InGaAs lasers have been available for pumping EDFAs. Providing reliable high-power pump lasers for Raman amplifiers in the 1.3-1.6 μm wavelength range is another important motivation for GaInNAs research.

¹DWDM spectrum is limited by spectral coverage of EDFA. Raman amplifiers can cover CWDM wavelengths

While the unique properties of N incorporated in GaAs or InGaAs provide promising new possibilities for semiconductor lasers at 1.3-1.6 μm , its unique properties also posed challenges for the growth of GaInNAs. The most important challenge was the very low solubility of nitrogen into InGaAs matrix. This is due to the different basic crystal structures of the constituent alloys and their regions of growth compatibility: InGaN is a hexagonal (wurtzite) crystal grown at relatively high temperatures while InGaAs is a cubic (zincblende) crystal grown at relatively low temperatures, creating a miscibility gap in the alloys [21–23]. When the N concentration or growth temperature increases, phase segregation occurs and the material breaks up into microscopic regions of InGaAs and InGaN. In the case of MOVPE(Metal-Organic Vapor-Phase Epitaxy) growths, there were additional difficulties with low cracking efficiency of ammonia or arsine, complex precursor reactions, highly non-linear incorporation ratios [24–27], or carbon and hydrogen contamination [25, 28]. MBE(Molecular Beam Epitaxy) also had its own challenges, such as strong sensitivity to growth temperature [2] or ion damage from rf plasma cell [29], among other things. These growth challenges become significantly more severe, as more nitrogen is added to increase the wavelength. This difficulty was initially called 'the nitrogen-penalty', where longer wavelength GaInNAs lasers with more nitrogen (and more indium) exhibited significantly higher threshold current densities as shown in Fig.1.7.

Despite the challenges, immense progress has been made through intense efforts from several research groups, and high-performance GaInNAs lasers have been realized in the 1.3-1.6 μm wavelength range. For the 1.3 μm range, edge-emitting lasers have been reported with room-temperature threshold current densities as low as 150-300A/cm² per QW for MQW lasers and 250–320A/cm² for SQW lasers [30–35], along with T_0 values over 100K [36–39] and high output power of >8.9W [40]. Room-temperature continuous-wave(CW) VCSELs with low threshold, high output power, high-speed direct modulation and high reliability have also been realized at 1.3 μm [41–50]. 1.55 μm lasers have proven to be far more challenging than 1.3 μm lasers, but we have succeeded in realizing very low threshold (318A/cm² pulsed, and 373A/cm² CW) and high-power(>1W pulsed, 430mW CW) lasers at 1.5 μm [51] and 1.55 μm [52].

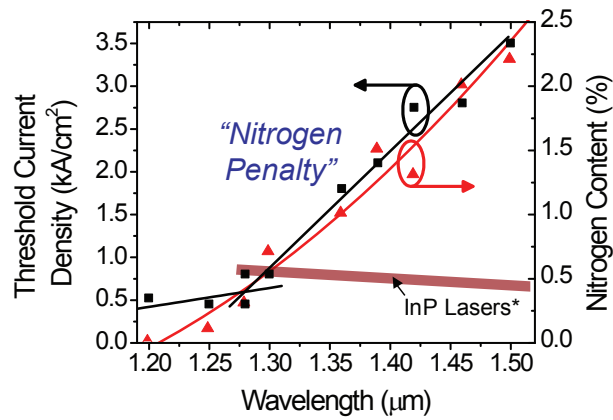


Figure 1.7: Higher thresholds for longer wavelength (more N) for early GaInNAs lasers, called "Nitrogen Penalty"

However, the realization of high temperature stability of edge-emitting lasers and room-temperature CW VCSELs for 1.55μ wavelength range have been quite challenging and elusive. T_0 for 1.55μ lasers has been rather low ($\sim 60\text{K}$) especially for low-threshold lasers [52], and 1.55μ VCSELs have been limited to pulsed operation at sub-zero temperatures [53, 54]. These two goals have been the main concerns of this thesis work. This thesis discusses the basics and recent improvements in the MBE growth of GaInNAs(Sb)², edge-emitting laser results and the origin of poor temperature stability, and the first near-room-temperature CW VCSELs at 1528nm on GaAs.

²For 1.55μ lasers, Sb is also incorporated to make GaInNAsSb, for reasons to be discussed in the next chapter

Chapter 2

MBE growth of GaInNAs(Sb)

MBE(Molecular Beam Epitaxy) is used for growth of GaInNAs(Sb) QWs and lasers reported in this thesis. This chapter provides a primer of the MBE technique and the growth improvements that have led to the first VCSELs and the best edge-emitting lasers near $1.5\mu\text{m}$. This chapter is meant to be a short review and to compliment the many excellent works of previous students [3, 55–59], so only essentially necessary or new information is presented here. "GaInNAs(Sb)" is used to include both GaInNAs and GaInNAsSb materials, and the reason of including Sb is explained in this chapter.

2.1 Molecular Beam Epitaxy for GaInNAsSb growth

Molecular beam epitaxy system is essentially a highly sophisticated thermal evaporation system. A schematic of an MBE chamber is shown in Fig.2.1. The MBE growth of semiconductor films takes place by the reaction of molecular beams of the constituent elements with a crystalline substrate surface held at a suitable substrate temperature under UHV conditions. The molecular beams are generated from sources contained in ceramic crucibles (typically pyrolytic boron nitride, or PBN), called effusion cells. The molecular beam flux intensity is accurately adjusted by the temperature within the effusion cell. To initiate or terminate the molecular beam flux of an individual effusion cell, each source is equipped with an externally controlled mechanical shutter. By opening/closing the shutters in proper sequences, complex

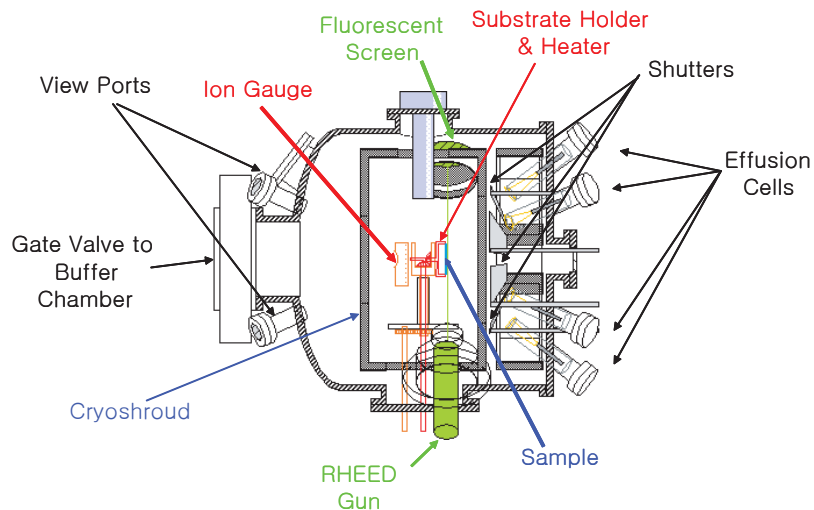


Figure 2.1: Schematic of an MBE chamber

multilayer heterostructures can be grown with high precision.

Because MBE growth is conducted under ultra high vacuum (UHV, $\sim 10^{-10}$ torr), the level of residual gas in the chamber and contaminant incorporation is very low. The low pressures also lead to long mean free paths for the source atoms. As a result, there are no precursor interactions. The substrate surface is thermally isolated from the rest of the chamber and the effusion cells, so the physical and chemical reactions on the substrate surface are solely determined by the substrate temperature, independent of the growth rates. Stoichiometric compound semiconductors are quite straightforward to grow by MBE, because at typical MBE growth temperatures, the group-III sticking coefficient is much higher on a group-V terminated surface than on a group-III terminated surface. Likewise, group-V elements stick to a group-III terminated surface much more strongly than to a group-V terminated surface [60]. MBE growth of III-V compound semiconductors is usually done under a high group-V flux with the lower group-III flux controlling the growth rate. These properties of MBE dramatically simplify growth compared to the competing MOVPE technique, where high-precision growth control and high quality growth require much more work due to high carbon/hydrogen levels and complex interactions between precursors in

the gas phase and on the substrate surface. Therefore, it is the preeminent growth technique for pioneering new materials and devices, which also has been true for GaInNAs. The first GaInNAs study and the first GaInNAs VCSEL near $1.3\mu\text{m}$ were realized using MBE [17], although with gas sources which caused some complications from H incorporation [61, 62]. The best edge-emitting lasers and the first VCSEL were all realized using MBE growth [52, 53].

2.2 RF plasma cell for nitrogen

Nitrogen needs special attention for MBE growth of GaInNAs(Sb), because the most abundant source of nitrogen on earth - nitrogen gas - is a very non-reactive substance, which is often treated as 'inert' for many practical purposes, including many semiconductor fabrication processes. A more reactive source of nitrogen has to be provided for GaInNAs(Sb) growth. Nitrogen-containing gases such as U-dimethylhydrazine (U-DMHy) or ammonia, which are often used for MOVPE growth, can be considered, but complications due to carbon/hydrogen incorporation or low cracking efficiency make this approach rather undesirable [62, 63]. On the other hand, a nitrogen plasma is employed to provide a reactive nitrogen species for GaInNAs(Sb) growth.

For our group and many other research groups, RF plasma cells have proven to be the simplest and most effective system to grow GaInNAs(Sb) using MBE [5, 52, 64–67]. By contrast to RF plasmas, electron cyclotron resonance(ECR) [68] and dc plasmas [69] were found to generate more ions and generally produce dilute-nitride material of poorer quality [56].

We used a RF plasma cell from SVT associates. The setup of the plasma cell is shown in Fig.2.2. The plasma was operated in an inductively-coupled mode (high-intensity mode) to more effectively generate reactive species. The plasma conditions are mainly determined by the pressure in the crucible and the rf power. Generally, higher pressures or lower powers tend to decrease the ion count and the ion energy, but also the dissociation efficiency. Lower pressures or higher powers, on the contrary, can increase the dissociation efficiency at the cost of more damaging ions. The optimum points can be found by experiments [70], but the plasma conditions are

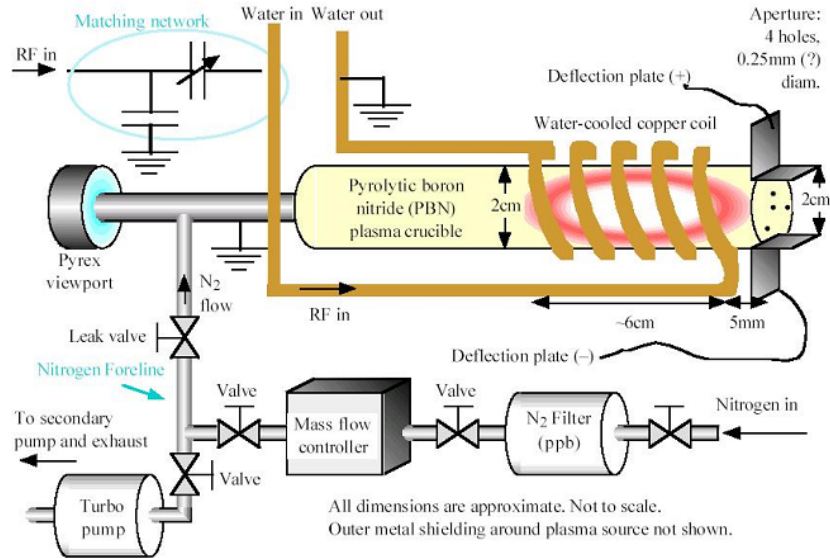


Figure 2.2: Schematic of the rf plasma cell and nitrogen delivery system

very complex and depend on a variety of competing mechanisms. Slight change in the nitrogen flux (therefore pressure in the crucible) or the rf power can change the plasma characteristics and the grown GaInNAs quality significantly in unpredictable manners, so it was decided that it is the best practice for repeatable high quality growth to keep the plasma conditions constant and vary the group-III rates to incorporate different amounts of nitrogen [56]. This was not as severe a limitation as it might sound, because it has been found that the nitrogen incorporation is inversely proportional to the growth rate [3,23], as shown in Fig.2.3. This means nitrogen has a unity sticking coefficient on the substrate surface, and therefore behaves like a group-III element as long as the amount of nitrogen incorporation is small. This finding greatly simplified GaInNAs(Sb) growth and truly enabled the early rapid progress at Stanford University.

However, MBE growth of GaInNAs(Sb) using the RF plasma was still not a straightforward proposition, one of the most annoying problems being the instability of the plasma cell. The nitrogen foreline pressure (indicative of the plasma pressure, despite not being its direct measure) and the reflected rf power are the two easiest

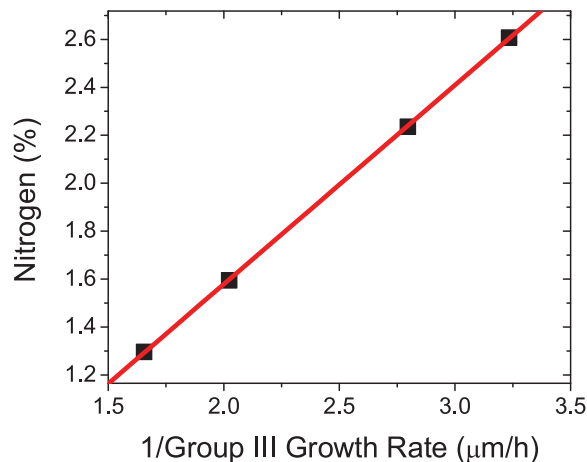


Figure 2.3: Nitrogen content as a function of growth rate for GaNAs

parameters to monitor for the plasma conditions, and they showed a very rapid change during the first hour of plasma operation, as shown in Fig.2.4. Moreover, the plasma would sometimes refuse to ignite at all or become extinguished in the middle of a growth for no apparent reason. This instability in the plasma conditions added some grievance and one more parameter to optimize in our efforts to find the best way to control the plasma cell. Various measurements, such as optical spectrum of the plasma and ion energy/count measurements, were conducted [56], and many samples were grown and compared to determine when the plasma was in its best condition, but the results were inconclusive. The origin of the instability was also not clear, although thermal effects on the crucible or the capacitor in the matching network were suspected [56]. An in-depth analysis was presented in [56] based on the hypothesis that a large drift in the capacitor temperature is the main cause of this instability problem, but later measurements showed that the capacitor temperature is very stable within 2-3°C, thus disproving the capacitor temperature hypothesis.

Part of this instability problem was resolved when the rf cell was repaired after producing low-quality materials for many months. With the repair, a significant change was made to the configuration of the crucible. Before the repair, the crucible was an open-ended cylinder with a separate aperture plate (thin and coin-shaped)

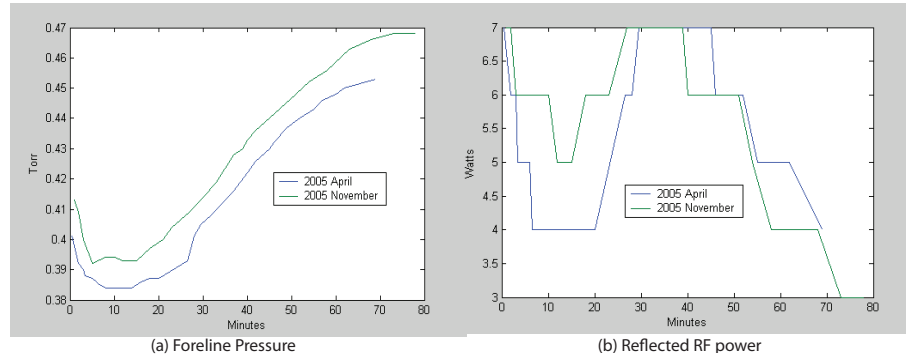


Figure 2.4: Trajectories of foreline pressure and reflected power before rf cell rebuild. The cell was rebuilt in mid-2006, so both lines are before the rebuild.

held in place between the crucible and the deflection plates. After the repair, a new crucible with the aperture plate now integrated as part of the crucible was installed. This resulted in a significant improvement in the cell stability, reaching steady-state within 20 minutes rather than drifting for over 1 hour, as shown in Fig.2.5. The new crucible also required much less nitrogen flow rate (only 0.115 sccm, compared to 0.5 sccm) for comparable plasma conditions and foreline pressures. Therefore, it seems that much of the instability was due to the mechanical drift of the separate aperture plate under temperature and pressure variations. We also found that as long as we kept the same foreline pressure as before, the nitrogen incorporation in and the optical quality of GaInNAs(Sb) were essentially the same, comparing samples before and after the installation of the new crucible. This was a welcome news for us in that it proved that the foreline pressure is actually a very good indicator of the plasma conditions, and the research can be continued without restarting everything from scratch, with a more stable plasma cell, despite a major equipment modification in the course of the research.

2.3 Photoluminescence

PL has been the most important characterization technique for the research of high-quality of GaInNAs(Sb) growth, so it deserves special mention in this chapter. Other

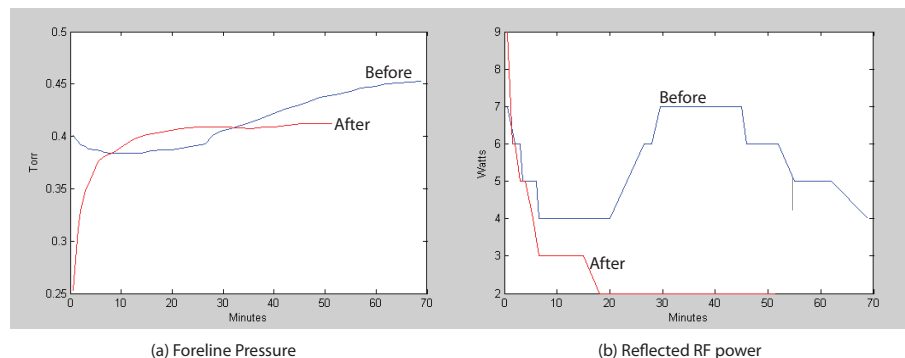


Figure 2.5: Improved plasma cell stability after rebuild

measurements such as XRD(X-Ray Diffraction), TEM(Transmission Electron Microscopy), and SIMS(Secondary Ion Mass Spectroscopy) were also used. SIMS mainly measures the compositions of the main constituent elements and some impurities in the grown films, XRD measures the crystalline quality, the strains and the composition, and TEM can take a real-space image of the actual atoms in the crystal, enabling us to directly see the defects, compositional fluctuations, interface quality, etc. These methods were all important, but PL was by far the most often used technique (i.e., for each and every sample after growth, rather than a few select samples for other techniques) and also the most sensitive to opto-electronic properties. Simply put, good quality indicated by XRD, TEM, or SIMS does not guarantee a good PL result, while a good PL result most probably means high crystalline quality and low level of impurities. More importantly, the PL result and laser performance have shown very strong positive correlation [5, 52], and many growth improvements discussed in this chapter were first identified by PL measurement and later corroborated by actual laser results. Therefore, only the PL technique is presented in this section, and the reader is referred to previous theses from our group for the details of other techniques [3, 56–58].

The PL technique consists of an incident pump beam with photon energy larger than the bandgap of the material being studied. The pump generates electron-hole pairs in the semiconductor. They quickly(~ 0.1 ps) thermalize to the lowest energy of their respective bands. The carriers then diffuse and eventually recombine, emitting

a photon close to the bandgap energy. However, the carriers may recombine in other ways than emitting a photon, most notably, through Shockley-Read-Hall(SRH), or defect recombination. Higher quality of the material would therefore lead to more recombination occurring radiatively, while lower quality material would lose a significant number of carriers through defect recombination. So the intensity of the radiative emission correlates positively with the material quality, and serves as an indicator of quality.

The PL setup employed in this work uses a chopper to modulate the pump laser (which was initially an Argon laser and later replaced with a 532nm frequency-doubled semiconductor laser). The emission signal passes through a monochromator to select a specific wavelength, and is then detected by a photo-detector. The detector signal is fed to a lock-in amplifier for maximizing the signal-to-noise ratio. As the wavelength response of this setup is not flat due to the spectral responses of the detector and the monochromator grating, each PL measurement is normalized by dividing by the system response, which was measured from the system response to a white light source. The PL measurement results also showed run-to-run variations due to day-to-day variations in the pump laser power, alignment, and so on, so a standard sample was measured for every run and the results were normalized with respect to the peak PL intensity of the standard sample.

The main parameters of interest for PL measurements are the wavelength of peak intensity, peak intensity, and linewidth. The wavelength of peak intensity is obviously of great interest, as it is quite close to the bandgap and where lasing would occur with such an active layer. Peak intensity is an excellent indicator of the optical quality of the material. The lower the defect density, the stronger the peak PL signal. Caution has to be exercised in comparing the peak PL intensities of different samples, however, because the peak PL intensity provides only a relative measure of the material quality, in that the peak intensity can be different even for the same quality material if its surrounding layers are of a different structure or quality. However, peak PL intensity has served as an excellent predictor of laser performance over several generations of lasers at Stanford as well as other research groups [5], as long as the same test structure is used over all the samples being compared. The linewidth is an indicator

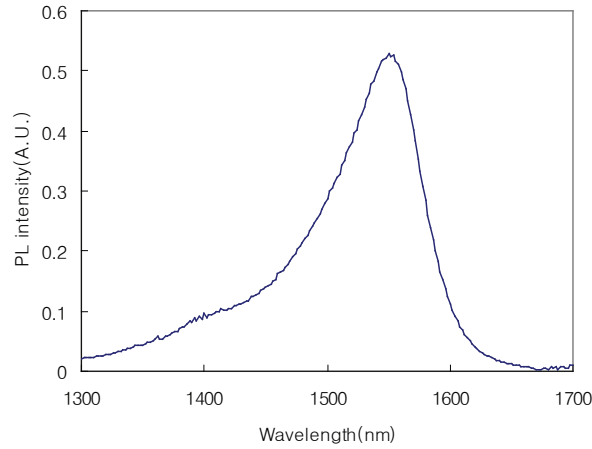


Figure 2.6: Room-temperature PL spectrum of a GaInNAsSb QW surrounded by GaNAs barriers

of broadening due to interface quality and alloy disorder. As low quality growth would lead to rougher interface and less uniform alloy, the linewidth was also considered as a possible predictor of laser performance, where a narrower linewidth would predict a better laser. However, for the recently grown high-quality samples, the linewidth did not predict laser performance as reliably as the peak PL intensity. The PL linewidth is not a straightforward measure of interface quality or alloy disorder either, because the linewidth may increase a little bit for a higher quality sample as higher energy states are filled to accommodate a larger number of carriers. One could lower the PL pump power until only the lowest-energy transition is visible, but a more straightforward way to probe the interface quality or alloy uniformity would be to use a photo-reflectance(PR) or contactless electro-reflectance(CER) measurement where the optical transition levels in the material are probed through the absorption process rather than emission, which does not require filling of the energy levels with carriers [6, 71].

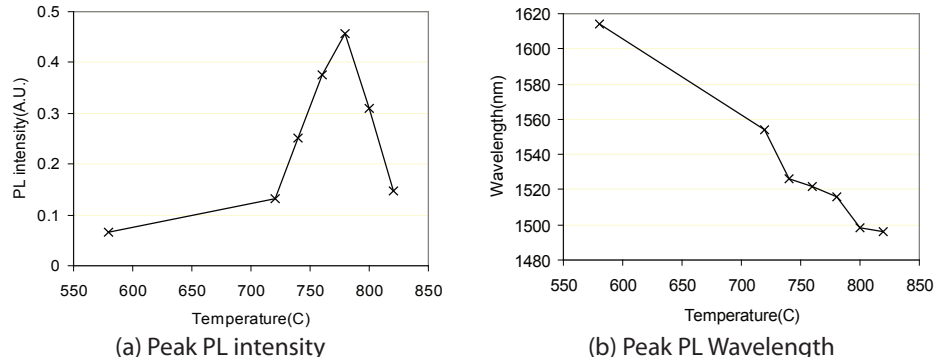


Figure 2.7: PL intensity and wavelength vs annealing temperature. 580°C represents 'no anneal'.

2.4 Annealing

Annealing has been an integral part of GaInNAs(Sb) research from the early days [27, 28, 72]. Annealing of GaInNAs(Sb) has two major effects on its properties: increase in the optical quality (measured by PL) and blueshift in the peak PL wavelength.

Many defects are formed during growth of GaInNAs(Sb), which is believed to result from the low growth temperature required to incorporate N and In, and the damage due to energetic species in the nitrogen plasma. A 60 second anneal in an RTA (Rapid Thermal Anneal) chamber has been typically employed by our research group, obtaining a significant PL intensity increase compared to the un-annealed sample as shown in Fig. 2.7. Researchers have identified many types of defects and their behavior when annealed. Among the most prominent are nitrogen split interstitials (two nitrogen on one group-V site, or $(N-N)_{As}$), and arsenic-nitrogen split interstitials $(As-N)_{As}$, giving rise to various electron and hole trap levels in the material [73–75]. Another important defect is arsenic anti-sites (an arsenic atom on a group-III site, or As_{Ga}), due to the low growth temperature and high arsenic flux. Presence of this type of defects can be supported by the significant improvement in luminescence efficiency and laser performance when lower arsenic flux was used for growth, as reported by the Infineon group [5] and by our group [76] and described in Section 3.3 of this thesis.

It is worth noting that PL intensity improves with anneal up to a certain temperature, above which the intensity starts to fall again. Various mechanisms have been proposed as a cause(s) of this behavior, such as arsenic vacancies diffusing from the surface or elsewhere in the substrate, outdiffusion from the QW [77], strain relaxation, or phase segregation [56]. It is found for our GaInNAs(Sb) QWs that this quality drop under over-annealing has a rather large activation energy ($\sim 7\text{eV}$) which may indicate an extended type of defect, such as dislocations. A very similar annealing behavior was observed for two samples with vastly different cladding structures but with the same QWs, which can be evidence against the importance of arsenic vacancies in the over-annealing mechanism. More will be discussed in Chapter 3.

The other major effect of annealing GaInNAs(Sb) is the blueshift of the peak PL wavelength, as shown in Fig.2.7. The origin of the blueshift was attributed to various mechanisms, such as nitrogen outdiffusion [3, 23, 78], In/Ga interdiffusion [79–81], and localized depressions in bandgap [82–84] due to nitrogen clusters or point defects that are removed with anneal. Later research indicates that changes in the nearest-neighbor configuration of nitrogen during annealing can explain the majority of this blueshift, when gallium and indium atoms trade places so each nitrogen is surrounded by more indium atoms, in order to reduce the local strain and the total energy of the lattice [85, 86]. One source of discrepancies between groups as to the origin of the blueshift was the presence or absence of vacancies in the crystal. It has been shown that intentional introduction of vacancies in the crystal causes more interdiffusion of atoms and thus more blueshift [87–89]. Thus, it is expected that the best quality material should demonstrate the least blueshift with anneal. The GaInNAs(Sb) QWs grown by our group and used in the low threshold $1.5\mu\text{m}$ and $1.55\mu\text{m}$ lasers indeed show very negligible blueshift, apart from the initial large blueshift due to the nitrogen nearest-neighbor reconfiguration (See Fig.3.16).

2.5 Overcoming the Nitrogen Penalty

As described in the previous chapter, there was initially a significant degradation in the material quality and increase in the laser threshold, as researchers tried to

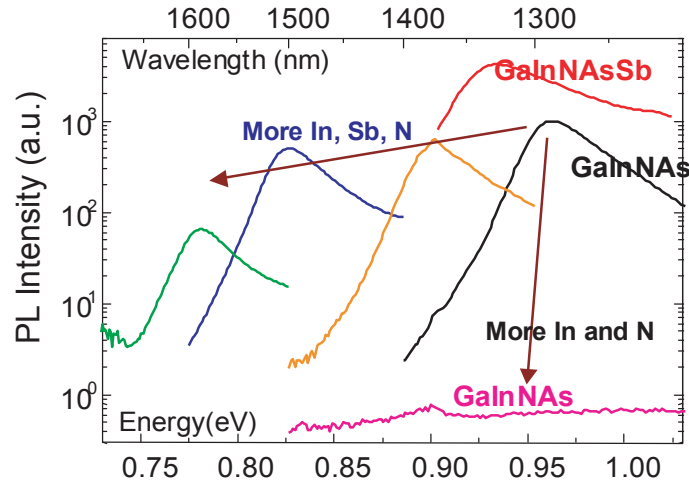


Figure 2.8: PL spectra illustrating the benefits of antimony

increase the wavelength by increasing nitrogen and indium content in GaInNAs. This section briefly describes important breakthroughs that enabled low-threshold room-temperature continuous-wave edge-emitting lasers at $1.55\mu\text{m}$ [52] and the first all-epitaxial GaAs-based VCSELs at $1.46\mu\text{m}$ and $1.534\mu\text{m}$ [53, 54].

2.5.1 Addition of Antimony

The quality of GaInNAs showed rapid degradation going beyond $1.3\mu\text{m}$ with more In and N added to increase the wavelength [27, 28, 45, 78]. Addition of antimony was found to solve this problem, enabling high quality growth for higher In and N contents, as illustrated in Fig.2.8. Antimony acts as a reactive surfactant, which reduces the surface diffusion length by occupying substitutional sites [90]. This reduction of the surface mobility suppresses phase segregation and roughening, allowing growth at higher temperatures. Higher growth temperature enables growth of higher quality material with fewer point defects.

In addition to acting as a reactive surfactant, Sb was also found to incorporate into the alloy (on the order of a few percents), which helped further reduce the bandgap. GaInNAsSb QWs, which are obtained by adding Sb to GaInNAs, have been essential for realizing high performance edge-emitting lasers and the first VCSELs at $1.55\mu\text{m}$

by our group [52, 54]. It is also possible to reach $1.5\mu\text{m}$ without using Sb, but the laser thresholds were significantly higher than achievable with GaInNAsSb [5].

Another interesting effect of antimony is that it increases the nitrogen incorporation rate by about 50%, due to its properties as a reactive surfactant [91, 92] and its large atomic size, making more room for N to incorporate without increasing the lattice free energy too much. Probably due its large size, antimony tends to compete against indium for incorporation, despite one being a group-V element and the other a group-III element [93]. Lastly, there exists an optimal flux of antimony for the best quality growth: the Sb flux has to be sufficiently high to provide surfactant effects, but not too high to reduce the surface diffusion length too much, degrading the optical quality of the material [93].

2.5.2 GaNAs barrier

Use of GaNAs barrier layers was another important step toward achieving high-quality GaInNAs(Sb) QWs. For 1.3-1.55 μm emission, GaInNAs(Sb) has a rather high concentration of indium(30-40%), which results in quite high compressive strain in the QW ($\sim 2.5\%$ for 1.55 μm QWs) even with the lattice constant reduction from N incorporation. Use of GaNAs barriers was proposed as a way to compensate this high compressive strain, by providing an opposing tensile strain below and above the GaInNAs(Sb) layer [3, 23, 79, 94]. The effect of GaNAs barriers on the peak PL intensity is shown in Fig.2.9. GaNAs barriers lead to roughly 4 times higher PL intensity compared to GaAs barriers. In addition to improving the quality of a GaInNAs(Sb) single QW, strain compensation provided by GaNAs barriers also helps with growing multiple QWs. Up to 3 QWs have been grown with high quality, which were actually used for the VCSEL results of our group [53, 54, 95], while SQWs were used for high performance edge-emitting lasers [52, 96].

GaNAs was also helpful in extending the emission wavelength, because it has a smaller bandgap than GaAs. Lower barrier energy leads to lower QW confinement energies, resulting in longer emission wavelength. It was also initially proposed that GaNAs can act as a reservoir of nitrogen, which can reduce the blueshift due to

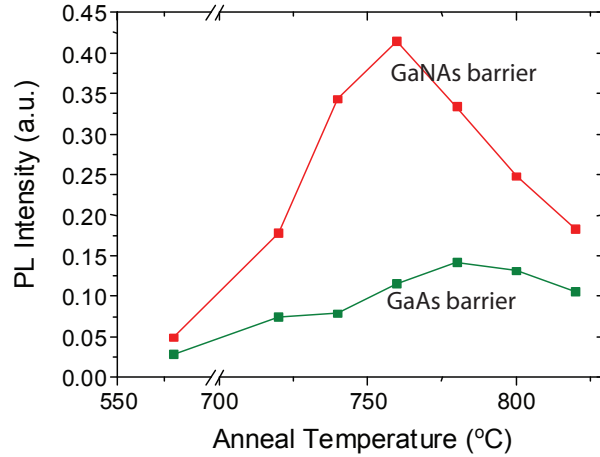


Figure 2.9: Improvement in PL intensity by GaNAs barriers

the nitrogen outdiffusion from GaInNAs(Sb) [23], but this effect seems to be less important for later high-quality GaInNAs(Sb) growths.

Although GaNAs has been one of the enabling factors for $1.55\mu\text{m}$ GaInNAs(Sb) lasers, now it is turning out to be a performance bottleneck. While GaNAs barriers improve the quality of GaInNAs(Sb), the quality of GaNAs itself remains relatively poor with a high concentration of point defects [73, 92, 97]. The small bandgap of GaNAs also means smaller band offset between GaInNAs(Sb) and GaNAs layers, resulting in more carriers in the GaNAs barriers when compared to GaAs barriers. The unfortunate combination of low quality and low band offset leads to significant carrier loss in the GaNAs layers, unnecessarily increasing the laser threshold and also degrading the temperature stability of the lasers. A new barrier design is necessary that can solve this problem while retaining the advantages of strain compensation. More details about this issue are presented in Chapter 4.

2.5.3 Impurities in the Nitrogen Beam and the MBE chamber

The background pressure (10^{-10} torr) and the fluxes of source elements (on the order of 10^{-7} torr measured by an ion gauge) are very low in MBE, so even a barely

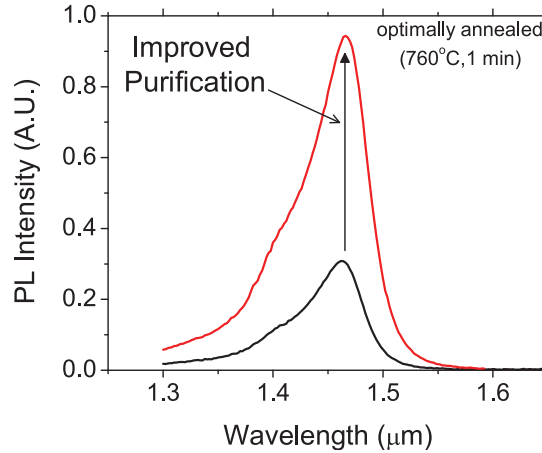


Figure 2.10: PL spectra before and after purification of the nitrogen source.

detectable quantity of contaminants can result in significant levels of impurities in the grown material. Therefore, minimizing background contaminants (such as H_2O , O_2 , CO_2 , and other hydrocarbons) in the MBE chamber is of paramount importance for growing high quality materials. As GaInNAS(Sb) growth requires a nitrogen plasma source, the nitrogen source gas has to be very clean too. Although 5N(99.999%) high-purity nitrogen gas is used as the source, 0.001% impurity in the nitrogen beam can lead to a high level of impurities in the crystal when nitrogen is incorporated at the concentration of several 10^{20}cm^{-3} . Deliberate care was taken to remove impurities from the nitrogen beam, by installing a part-per-billion purifier, carefully baking the nitrogen delivery lines, and fixing a leak in the pumping system. This resulted in a significant improvement in the PL intensity, as shown in Fig.2.10. Impurity levels were checked using a residual gas analyzer installed on the growth chamber, to make sure oxygen and water levels are below the detection limits, every time a major maintenance or modification work was performed on the chamber, especially when the rf plasma cell was rebuilt.

Maintaining low background pressure in the MBE growth chamber is also very important, without which one cannot embark on any meaningful growth experiments. Although this is a conceptually simple task, in practice it is arguably the most important and the most time-consuming aspect of MBE growth research, requiring days

and weeks of repairs, bakes, and leak checking, although it does not merit much discussion in a thesis. However, one particular problem that plagued our MBE chamber¹ for a decade or so is worth describing. The chamber pressure would rise to 10^{-7} or 10^{-6} torr at a random moment for no apparent reason. The high pressure would stay for a few minutes, and then drop abruptly down to the 10^{-10} torr range. This problem was dubbed quite appropriately as "System5 burps". The origin of and the solution of this burping problem was not found over many generations of students, although some hypotheses were proposed, such as permeation of cooling water and ethylene glycol through the stainless steel wall of the source cooling panel. This problem was eventually found to be due to a clogging at the liquid nitrogen valve, which sits between the liquid nitrogen reservoir in the ceiling of the laboratory room and the cryoshroud in the MBE chamber². Due to the clogging, the cryoshroud would be insufficiently filled, leading to less effective pumping action and slow rise in the chamber pressure, and then a rapid decrease when liquid nitrogen suddenly flows into the cryoshroud with a refill of the reservoir. This problem was permanently resolved by emptying the liquid nitrogen system completely and drying the whole system with dry air, which probably removed small particles of dust or ice that were deposited at the valve.

The most troublesome implication of the burp problem is that some of previous experiments might have been affected by one of these burps. Since System5 burps would manifest themselves at random moments without any warning, there was always some uncertainty whether low optical quality of a particular sample was a real meaningful result or just a victim of a burp³. Although we believe previous experiments were properly analyzed taking any possible 'burp victims' into account, one needs to stay open-minded and prepared for any surprise findings that contradict

¹This problem was persistent in System5, which is dedicated for GaInNAsSb growth, while the other System4 is dedicated for AlGaAs cladding and DBR growths. Two chambers are needed because of limited number of source materials per chamber, and also the advantage of separating Al and N cells

²The cryoshroud filled with liquid nitrogen acts as a large and effective vacuum pump by adsorbing gas molecules onto its outer surface.

³We do not monitor the chamber pressure during growth, to minimize contaminant outgassing from the ion gauge and also to maximize the life span of the ion gauge, which is inversely proportional to the chamber pressure.

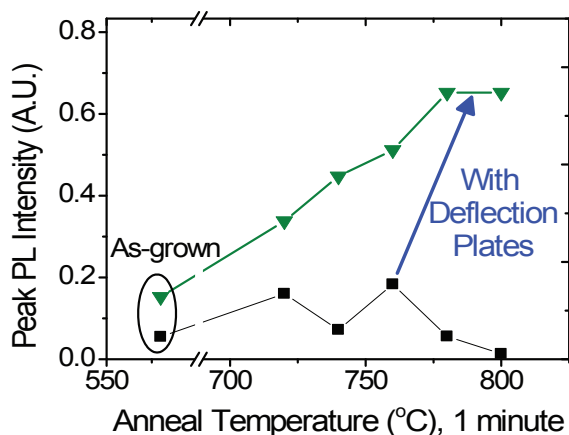


Figure 2.11: PL improvement by using deflection plates.

previous experiments performed when the burps were still present.

2.5.4 Avoiding ion damage

Although a rf plasma cell was found to produce fewer ions than other types of plasma cells, there are still a significant number of ions generated in a rf plasma cell. The energy distribution of ion and electron currents from the plasma were measured by Wistey using the chamber ion gauge as a remote Langmuir probe [56, 98]. It was found that electrons have energies up to 8eV, and the electron current was about 4nA. Ions were found to have energies up to 35eV, with the total ion current of ~ 1 nA.

To see the effect of ion removal from the plasma output, metal plates were installed at the exit aperture of the nitrogen plasma cell. One plate was grounded and the other was biased. From the calculation based on the measured ion energies and also by PL measurements on samples grown with different deflection voltages, it was found that 20V is sufficient to deflect the ions away from the wafer, and the PL intensity was uniformly high for +100, +15, and -40V, whereas 0V resulted in poorer PL intensity as shown in Fig.2.11. Ion count measurements for different deflection voltages agree with this result, too, as shown in Fig.2.12. On the other hand, the PL wavelength did not change much with the application of deflection plates, which implies that nitrogen

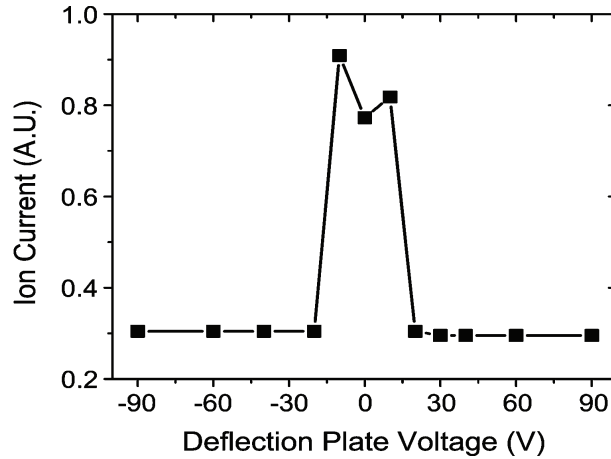


Figure 2.12: Ion current measured as a function deflection voltage.

incorporation in GaInNAsSb happens mainly by excited atoms or molecules, rather than ions. Another interesting thing to note is that the initial experiments with deflection plates used a much higher voltage (+800V and -800V), but this resulted in arcing to the ground in the cell, resulting in no PL improvement [59].

Another technique used to protect the wafer surface from the plasma was arsenic capping. A thick layer of arsenic was deposited after growth of a bottom cladding or a bottom DBR, by keeping an arsenic flux of $\sim 10^{-6}$ torr for 30 minutes to 1 hour while cooling the wafer down to 40°C . The arsenic cap can be easily desorbed by heating the wafer above $\sim 400^{\circ}\text{C}$. This arsenic cap is used to protect the wafer surface during plasma ignition by igniting the plasma before desorbing the capping. Because the plasma operates in a more ion-rich condition (low flow and high rf power), it is worthwhile to protect the wafer during plasma ignition. Significantly higher PL intensity was observed for an arsenic-capped sample than a non-capped sample, and the good laser results were obtained using arsenic capping technique [52, 54, 56, 99].

2.5.5 Laser results

Using the growth improvements described in this chapter, the lowest reported threshold $1.55\mu\text{m}$ GaInNAsSb edge-emitting lasers and the first VCSELs at 1534nm were

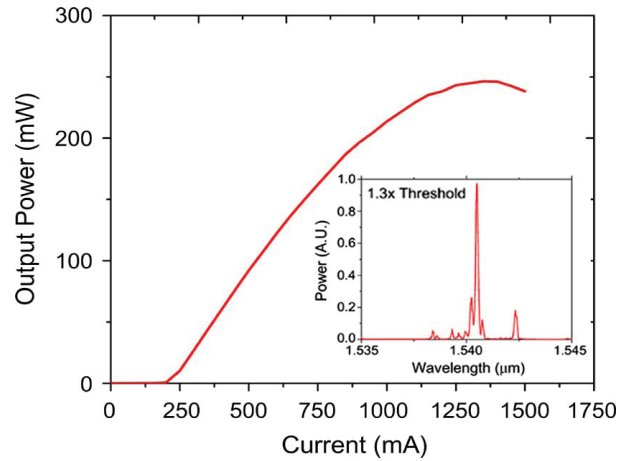


Figure 2.13: CW L-I curve and spectrum for the lowest-threshold $1.55\mu\text{m}$ laser.

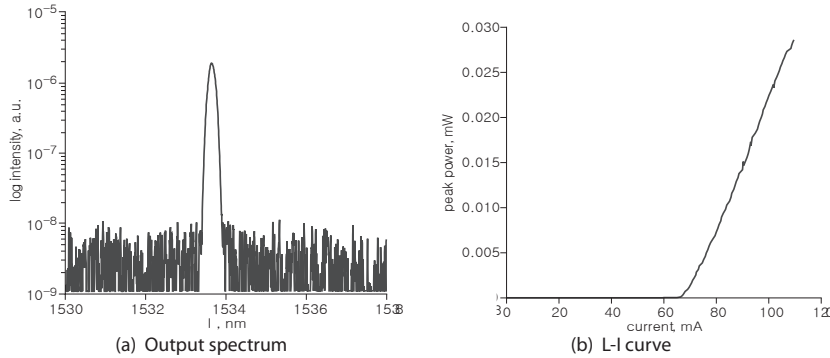


Figure 2.14: Pulsed spectrum and L-I curve for a $14\mu\text{m}$ -aperture VCSEL

realized.

Fig.2.13 shows the CW L-I curve and the spectrum for the $1.55\mu\text{m}$ lasers reported in [52]. The threshold current density of $318\text{A}/\text{cm}^2$ for pulsed operation and $373\text{A}/\text{cm}^2$ for CW operation is the lowest threshold ever reported for GaAs-based $1.55\mu\text{m}$ lasers. CW output power reached 250mW (both facets) and pulsed output power reached 650mW (limited by the laser driver, not by the laser itself). This comes very close to realizing the potential of GaInNAs(Sb) material for $1.3\text{-}1.6\mu\text{m}$ lasers. However, the temperature stability was not as good as was expected, as shown by its relatively low T_0 value (71K up to 35°C and only 21K above 35°C).

Fig.2.14 shows the pulsed VCSEL results emitting at 1534nm. This was the first-ever VCSEL at this wavelength range grown on GaAs, which is a significant achievement, but the VCSEL required significant cooling (below -25°C) and it still operated only in pulsed-mode.

In the following chapters, additional growth and annealing improvements and the results of edge-emitting lasers and the first near-room-temperature CW VCSEL results at 1528nm employing the improvements and careful design efforts.

Chapter 3

Advances in GaInNAsSb growth

3.1 Substrate temperature

Substrate temperature has always been an important growth parameter for molecular beam epitaxy (MBE) [100, 101], along with the fluxes from the effusion cells. GaInNAs(Sb) has been no exception [2, 5, 102]. We observed a distinct optimum growth temperature at 440°C, while the quality degraded by about a factor of two when the temperature is off by 20°C (Fig. 3.1). Therefore, accurate control of the substrate temperature is very important to achieve high quality GaInNAsSb growth reliably and repeatedly.

The MBE chamber has a thermocouple on the substrate heater assembly for measuring the substrate temperature. But this thermocouple provides a very unreliable measurement of the substrate temperature. The intrinsic accuracy of the thermocouple is not the problem, as its accuracy is often within 2 or 3 degrees [103] for temperatures below 600°C. The real problem is that the thermocouple(TC) is not in direct contact with the wafer, far removed from it with a sapphire diffuser plate sitting in between. As a result, the temperature measured by the thermocouple can be 100 or 200 degrees Celcius off from the actual wafer temperature, and worse, the offset is dependent on the size, doping, material, surface quality and mounting method of the wafer.

However, the reproducibility of desorption temperature of the GaAs surface oxide

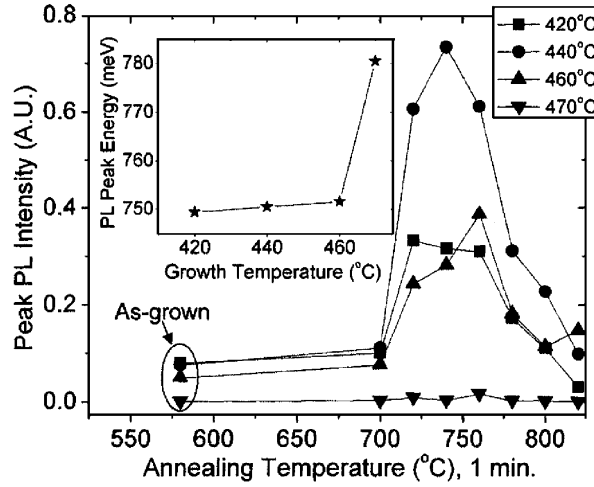


Figure 3.1: Peak PL intensity, as a function of postgrowth annealing temperature. Inset shows the peak emission energy (as-grown) at room temperature. From [2]

[104] has provided a very reliable temperature reference at 582°C. This temperature is also an appropriate temperature for growing high-quality GaAs or AlGaAs layers, so the inaccuracy of TC measurement presented no serious problems for these layers. But the growth temperature for GaInNAsSb is lower than that by 140°C, for which another reliable method for temperature measurement is required.

We initially tried bandgap thermometry, which uses the temperature-dependent bandgap shift of semiconductors. This technique enabled us to do a growth temperature study as in [2], but this was not applicable to doped wafers or complex hetero-structures. Pyrometry measures temperature by measuring the blackbody radiation from the wafer. Pyrometry also has some practical limitations, but it proved sufficiently accurate and reliable for growth of GaInNAsSb QWs. More details are discussed in the following subsections.

3.1.1 Bandgap Thermometry

The bandgap of a semiconductor decreases with temperature, so by measuring the bandgap, one can determine the temperature of the wafer with great accuracy and precision, as described by Hellman [105]. The best measurement would be provided

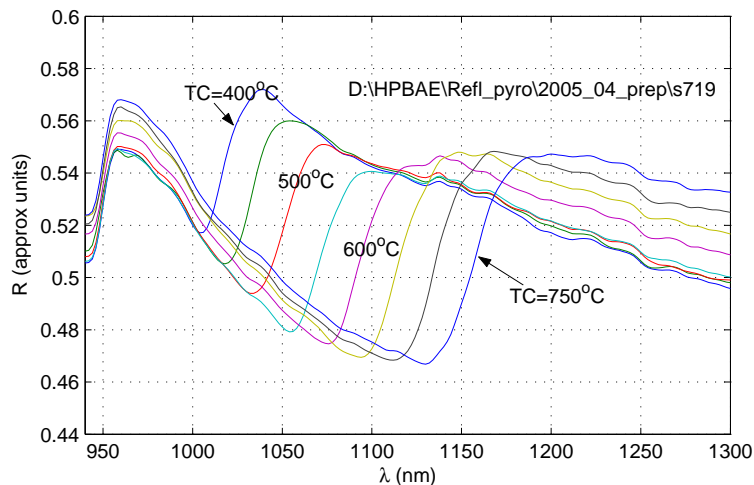


Figure 3.2: Reflectivity spectrum for an undoped wafer at various thermocouple temperatures in 50°C steps

by placing a light source behind the wafer and measuring transmission (absorption) through the wafer. While it would be very convenient to use the substrate heater as the light source, as in [105], the heater radiation was too weak at the QW growth temperatures, and it is not practical to install another light source or fiber on the heater assembly in the MBE chamber.

We used a reflectivity measurement instead, by irradiating the wafer with a 20W halogen lamp installed at one ellipsometry port and detecting the reflection spectrum from the other ellipsometry port. We were able to observe band edge transitions shifting with temperature as shown in Fig. 3.2. Fitting the measured band edge transitions with Varshni parameters, we were able to determine the growth temperature for the QW. This technique was essential in our growth temperature study [2].

Unfortunately, the reflective bandgap thermometry method has a few serious practical difficulties. Many of the problems are due to the reflective setup, whereby the most useful signal comes from those optical rays that enter the wafer through the front surface, go through the wafer, reflect at the backside, travel back to the front surface, and then leave the front surface to reach the detector. This is a significantly smaller signal than the direct specular reflection off of the wafer that does not go

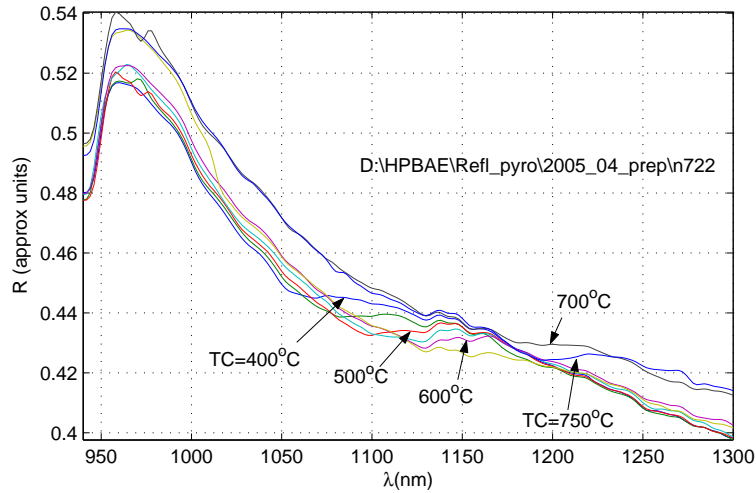


Figure 3.3: Reflectivity spectrum for an n-type wafer at various thermocouple temperatures in 50°C steps

through the substrate material at all. For undoped wafers, the useful signal still represents about 20% of the total signal as shown in Fig. 3.2, which was sufficiently strong for reliable extraction of temperature information. But for doped wafers, it becomes much weaker due to free carrier absorption. The reflectivity spectrum measured for an n-type wafer (Fig. 3.3) still shows the absorption edge red-shifting with higher temperature, but the transition looks quite indistinct and noisy such that we were not confident enough to use it for temperature reference. This problem gets only worse for p-type wafers, due to stronger optical absorption.

Reflective bandgap thermometry was also very susceptible to wafer rotation and optical interference from heterostructures. Since wafer rotation caused large signal fluctuations that swamped the useful signal, we had to leave the wafer stationary for the duration of the entire measurement. In addition, when multi-layer heterostructures are to be grown, such as AlGaAs claddings for edge-emitting lasers or DBR layers for VCSELs, the optical interference from these structures dominates the signal, making it very tricky, if not impossible, to extract temperature information. Due to these problems, we were not able to use this technique either for on-the-fly measurements during growth, or for the QWs in edge-emitting lasers or VCSELs.

Even worse was that the technique required several hours of measurement as a separate and additional process before the growth of each wafer. Since the band edge transition is a gradual one, there is some level of uncertainty about the exact location of the transition. To compensate for this and minimize errors, we measured the reflectivity spectrum for several temperatures, and applied a linear minimum-squared-error fit to the result. This entire process took 3 to 4 hours for each wafer before growth, causing additional delay to the experiments. We also had to provide an arsenic flux during the measurement to avoid arsenic desorption, wasting a significant amount of material unnecessarily.

Thus we concluded that reflective bandgap thermometry is a rather inconvenient, time-consuming, unreliable, and wasteful technique with only limited applicability. We thus tried pyrometry as the next candidate, and it proved easy, versatile, and reliable for our purposes, and the detail is discussed in the next subsection.

3.1.2 Pyrometry

Basic theory

Pyrometry uses the relationship between the blackbody radiation intensity and the temperature for measuring temperature. The blackbody radiation energy at a given temperature T (in Kelvin) is known to depend on T as follows:

$$S = \varepsilon \frac{8\pi hc}{\lambda^5} \frac{1}{\exp(\frac{hc}{\lambda kT}) - 1} \quad (3.1)$$

where the unit of S is energy per unit volume per unit wavelength. ε is the emissivity of the surface, which is equal to $(1-\text{Reflectivity})$ for an opaque substrate [106].

There are many practical issues that complicate the pyrometry. Prominent among them are: emissivity compensation, viewport coating, wafer wobble, heater radiation leakage, and reflections from other heat sources.

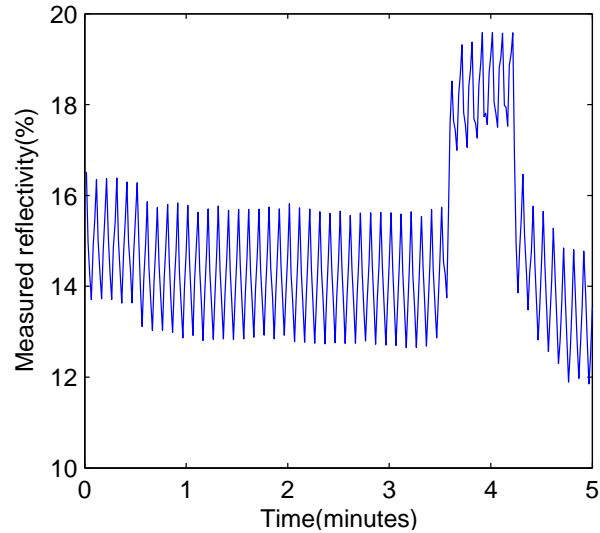


Figure 3.4: Sensitivity of reflectivity measurement to wafer wobble

Emissivity compensation

Upon inspecting Eq. (3.1), it seems absolutely essential to compensate for the emissivity, as the emissivity may change significantly during growth. It would depend slightly on the substrate material and temperature, but the biggest impact would be from the growth of different materials (with significantly different refractive indices) on the substrate, because the reflections at the interfaces would interfere to modulate the overall reflectivity significantly as growth proceeds. In practice, compensating for such emissivity differences proved to be infeasible and unnecessary.

We used an emissivity-compensating pyrometer on our first attempt at pyrometry. Emissivity was estimated by actually measuring the reflectivity from the wafer using an LED and a photodetector pair, and the measured blackbody radiation was processed by Eq. (3.1), using the measured emissivity. Although straightforward in concept, this didn't work very well, because the reflectivity measurement was too sensitive to wafer wobble. As the light emitted from the LED has to reflect off of the wafer, and then reach the photodetector, the alignment requirement is so stringent that even a slight wobble of the wafer causes a large change in the reflectivity measurement.

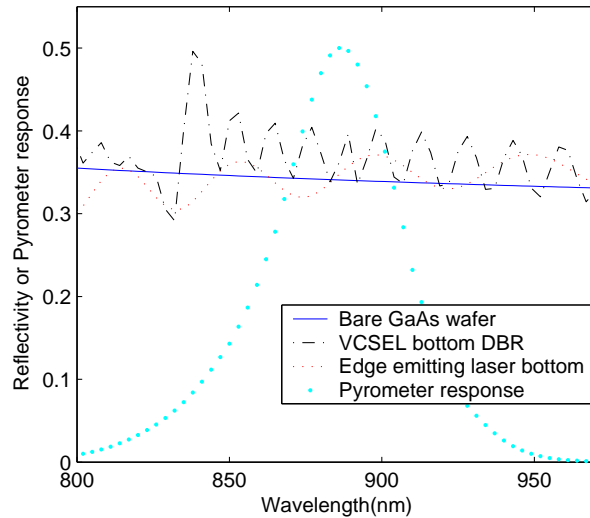


Figure 3.5: Reflectivity of different substrate structures(at 440°C). Also shown is the pyrometer response spectrum, in arbitrary unit.

Fig. 3.4 shows the measured reflectivity (%) while the wafer is rotating. There is a periodic fluctuation (on the order of a few %) in the measured reflectivity, exactly following the period of the wafer rotation. Moreover, we would see a huge jump in the measured reflectivity from time to time. When that happened, the wafer was also seen to jump around in the wafer holder. It should also be noted that the measured reflectivity in Fig. 3.4 is unrealistically low, compared to the roughly 30% reflectivity expected theoretically, due to calibration error. It is virtually impossible to properly calibrate the reflectivity measurement, when the measurement is as unreliable as shown in Fig. 3.4. Thus, it was determined that emissivity compensation adds more error than it reduces to the pyrometry. Note that this difficulty mainly stems from the excessive wafer wobble, which in turn is due to the configuration of our MBE chamber, where the wafer has to stand up perpendicular to the ground. Emissivity compensation can be feasible in different chamber configurations, where the wafers sit parallel to the ground.

Closer look at the optical bandwidth of the pyrometer and the typical growth situation for GaInNAsSb QWs revealed that emissivity compensation, even if it were feasible in our MBE chamber, would not contribute much to the accuracy of temperature

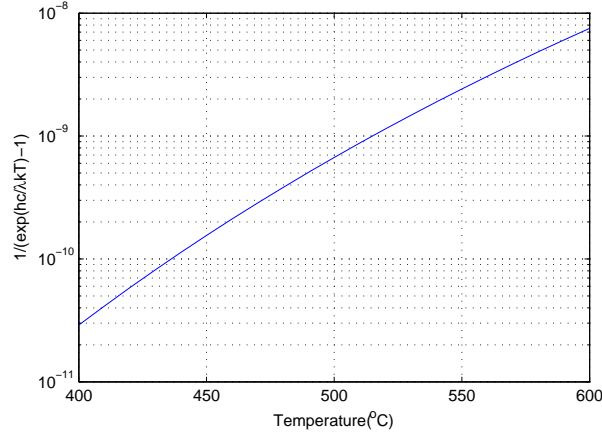


Figure 3.6: $1/(e^{\frac{hc}{\lambda k T}} - 1)$ vs. temperature, $\lambda=886\text{nm}$

control during QW growth. The typical growth situation of our GaInNAsSb/GaNAs QWs was either 1) on a GaAs wafer with no hetero-structure for PL samples, 2) on a 1800nm-thick AlGaAs cladding for edge-emitting lasers, or 3) on a $5 \sim 6\mu\text{m}$ -thick DBR for VCSELs. For PL sample growths, the substrate is simply GaAs, so we wouldn't expect any significant variation in reflectivity (and thus emissivity), except for very minor dependence on temperature and doping ([107,108]). For edge emitter or VCSEL growths, the reflectivity spectrum would obviously show many oscillations. But as shown in Fig. 3.5, the oscillations are finer than the optical bandwidth of the pyrometer detection optics, resulting in significant averaging effect. Thanks to this averaging effect, the overall reflectivity changes only by about 3 percentage points depending on different substrate structures. This emissivity error translates into about a 5 percent error in the estimation of the exponential term in Eq.3.1. This in turn corresponds to temperature error of about 2°C near the QW growth temperature of 440°C , which was good enough for quite reproducible growth of high quality GaInNAsSb QWs. (See Fig. 3.6)

Viewport coating

We were initially concerned that the viewport, through which the pyrometer collects the blackbody radiation from the wafer in vacuum, would get coated with arsenic

over time, leading to a lower signal level and hence lower apparent temperature reading. Although this is theoretically, and also practically possible in MBE or MOVPE chambers, we didn't notice any systematic drift in the temperature measurement over a very long period of 3 years, without any recalibration. The viewport is heated to minimize arsenic deposition, and the exponential nature of the blackbody curve means that even a few percent increase in radiation loss by the viewport corresponds to only 1 or 2°C of temperature measurement error. Even if viewport coating did affect pyrometry, it could be easily solved by recalibrating on a regular basis.

We were also concerned that the radiation from the heated viewport might swamp the radiation from the wafer, but this was in practice no problem, because the viewport temperature is much lower than the growth temperature and the detection optics are focused on the wafer.

Wafer wobble, heater radiation leakage, and reflections from other heat sources

As discussed above, wafer wobble was a serious problem when we tried to measure and compensate for emissivity changes on the fly. On the other hand, without emissivity compensation, we found wafer wobble was less problematic, because measurement of radiation is less sensitive to wafer wobble than measurement of reflectivity. There are two reasons for that; 1) Blackbody radiation is less directional than the focused LED beam used for the reflectivity measurement, and 2) light has to make only a one-way trip from the wafer to the detector for a blackbody radiation measurement, compared to the round-trip required for a reflectivity measurement (i.e., from the LED in the pyrometer, via the wafer, and back to the pyrometer).

However, temperature measurements still showed periodic fluctuations when the wafer was rotating, as shown in Fig. 3.7, for a 3-inch GaAs wafer. The amplitude of this fluctuation was different for different wafers, and the most dominant effect was from the size of the wafer. The fluctuation was larger for smaller wafers, as shown in Fig. 3.7, Fig. 3.8 and Fig. 3.9. The source of these fluctuations was determined to be the leakage of substrate heater radiation around the edges of the wafer. Fig. 3.10 shows a schematic of different wafer sizes on the wafer holder. 2-inch or quarter 3-inch

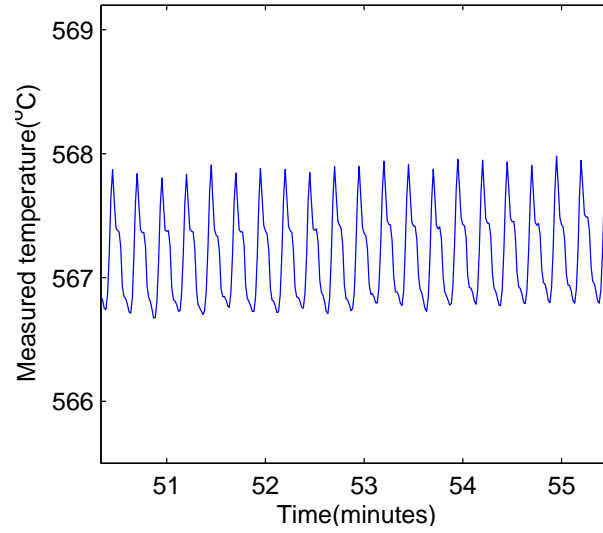


Figure 3.7: Pyrometer measurement fluctuations for a 3-inch wafer

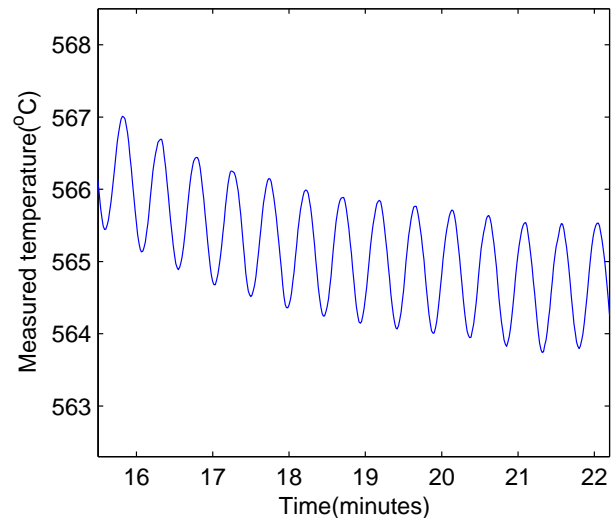


Figure 3.8: Pyrometer measurement fluctuations for a 2-inch wafer

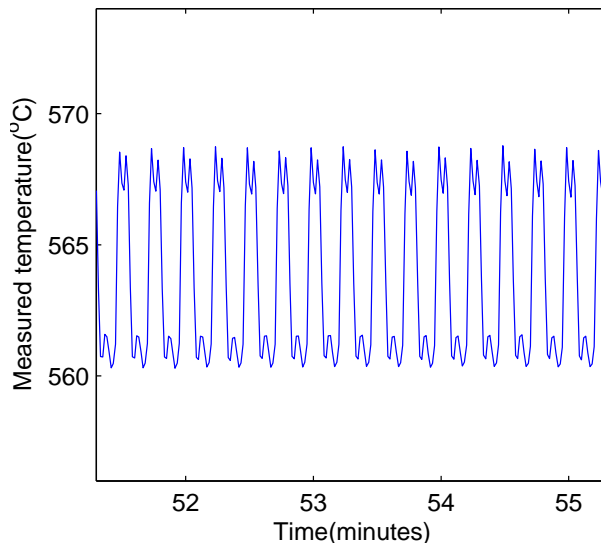


Figure 3.9: Pyrometer measurement fluctuations for a quarter of 3-inch wafer

wafers have gaps around the edges, through which one can clearly see the orange glow of the substrate heater. As the detection optics of the pyrometer has a finite spot size on the wafer, it is not surprising that this heater radiation is also captured by the pyrometer, causing a periodic perturbation in measurement as the wafer rotates. As further evidence of leakage, the fluctuations are much larger during wafer heat-up as the heater is hotter, compared to during cool down, as shown in Fig. 3.11. A full 3-inch wafer also leaves a small gap around its major flat, so it also exhibits similar fluctuations, although smaller in amplitude. The magnitude of these fluctuation was at most $\pm 1^\circ\text{C}$ for 3-inch wafers, or $\pm 2^\circ\text{C}$ for 2-inch wafers, which was good enough for reproducible growth of GaInNAsSb QWs. Fluctuations for quarter 3-inch wafers were found to be too large for reliable growth, sometimes being larger than $\pm 5^\circ\text{C}$.

Measurement wavelength was also found to be a critical choice for pyrometry. We initially used 980nm as the detection wavelength, but this turned out to be a poor choice, because GaAs is transparent at this wavelength up to around 400°C , allowing the substrate heater radiation to pass through the wafer, thus swamping the blackbody radiation from the wafer itself. We finally chose 886nm, for which GaAs turns opaque at approximately 100°C , which is sufficiently lower than our QW growth

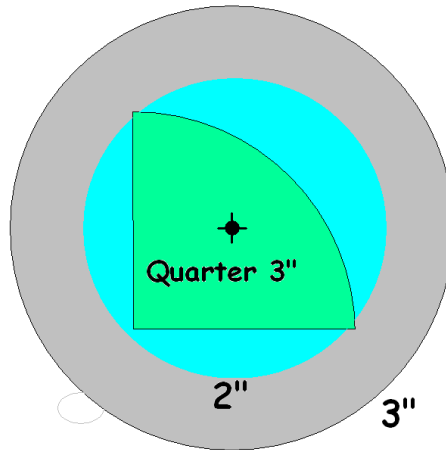


Figure 3.10: Schematic of typical wafer sizes when loaded on the substrate heater

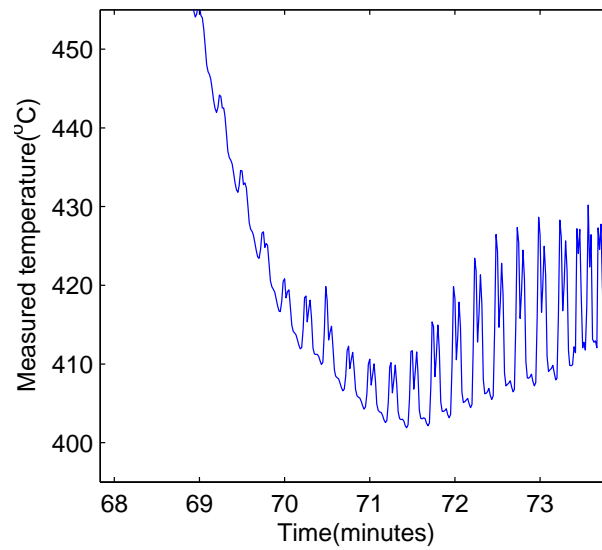


Figure 3.11: Pyrometer measurement during cool-down and then heat-up, for a quarter of 3-inch wafer

temperature of 440°C.

Reflected radiation from other heat sources in the chamber can also affect pyrometry. Effusion cells, especially the gallium cell, can be as hot as 1000°C during growth. The cracker section of the arsenic cell is at 850°C even in the idle state. This is much hotter than the wafer during growth, and their blackbody radiation is larger by several orders of magnitude. Some of this radiation is captured by the pyrometer after reflections in the chamber, limiting the minimum temperature that the pyrometer can measure. Although the intrinsic capability of the pyrometer (when the detector noise is compared to blackbody radiation) has no problem measuring as low as 300°C, reflected radiations from hot cells prevented the pyrometer from reading lower temperatures than 360°C, even when the wafer was at room temperature. Fortunately, this was sufficiently lower than our typical growth temperature that this technique proved useful.

Implications for temperature control

Despite these difficulties as discussed above, pyrometry proved to be a useful technique with a reasonable accuracy of \pm a few degrees Celcius. It was also much faster, more convenient, and more versatile compared to the band-edge absorption method, which required several hours of measurement for each wafer and worked only for bare SI wafers. Pyrometry is also much more accurate than the thermocouple, which could be off by 100 or even 200°C.

Pyrometry also allowed us to discover a few more interesting characteristics of wafer heating in the MBE chamber.

First, different wafers may heat up at completely different rates and efficiency. Especially dominant is the effect of wafer doping. Undoped wafers require much higher thermocouple temperature and higher heater power than doped wafers. Undoped wafers are also much slower to heat than doped wafers. When we increase the temperature setpoint, undoped wafers tend to take several minutes to reach the setpoint, following a smooth curve. On the other hand, doped wafers heat up very quickly overshooting by a large amount (as much as 50°C), and then settle down to the setpoint temperature. Typical trajectories of wafer temperatures during heat-up

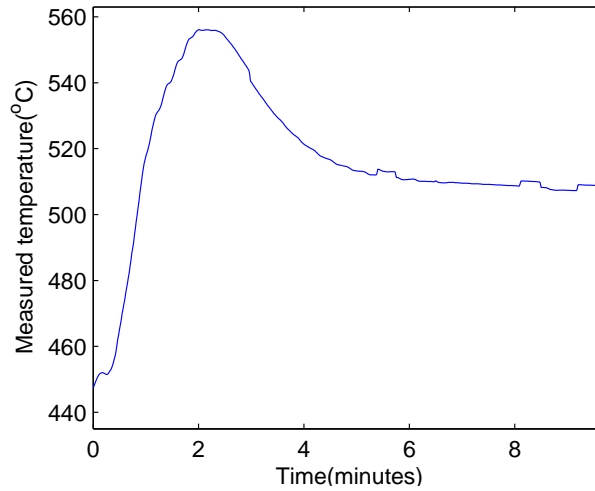


Figure 3.12: Pyrometer measurement during heat-up, for a 3-inch n-type wafer. Small bumps are due to wafer tilting for easier RHEED observation

are shown in Fig. 3.12 and Fig. 3.13. This difference shows that the wafer is heated mainly by absorbing the radiation from the heater, rather than by heat conduction. It also shows that we have to be very careful and patient when determining the deox temperature, because the wafer temperature might still be in a transitory state if we don't allow the wafer enough time to stabilize at a given temperature.

The second important finding is that the GaAs oxide desorption temperature is indeed very constant and reliable. We observed a very similar temperature reading (within a few degrees) on the pyrometer as the oxide desorbs from the wafer, regardless of wafer type, size, and vendor. We did doubt in the past whether the deox temperature was really constant because we saw no consistency in the TC reading at the deox temperature [56], but pyrometry enabled us to finally use this reference with confidence.

It was also found that the TC reading offset between the deox and the QW growth temperatures were quite repeatable, although each of them varied a lot in TC reading, wafer to wafer. Fig. 3.14 shows the thermocouple readings at the deox(580°C) and the QW growth(440°C) temperatures, for several 3" n-type wafers. The deox temperature was determined by inspecting RHEED in the sys4, and the QW growth temperature

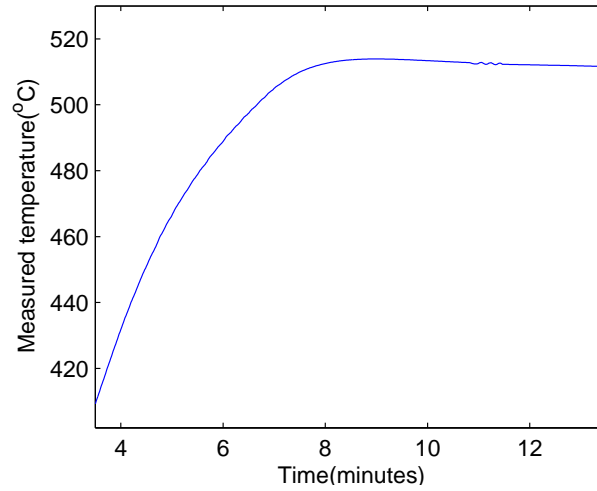


Figure 3.13: Pyrometer measurement during heat-up, for a 3-inch undoped wafer

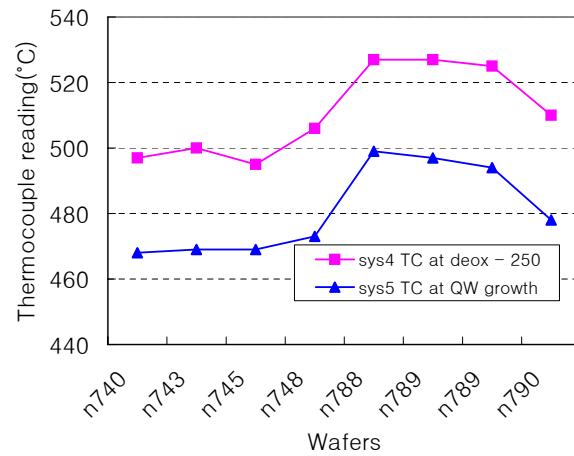


Figure 3.14: TC readings at deox in sys4 and at QW growth in sys5

was determined by pyrometry in the sys5. The difference in thermocouple reading between the two temperatures was consistently very close to 280°C, even though the two temperatures were measured in two different chambers. It was also found that the thermocouple readings from the two chambers at deox temperature were 50°C apart from each other. From then on, we decided to grow QWs at 230°C lower than the sys5 deox temperature by thermocouple reading, or equivalently, 280°C lower than the sys4 deox temperature by thermocouple reading. For full 3" n-type wafers, we checked the pyrometer reading during growth as well, to make sure the temperature was correct, and we didn't experience any unexpected deviation. For quarter 3" n-type wafers, we used the same method, only putting less weight on the pyrometer reading due to its higher error for smaller wafers. Using this method, we grew quite a few PL samples on quarter 3" n-type wafers and they showed very repeatable PL intensity and wavelength. Though we have not established whether a similar method can be used for undoped or p-type wafers, establishing this relationship for n-type wafers was sufficient for the purposes of this thesis, as the PL samples and the lasers only required n-type wafers.

3.2 Improvement in annealing conditions

Dilute nitride materials typically have quite a large number of defects as-grown, due to low N solubility in GaAs or InGaAs [21,22], and in the case of MBE growth, from the ion-related damage from the rf plasma cell [29]. Post-growth annealing has been a standard process for dilute nitrides to remove as-grown defects and improve material quality [109] and there have been many reports about the annealing properties [65, 72, 77, 85, 110–114].

The annealing experiments have been done by two different methods: One is to anneal the as-grown samples in the growth chamber (in-situ) or a furnace for a relatively long time (tens of minutes) with arsenic fluxes supplied to suppress arsenic desorption from the sample surface [113]. The second is to anneal the samples in an RTA chamber for a short time (up to a few minutes), with a GaAs cap wafer to minimize arsenic desorption [72, 111, 112, 114, 115]. It may seem natural to wonder

which annealing method produces a better quality after annealing, but for some unknown reasons, most research groups tended to stick to one method rather than comparing the two and choosing the better one. Our group was no exception in this respect, sticking to 1-minute annealing at a few different temperatures in an RTA. We were able to achieve very low threshold for $1.55\mu\text{m}$ GaInNAsSb lasers [52] by using 1-minute annealing, but this doesn't necessarily mean that it is the best that could be achieved.

For silicon CMOS processing, it is well known that short-duration high-temperature annealing is better than long-duration low-temperature annealing because the defect annealing effects have stronger temperature dependence than the undesirable transient enhanced diffusion (TED). We were interested in finding out whether GaInNAsSb QWs follow an analogous or an opposite trend. In the case of dilute nitrides, there are two distinct processes affecting the material quality during annealing: one is removal of growth-induced defects and the other is creation of annealing-induced defects [77]. Comparison of temperature dependencies of the two processes would reveal whether short-duration high-temperature annealing or long-duration low-temperature annealing results in higher material quality.

To determine the temperature dependencies of annealing processes, we annealed GaInNAsSb PL samples using various temperatures and durations. A PL sample has a 7.5nm-thick $\text{Ga}_{0.62}\text{In}_{0.38}\text{N}_{0.03}\text{As}_{0.943}\text{Sb}_{0.027}$ QW with 21nm $\text{GaN}_{0.04}\text{As}_{0.96}$ barriers on both sides, after growing 300nm undoped GaAs buffer layer and is followed by a 50nm GaAs layer. The GaAs layers are grown at 580°C and the QW is grown at 440°C with V/III BEP (beam equivalent pressure) ratio of 20. This is nominally the same composition and growth condition as those QWs used for our lowest threshold $1.55\mu\text{m}$ GaInNAsSb lasers as reported in [52]. It is important to use high quality QWs as in this study to make sure that the intrinsic property of GaInNAsSb QWs is not obscured by extrinsic behaviors due to an unnecessarily high level of defects, as the level of defects can affect the annealing properties significantly [87, 88].

Figure 3.15 shows the peak photoluminescence (PL) intensity and wavelength after annealing GaInNAsSb PL samples for 1-minute in the RTA. As previously reported by many researchers, the PL intensity initially increases with temperature as

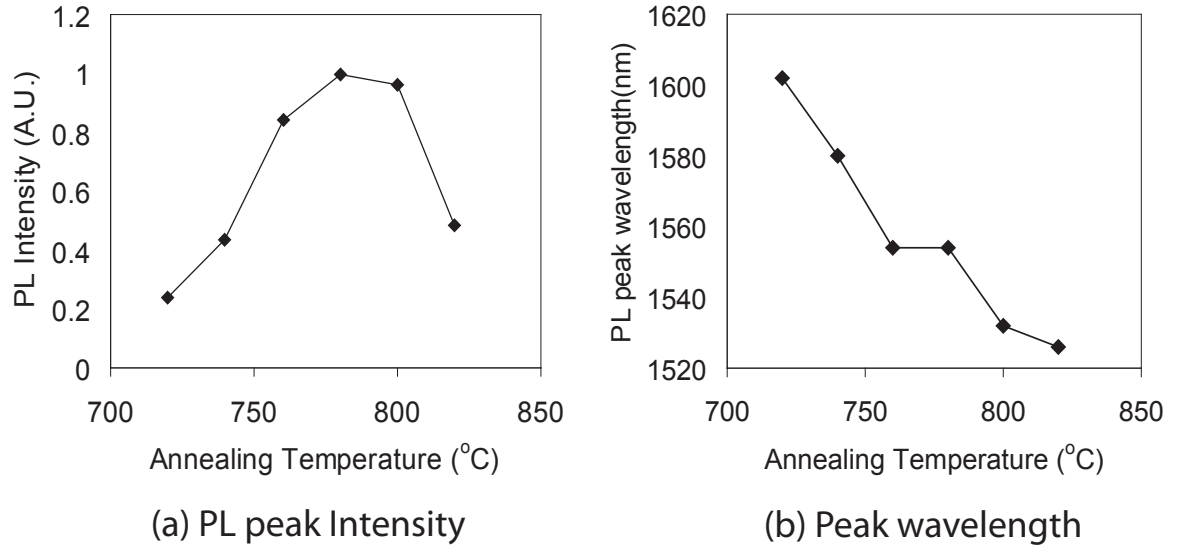


Figure 3.15: Result of 1-minute annealing at different temperatures for $\text{Ga}_{0.62}\text{In}_{0.38}\text{N}_{0.03}\text{As}_{0.943}\text{Sb}_{0.027}$ QW

growth-induced defects are annealed, but starts to degrade when the temperature gets too high. The optimum occurs around 780 $^{\circ}\text{C}$. The wavelength becomes shorter as the QW is annealed at higher temperatures. The mechanism of the blueshift was initially hypothesized to be indium [79, 80, 116] or nitrogen [3, 23] outdiffusion from the quantum wells, but later research indicated that the change in nearest-neighbor configuration of nitrogen atoms explains most, if not all, of this effect [85]. In Fig. 3.15, the PL intensity is normalized with respect to the optimum at 780 $^{\circ}\text{C}$, and this optimum intensity is used as the reference for the annealing and growth studies in this and following sections.

The first experiment was to anneal the same PL samples at 700 $^{\circ}\text{C}$, for 10 to 150 minutes, as shown in Fig. 3.16. The 700 $^{\circ}\text{C}$ result resembles that in Fig. 3.15, in that the PL intensity initially increases and then eventually decreases when annealed too long or too hot. But unlike Fig. 3.15, Fig. 3.16 shows a very wide window of flat PL intensity (as long as 2 hours), and the peak PL intensity is more than two times higher than the 1-minute annealed samples. Note that a similar wide plateau was also observed in [65], where the PL intensity improvement saturates after about 5

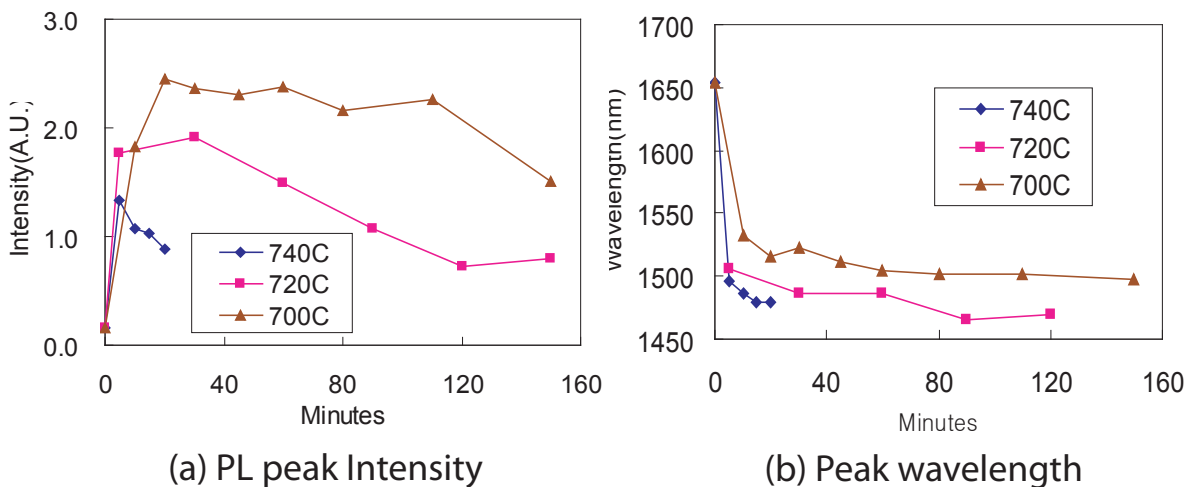


Figure 3.16: PL intensity and wavelength vs. annealing duration for Ga_{0.62}In_{0.38}N_{0.03}As_{0.943}Sb_{0.027} QW.

minutes and stays flat up to 30 minutes. [65]. But eventual degradation after 2 hours of apparent stability of material quality was not reported in [65] or any other reports, to the best of our knowledge.

Such a long stability plateau and the following degradation is a very interesting behavior in itself, and the higher PL intensity compared to 1-minute annealing is also very intriguing. Additionally, at 700°C, the over-anneal degradation does not begin until the sample is annealed more than 2 hours. On the other hand, a 1-minute anneal at 800°C was enough to generate annealing-induced defects, as shown in Fig. 3.15. This implies that the annealing-induced degradation has a very steep temperature dependence, or equivalently, a large activation energy. To examine the temperature dependence of the annealing-induced degradation, we next annealed samples at 720°C and 740°C until substantial degradation was observed, and the result is also shown in Fig. 3.16. While it took as long as 150 minutes until the onset of degradation at 700°C, it took only 60 minutes at 720°C, and only about 10 minutes at 740°C. This is roughly $\times 3$ – $\times 5$ difference for every 20°C, which in turn translates into activation energy of 6–7eV assuming an Arrhenius relationship.

On the other hand, removal of growth-induced defects was found to have a much

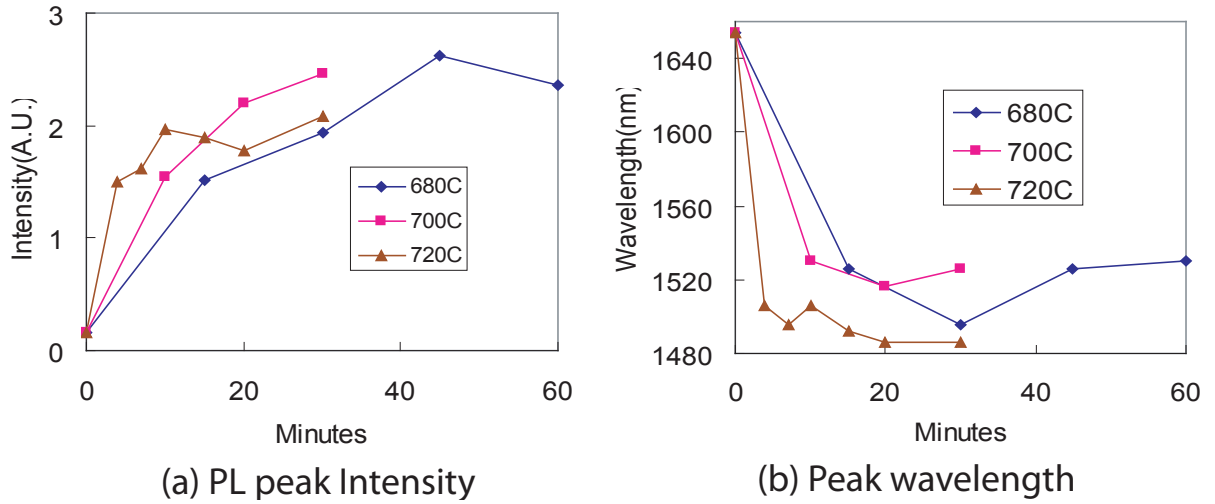


Figure 3.17: PL intensity and wavelength vs. annealing duration for Ga_{0.62}In_{0.38}N_{0.03}As_{0.943}Sb_{0.027} QW.

shallower temperature dependence than that of annealing-induced defect generation. Figure 3.17 shows the result of annealing experiments at 680–720°C. The PL intensity saturates after about 40 minutes of 680°C annealing, whereas it takes 30 and 10 minutes at 700°C and 720°C respectively for the PL intensity to saturate. This temperature dependence is about $\times 2$ faster per 20°C increase, which translates into activation energy of about 3eV.

Due to this combination of a shallow temperature dependence for removal of growth-induced defects, and the steep temperature dependence of annealing-induced degradation, longer and cooler anneals produce not only higher but also more reproducible PL intensity than shorter and hotter anneals, because the lower temperature inhibits the degradation process more significantly than it slows the improvement process. The optimum intensity that can be achieved with long anneals at 700°C was indeed about $\times 2$ higher than our previous best for 1-minute anneals. (Compare Figs. 3.15 and 3.16. Their PL intensities are plotted in the same scale, so that direct comparison is possible.) This higher PL intensity by low-temperature long-duration annealing implies better material quality, which in turn can produce better laser results. In addition, low-temperature, long-duration annealing allows a very wide

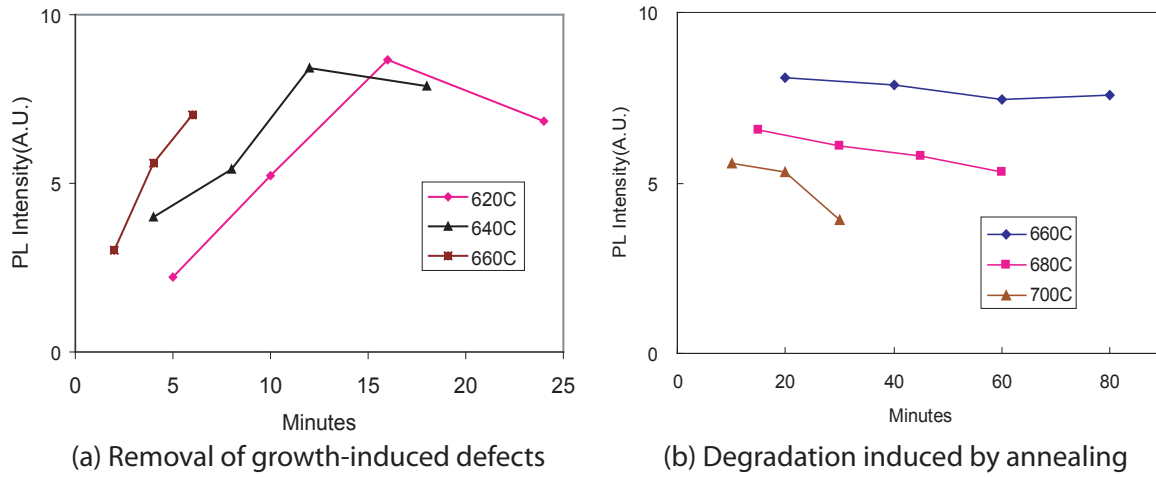


Figure 3.18: PL intensity vs. annealing duration for $\text{Ga}_{0.7}\text{In}_{0.3}\text{N}_{0.012}\text{As}_{0.968}\text{Sb}_{0.02}$ QW.

optimum processing window, which significantly improves process control.

Similar experiments were done for a significantly different QW composition, namely 7nm-thick $\text{Ga}_{0.7}\text{In}_{0.3}\text{N}_{0.012}\text{As}_{0.968}\text{Sb}_{0.02}$ QW, for $1.26\mu\text{m}$ emission after anneal ($1.31\mu\text{m}$ before anneal). The result is shown in Fig. 3.18. We can see a very similar trend as in Figs. 3.16 and 3.17. The PL intensity degradation by annealing-induced defects have a steep temperature dependence, exhibiting a widely different behavior for only 40°C difference in the annealing temperature. Compared to that, the removal of growth-induced defects show a much shallower temperature dependence.

Another kind of PL samples with a completely different structure was also annealed and measured, namely 150-nm thick $\text{Ga}_{0.92}\text{In}_{0.08}\text{N}_{0.02}\text{As}_{0.98}$. This is a lattice-matched thick layer with light emission at $1.15\mu\text{m}$, rather than a strained QW. It has no Sb and only 5nm GaAs cap layer, unlike the other two kinds of PL samples discussed above, which had Sb incorporation and 50nm cap layers. Despite these differences, Fig.3.19 shows a similarly shallow temperature dependence for the removal process of growth-induced defects, namely roughly $\times 4$ every 40°C , which is equivalent to $\times 2$ every 20°C . On the other hand, we were not able to extract meaningful temperature dependence for the creation of annealing-induced defects due to rather noisy result as shown in Fig.3.19(b) and insufficient amount of samples left for

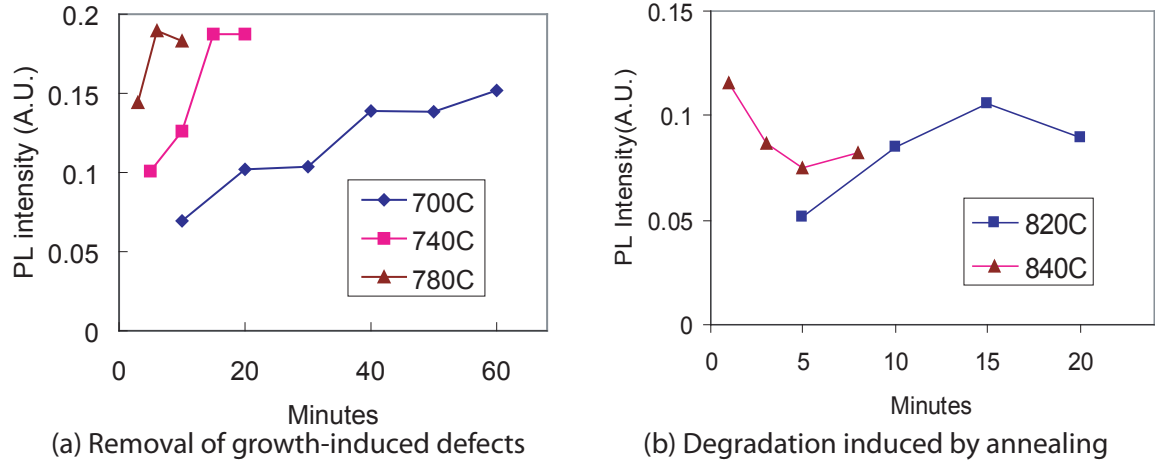


Figure 3.19: PL intensity vs. annealing duration for lattice-matched 150nm-thick $\text{Ga}_{0.92}\text{In}_{0.08}\text{N}_{0.02}\text{As}_{0.98}$ layer.

measurement. However, this result still agrees with those of the other two samples in that the lower-temperature annealing results in roughly $\times 2$ higher PL intensity than higher-temperature annealing for a short duration. (PL intensities of Fig.3.19(a) and (b) can be directly compared with each other.)

These measurements indicate that different alloys of GaInNAs(Sb) exhibit similar dependence on annealing temperatures, even for vastly different compositions and thicknesses. This implies that the same defect removal and defect creation mechanisms are in action during annealing for any GaInNAs(Sb) compositions, which is not surprising since this annealing behavior is unique to the dilute nitride materials and is definitely closely associated with their unique growth conditions due to the low solubility of nitrogen.

On the other hand, the improvement and degradation processes by annealing are observed at widely different temperatures depending on the composition, as reported by many researchers [72,85,112,114,115]. This indicates that the PL degradation from over-annealing does not arise from arsenic vacancies from the surface or elsewhere in the substrate, because the annealing temperature and duration at which the arsenic vacancies reach the GaInNAs(Sb) layer would not depend much on its composition.

Outdiffusion from the QW [77] was also suggested as a cause of PL degradation from over-annealing, but apparently this is not the case either, as the interdiffusion process has been reported to have an activation energy of about 3eV [89, 110, 117], which is significantly smaller than the activation energy of annealing-induced defects as discussed above. A 6–7eV activation energy is observed for annealing-induced defects for our GaInNAs(Sb) QW samples, which is rather large for point defects, so we suspect it is more likely to be associated with extended defects, i.e. dislocations. Actual observation of dislocations was reported in [77] using TEM (transmission electron microscopy), but more research is needed to fully understand the mechanism of the annealing-induced defects.

The wavelength blueshift is another important process that happens during annealing. It is now known that a large portion of the blueshift is due to the nearest-neighbor reconfiguration of nitrogen atoms, and the activation energy of the reconfiguration process is quite low ($\sim 0.6\text{eV}$) [85, 117]. This reconfiguration happens rather quickly during the initial phase of annealing, and then additional blueshift due to interdiffusion and its activation energy of about 3eV is reported [110, 117]. Our wavelength measurements in Figs. 3.17 and 3.16 qualitatively agree with these reports with very rapid initial blueshift commensurate with the low activation energy of $\sim 0.6\text{eV}$, and very small, if any, additional blueshift agreeing with the higher activation energy of $\sim 3\text{eV}$. However, the additional blueshift due to interdiffusion is so small compared to the initial large blueshift due to nearest-neighbor reconfiguration that it can be practically ignored for device applications.

The most important implication of this annealing experiment for this thesis work is that about $\times 2$ higher PL quality can be achieved by annealing at lower temperatures for longer durations, instead of the *traditional* 1-minute annealing. In addition, the PL intensity stays high for a very wide window of annealing durations, making the process far easier to control.

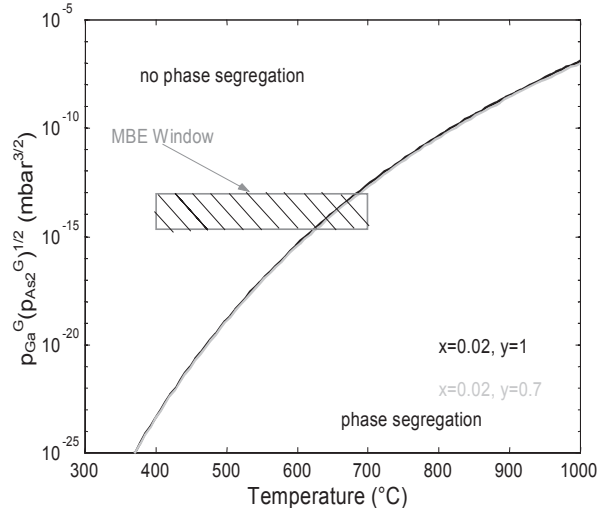


Figure 3.20: Ga and As equivalent pressures for which segregation-free growth happens for $\text{Ga}_y\text{In}_{1-y}\text{N}_x\text{As}_{1-x}$ [3]

3.3 Improvement by Lower group-V flux

Early theoretical and experimental work proposed that low growth temperatures and high arsenic fluxes were required for single phase molecular beam epitaxy (MBE) of dilute nitride materials [3, 118], as shown in Fig.3.20. Following these growth guidelines, we were able to realize low threshold $1.5\mu\text{m}$ GaInNAsSb lasers by growing at relatively low temperatures (440°C) and high group-V fluxes ($\times 20$ V/III ratio in BEP (beam equivalent pressure)) [52]. On the other hand, significant improvement in material quality for Sb-free GaInNAs was reported when grown at a much lower arsenic flux (only $\times 1.2$ of group-III flux) and also much lower temperature (350°C) [5]. This result does not contradict with the growth regime illustrated in Fig.3.20 as lower temperature does allow lower arsenic pressure, but it draws our attention to the fact that the analysis underlying Fig.3.20 [3] only deals with the avoidance of phase segregation, and thus does not actually specify exactly which growth condition to choose in the wide parameter range that allows segregation-free growth. Low temperature and high arsenic flux prevents phase segregation, but on the other hand it may reduce the surface mobility too much by limiting arsenic re-evaporation, leading

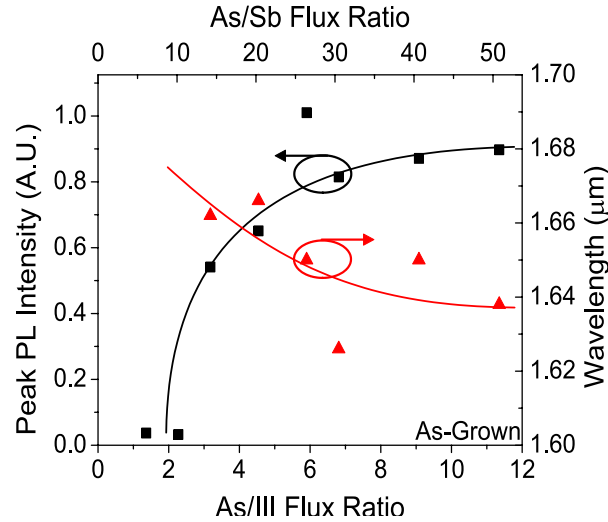


Figure 3.21: PL results for GaInNAsSb QWs, as a function of the As/III flux ratio

to undesirable excess As point defects. As this possibility was not explicitly explored, it seemed likely that the high arsenic flux growth previously considered optimum was not actually the best achievable.

We first examined the possibility by trying different arsenic fluxes at 440°C , the result of which is shown in Fig.3.21 and reported in [76]. The graph is shown in terms of actual As/III flux ratio, which is about half of the BEP(Beam Equivalent Pressure), and the sample with the highest As/III ratio in the graph corresponds to the As/III BEP ratio of 20. From this result, 440°C and x20 As/III BEP ratio actually is the optimum, with the PL intensity decreasing slowly as the ratio is lowered, before dropping precipitously as the flux ratio drops below 3. On the other hand, the wavelength becomes longer as we lower the arsenic flux, which is probably due to increased antimony incorporation as the Sb/As ratio increases with lower As flux. In addition to wavelength change, the Sb/As ratio is also known to affect the growth quality as shown in Fig.3.22 [4], so it is very possible that changing the As flux alone is not the best way to explore the growth parameters.

Therefore, we instead set out to change the As and Sb fluxes together, while keeping their ratio constant. We grew $1.55\mu\text{m}$ PL samples at various $(\text{As}+\text{Sb})/\text{III}$

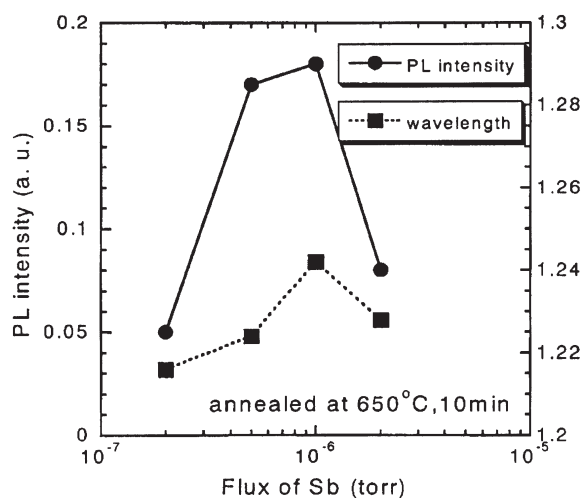


Figure 3.22: PL results versus Sb flux from [4]

flux ratios at two different growth temperatures. The first set of samples were grown with 39% indium with the (As+Sb)/III flux ratios ranging from $\times 11$ to $\times 20$ in BEP ratio (roughly $\times 5.5$ to $\times 10$ in real flux ratio) at 410°C . The ratio between arsenic and antimony fluxes was fixed at 54 in BEP, and the nitrogen plasma was also kept constant, with the same gas flow and power. Another set of similar PL samples was grown at 410°C , under (As+Sb)/III ratios ranging from $\times 3$ to $\times 11$. And the third set of PL samples was grown at 440°C with (As+Sb)/III ratios between $\times 2$ and $\times 15$. This first set was grown about 18 months before the other two samples, and its results were reported earlier in [76]. During the 18 months, the MBE chamber was not operational going through significant repairs and maintenance, and the nitrogen plasma cell was operating under a significantly different condition after the repairs, as described in the previous chapter. Despite the significant lapse of time and different chamber condition, the results of all three sets of growths align with one another reasonably well, which is a good sign for the repeatability of GaInNAsSb growth.

Figure 3.23 shows the peak PL intensity after 1-minute annealing for the first set of samples (Growth T= 440°C). Figure 3.24 shows the peak PL intensity for all the three sets of samples. (note: The result for $\times 2$ flux ratio grown at 440°C is not

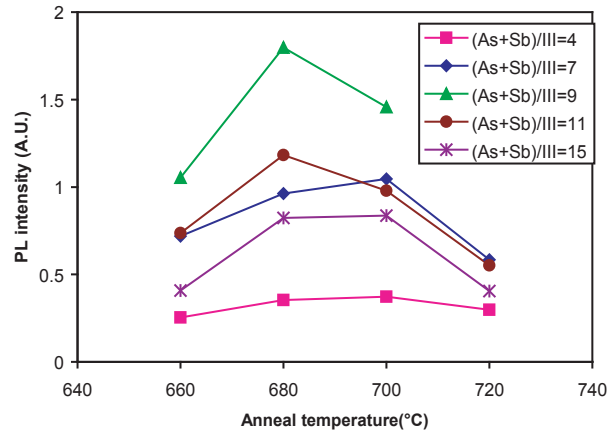


Figure 3.23: PL intensity for different $(As+Sb)/III$ flux ratios annealed for 1 minute

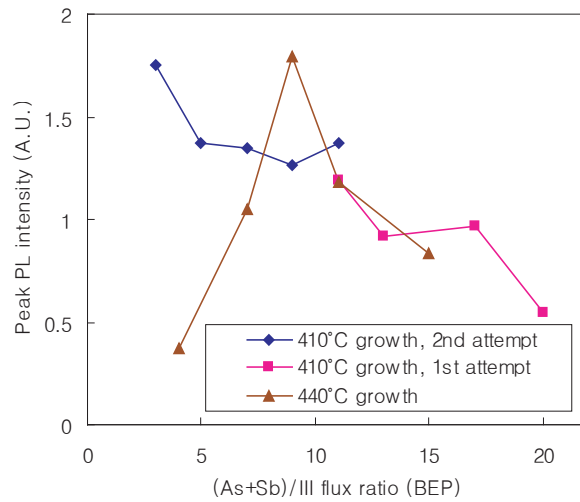


Figure 3.24: PL intensity at the optimum annealing temperature vs. $(As+Sb)/III$ flux ratio. Annealed for 1 minute

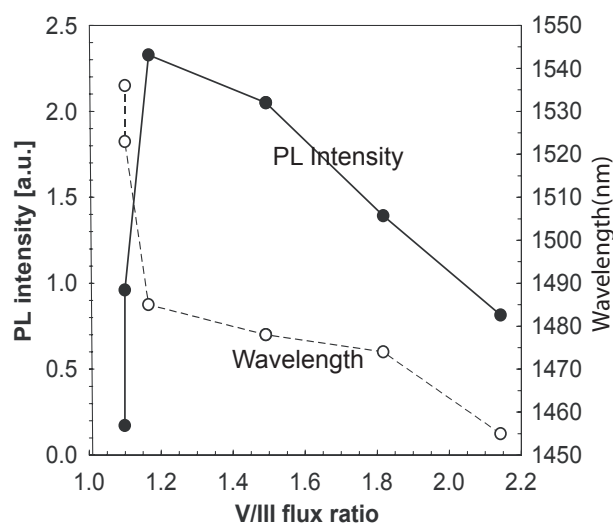


Figure 3.25: PL peak intensity (solid circles) and wavelength (open circles) versus As/III ratio [5]

shown because the sample was optically inactive.)

The most important point from this result is that much higher PL intensity ($\sim \times 2$) is achieved by lowering As and Sb fluxes together. It is to be noted that the PL intensity graphs are normalized with respect to the peak intensity we achieved under the growth condition of $\times 20$ flux ratio and 440°C and 1-minute annealing, which was previously considered optimal.

And there is an optimum flux ratio, which varies depending on the growth temperature. Fig.3.24 shows that both too high and too low fluxes result in sub-optimal PL intensity, with an optimum flux ratio of about 9 when grown at 440°C . On the other hand, the optimum flux ratio is either 2 or even lower at 410°C . Both growth temperatures give similar optimum PL intensity, but we chose to use 440°C as the growth temperature, because the optimum V flux is too low (close to 1 in real V/III flux ratio) for the 410°C growth, and the growth quality would be too sensitive to the group-V flux control as shown in Fig.3.25 [5]. There is also less concern about the controllability of the arsenic flux when grown at 440°C , because the adjacent GaNAs layers are grown at a (As+Sb)/III BEP ratio of 15, which is much higher than the low flux required for 410°C growth of GaInNAsSb, but closer to $\times 9$ required for 440°C

growth. Temperature control is also easier at 440°C, as the pyrometer noise floor is too high for good control at 410°C, and the required temperature change from the 580° for adjacent GaAs layers is smaller for 440°C.

The trend of lower optimal flux for lower growth temperature can be easily understood from the conventional tradeoffs in MBE growth conditions, whereby either high growth temperature or low group-V flux leads to excessive surface desorption or phase segregation, while growth at too low temperature or too high group-V flux impedes atoms from reaching the correct lattice sites. The effect of antimony flux is especially important, as it is a reactive surfactant, which improves the quality of epitaxy by inhibiting the surface diffusion length [90] when the epitaxial layer is either strained or has a large miscibility gap, both of which are true for GaInNAsSb grown on GaAs [21,22]. As the antimony flux has a strong influence on the surface diffusion properties, reduction of Sb flux together with As flux was critical to improving the material quality in this report, while no improvement was observed if only the As flux was changed. On the other hand, the other group-V element, nitrogen, showed no measurable variation in composition as determined by SIMS over the samples in this study, despite the huge variation in the As and Sb fluxes. This insensitivity of N incorporation to other group-V fluxes agrees with our previous finding that nitrogen behaves more like a group-III element as far as composition control is concerned, and its composition is mainly dependent on the growth rate, which is determined by the group-III fluxes [23].

Figure 3.26 shows a dependence of wavelength on the (As+Sb)/III ratio, where the wavelength tends to decrease as the flux ratio approaches the optimum ratio for high PL intensity. Although it might be possible that antimony incorporation increases slightly under high Sb and As fluxes and nitrogen incorporates more under low Sb and As fluxes, the actual SIMS results shown in 3.28 do not support this hypothesis. No significant difference was found in the HRXRD measurements either, as shown in Figure 3.27 for 440°C growths. The HRXRD scans show very similar high structural qualities and the strains do not show any discernable difference. We were not able to determine the mechanism of the wavelength dependence, but shorter wavelength for the optimum PL intensity was repeatedly observed. Therefore, we tried to increase

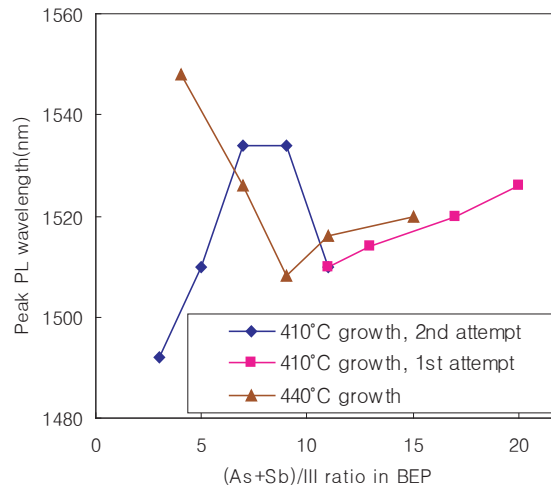


Figure 3.26: PL wavelength for different (As+Sb)/III flux ratios. Annealed for 1 minute

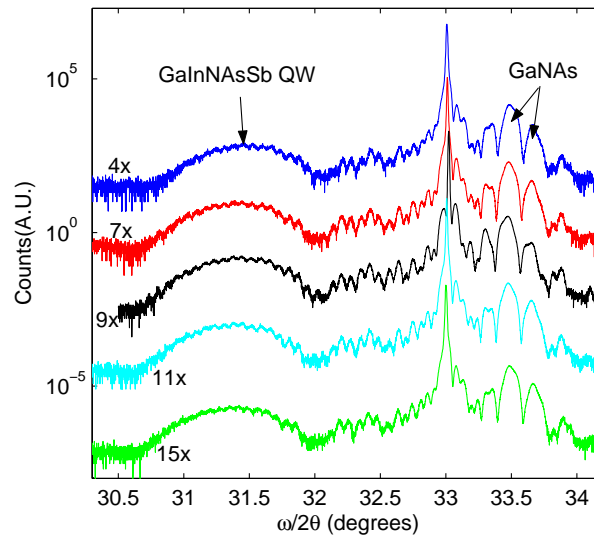


Figure 3.27: XRD result for different (As+Sb)/III flux ratios, grown at 440°C

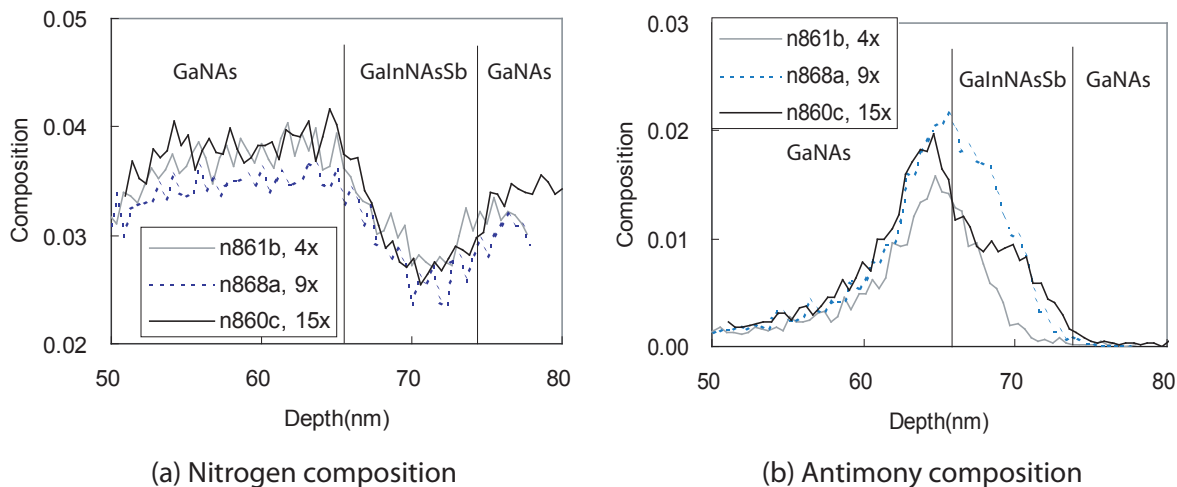


Figure 3.28: SIMS result for $\times 4$, $\times 9$, and $\times 15$ (As+Sb)/III ratio growths, at 440°C

the emission wavelength closer to 1550nm, by increasing the In composition.

We grew two different samples with 39%(n852) and 41%(n851) indium in the GaInNASb layer under $\times 11$ (As+Sb)/III ratio (in BEP), and one sample(n864) with 41% indium under $\times 9$ (As+Sb)/III ratio. Growth temperature was 440°C for all three samples. The samples were first annealed at different temperatures for 1 minute. The result is shown in Fig. 3.29. An improvement of about 1.5-2 times is observed for all samples, with the $\times 9$ -V/III-ratio growth being the best, which agrees with the result in Figs.3.23 and 3.24. Also worth noting is that the 2% difference in the indium concentration does not have any significant impact on the material quality.

The samples were then annealed at lower temperatures(620°C) for durations of up to 105 minutes. The result is shown in Fig.3.30. The results for the three samples all show that there is an additional 1.5-3 times PL intensity improvement over the 1-minute annealing results in Fig.3.29. This is essentially the same result as discussed in the previous section, where the steeper temperature dependence of the over-anneal degradation than that of defect annihilation by annealing led to a twice higher peak

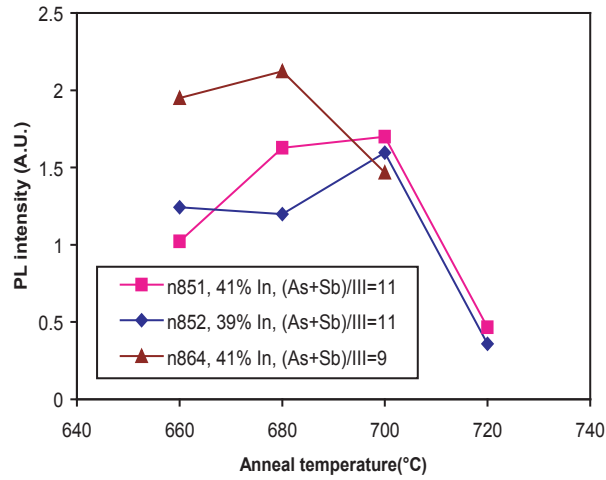


Figure 3.29: PL result for low As+Sb flux growths, after one-minute annealing

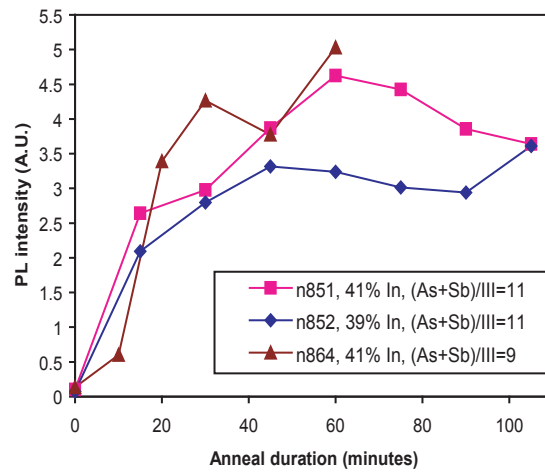


Figure 3.30: PL result for low As+Sb flux growths, after long annealing

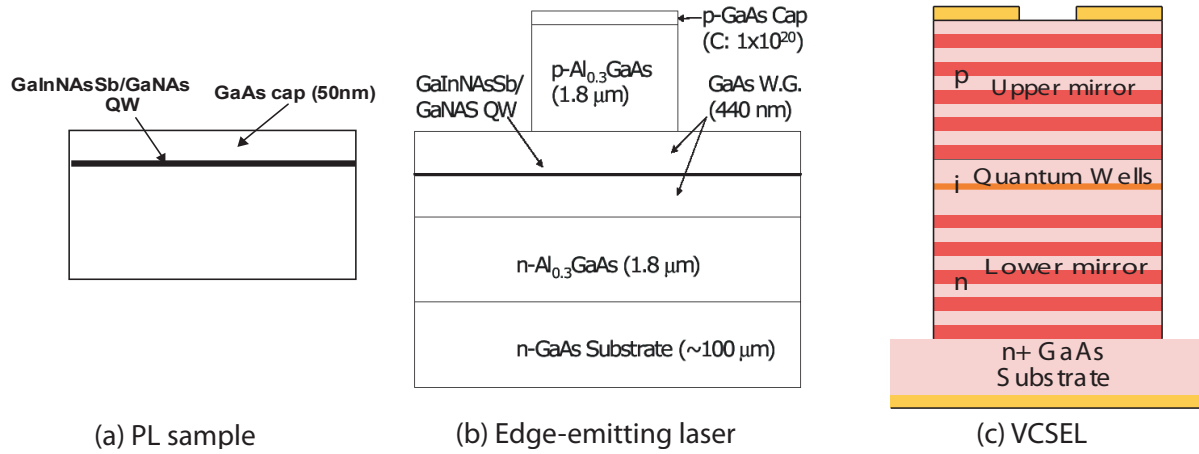


Figure 3.31: PL sample and laser structures studied for this thesis

PL intensity when annealed for a longer duration (tens of minutes) at a lower temperature (60-80°C below the optimum 1-minute annealing temperature). The difference for this study is that the samples in this study are grown under the newly-discovered optimal (As+Sb) flux, resulting in roughly 2X better PL intensity for 1-minute annealing. Therefore, the overall improvement in peak PL intensity by combining the low group-V-flux growth and the low-temperature long-duration annealing is as much as 3-5 times compared to our previous best samples, which were grown under high (As+Sb) fluxes and annealed for 1-minute at higher temperatures.

3.4 Effects of self-annealing

Self-annealing refers to the inevitable in-situ annealing that the QW experiences during growth of actual devices, such as edge-emitting lasers, photo detectors, or VCSELs, because it takes from tens of minutes to several hours to grow the upper structures above the QWs [111,119]. Figure 3.31 shows the three different structures that were grown and studied for this work. PL samples have a 50nm GaAs cap layer, which takes 10–15 minutes. On the other hand, it takes about 2.5 hours to grow the upper cladding for an edge-emitter, and more than 6 hours to grow the upper DBR for a VCSEL. The growth temperature is 580°C for all these upper structures for PL

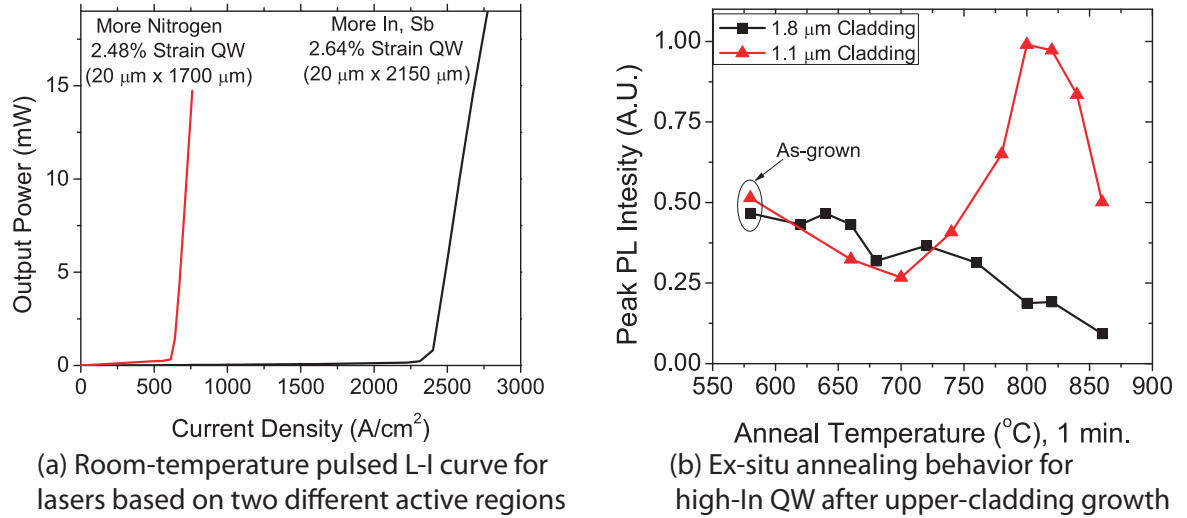


Figure 3.32: Laser result and PL for high-indium QW

samples or laser structures.

10–15 minutes of self-annealing during PL sample growth has not been an issue for the study of GaInNAsSb material, as the PL improvement and blueshift due to the self-annealing seem negligible compared to those due to the additional ex-situ annealing (For example, in Figs.3.16 and 3.17, 0-minute annealing refers to the nominally as-grown sample, which actually experienced 10–15 minutes of self-annealing). On the other hand, the self-annealing has been an important factor for edge-emitters and VCSELs. We have had to anneal edge-emitting lasers at lower temperatures (by 20–40°C) than the 'optimum PL' temperature [52, 96, 120]. And the previous VCSEL operated best when no ex-situ anneal was performed [121]. However, the self-annealing process has not been studied directly, and because of that, the search for the right ex-situ annealing condition has been an ad-hoc blind search process rather than a systematic one, which complicated the laser fabrication.

The need for a more explicit study of the self-annealing process was more urgently felt when we saw poor laser performance from a QW design that showed high PL intensity, when we were trying to achieve low threshold 1.55μm lasers for the first time [122]. Our initial approach to increase the emission wavelength out to 1.55μm

was to increase the In composition (to 41%) to the GaInNAsSb QW. Although this resulted in decent PL, the laser using the high-indium QW showed high threshold current. On the other hand, increasing nitrogen while keeping In at 38% showed similar PL intensity up to $1.55\mu\text{m}$ and enabled us to achieve the lowest-threshold GaInNAsSb laser at $1.55\mu\text{m}$. The discrepancy between the good PL and the poor laser for the high-In QW was attributed to over-annealing the QWs by the self-annealing process, as shown in Fig. 3.32. In this experiment, an undoped laser structure is grown using the 41%-In QW, and compared against a PL sample after 1-minute annealing using the same QW. This structure is identical to an edge-emitting laser, except that the AlGaAs claddings are not doped, to minimize optical loss and carrier loss in the doped layers in order to maximize the PL signal. Fig.3.32 indicates that the QW appears to get over-annealed after 2.5 hours of self-annealing, thus showing decreasing PL intensity with any additional ex-situ annealing. It was hypothesized that higher compressive strain in the QW due to additional In was responsible for this reduced thermal stability of the 41%-In QW against self-annealing, resulting in inferior laser performance despite decent PL quality.

In the previous section, significant improvement in PL intensity was realized by growing QWs at lower (As+Sb) fluxes, but it came with an undesirable side effect of slightly shorter emission wavelength. In order to extend the wavelength again, we tried increasing the indium content to 41% despite the potential problem of reduced thermal stability against self-annealing. Interestingly, we did not find any sign of inferior thermal stability of a 41%-In QW compared to a 39%-In QW as shown in Fig.3.30, which would imply that a 41%-In QW can survive the 2.5-hour self-annealing just as well as a lower-In QW does. Though this contradicts our previous hypothesis that a 41%-In QW is irreversibly damaged during 2.5-hour self-annealing, and the cause of this discrepancy needs more investigation, this encouraged us to explore the 41%-In QWs further in the hope that the 41%-In QW may be thermally stable enough to be useful for GaInNAsSb lasers.

We grew two GaInNAsSb PL samples for emission wavelength around $1.5\mu\text{m}$, one with 39% In and the other with 41% In. They were both grown at $\times 9$ (As+Sb)/III flux ratio as measured in BEP(Beam equivalent pressure) and at the growth temperature

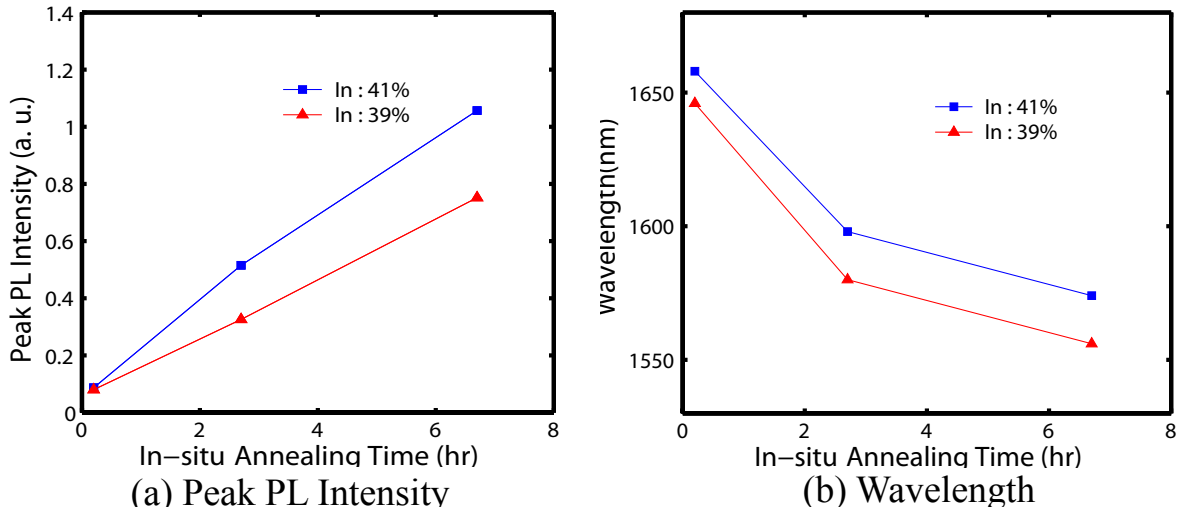


Figure 3.33: PL intensity and wavelength after self-annealing of plain PL samples

of 440°C , to achieve the optimum PL intensity as described in the previous section. After growth, each wafer was cleaved into quarter-wafer pieces, and 2 pieces of each wafer are loaded back into the MBE chamber. One piece of each wafer is annealed in the MBE chamber at the GaAs/AlGaAs growth temperature of 580°C (measured by the pyrometer) for 2.5 hours to emulate the upper cladding growth for edge-emitting lasers, and the other piece is annealed at the same temperature for 6.5 hours to emulate the upper DBR growth for VCSELs. The growth of each PL sample involves a 12-minute growth of a 50-nm GaAs cap layer, so the total self-annealing time is 2.7 hours and 6.7 hours for each piece, respectively. Arsenic pressure was applied during the in-situ annealing to prevent arsenic desorption from the surface.

Figure 3.33 shows the PL peak intensity and wavelength after self-annealing only, with no additional ex-situ annealing. Our concern with the 41%-In was that it may degrade by over-annealing when it is 'self-annealed' during the growth of upper structures of lasers, but we did not see any such degradation from this result.

Moreover, when we apply additional 1-minute ex-situ annealing to the 41%-In samples after 0, 2.5-hour, and 6.5-hour self-annealing, we see additional PL improvement and wavelength blueshift for 2.5-hour and 6.5-hour self-annealed samples as

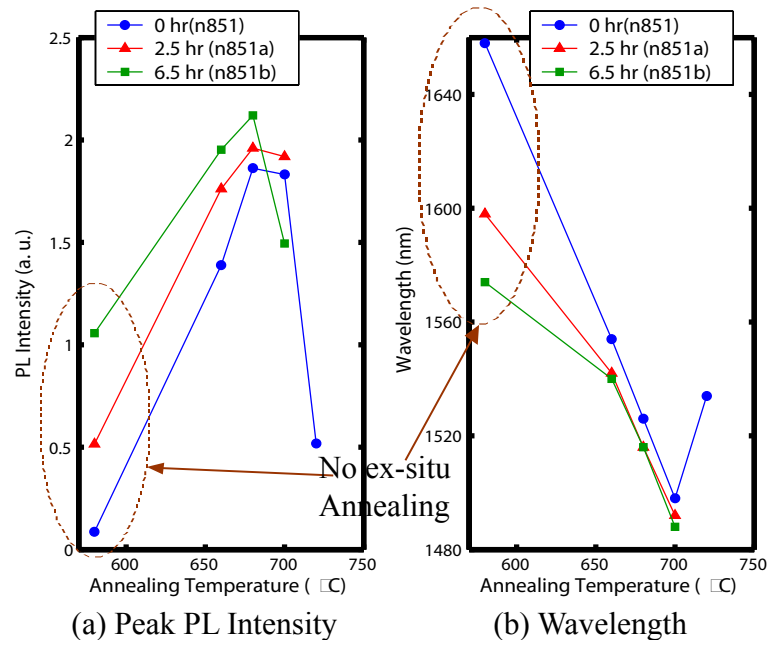


Figure 3.34: Results of additional ex-situ 1-minute annealing of 41%-In plain PL samples after 0-, 2.5-, and 6.5-hour self-annealing

shown in Fig. 3.34, in the same way as we see without self-annealing. Although longer self-annealing results in higher PL intensity and shorter wavelength for lower ex-situ annealing temperatures, all three samples reach similar PL intensity and wavelength for higher ex-situ annealing temperature. Moreover, longer self-annealing gives higher optimum PL intensity, although the difference is not large. Now it seems very clear that hours of self-annealing during edge-emitter upper-cladding growth and even thicker VCSEL upper-DBR growth does not cause over-annealing degradation, even for a high In content of 41%.

This is a very encouraging result, but we still had doubts because of our previous disappointing experience with 41%-In QWs. Noticing that the PL samples differ from actual laser structures in that PL samples do not have doped AlGaAs claddings, we grew another PL sample with a more laser-like structure to more faithfully reproduce the conditions that a QW is placed in during self-annealing. This laser-like PL structure is essentially an edge-emitting laser structure, only with thinner claddings for more efficient PL measurement. It has a 500-nm thick $\text{Al}_{0.4}\text{Ga}_{0.6}\text{As}$ bottom cladding with n-type doping of 10^{18}cm^{-3} and a 100-nm thick $\text{Al}_{0.4}\text{Ga}_{0.6}\text{As}$ top cladding with p-type doping of 10^{18}cm^{-3} , while an edge-emitter structure has $1.8\mu\text{m}$ -thick claddings on both sides. After growth, this laser-like PL sample was cleaved into quarter wafers and two quarters pieces were annealed for 2.5 and 6.5 hours respectively in the MBE chamber, at the GaAs/AlGaAs growth temperature of 580°C .

The result of PL measurement for ex-situ 1-minute annealing on the self-annealed laser-like PL samples shown in Fig.3.35 shows a very similar trend with Fig.3.34. Some PL improvement and wavelength blueshift happens in-situ during self-annealing, but definitely no degradation happens due to self-annealing. There is also additional PL improvement and wavelength blueshift by ex-situ annealing, which is an indication that the QW is not over-annealed by self-annealing, although the QW seems to have been almost fully annealed after 6.5 hours of in-situ self-annealing. In addition, the similarity of annealing results for laser-like PL samples (Fig.3.35) to those for plain PL samples (Fig.3.34) implies that the observed annealing properties are truly intrinsic properties of the QW, rather than extrinsic properties influenced by the presence of nearby AlGaAs layers or their doping levels, or distance of the QW to the surface or

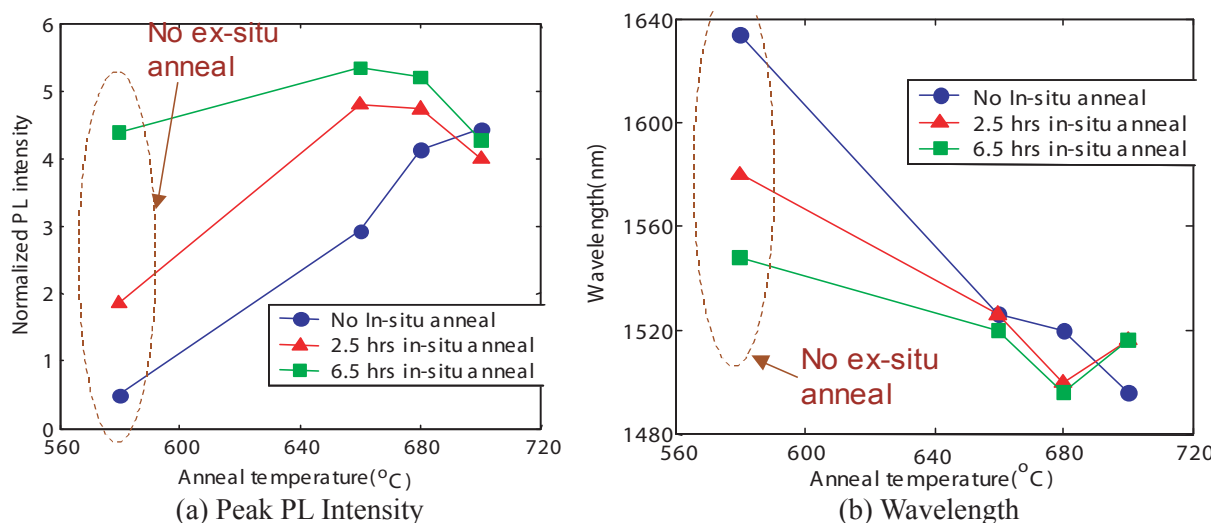


Figure 3.35: Results of additional ex-situ 1-minute annealing on "Laser-like" PL samples with 41%-In QW

the substrate.

It becomes clearer that the QW is far from being fully or overly annealed even after 6.5 hours of self-annealing, when we apply long and cool ex-situ annealing to the samples. Fig.3.36 shows that additional 2–3 times improvement in PL intensity is obtained by ex-situ annealing, even after many hours of in-situ self-annealing. The apparent redshift of wavelength with longer annealing seems to contradict the usual observation of blueshift under annealing, but we suspect this is due to the non-uniformity of wavelength over the wafer. There is about 40nm difference in PL emission wavelength between the center and the edge of a wafer, with the center emitting at a longer wavelength. This particular long-annealing experiment was executed in such a way that pieces closer to center are annealed longer. If we remove the effect of this wavelength nonuniformity, we expect to see negligible wavelength shift after 20 minutes.

These laser-like PL samples were also useful as benchmark samples for optimizing the annealing process for actual edge-emitting laser or VCSEL wafers. When we grow edge-emitting lasers or VCSELs, we grow a laser-like PL sample with nominally the same QW composition along with lasers, preferably in the same day or at least

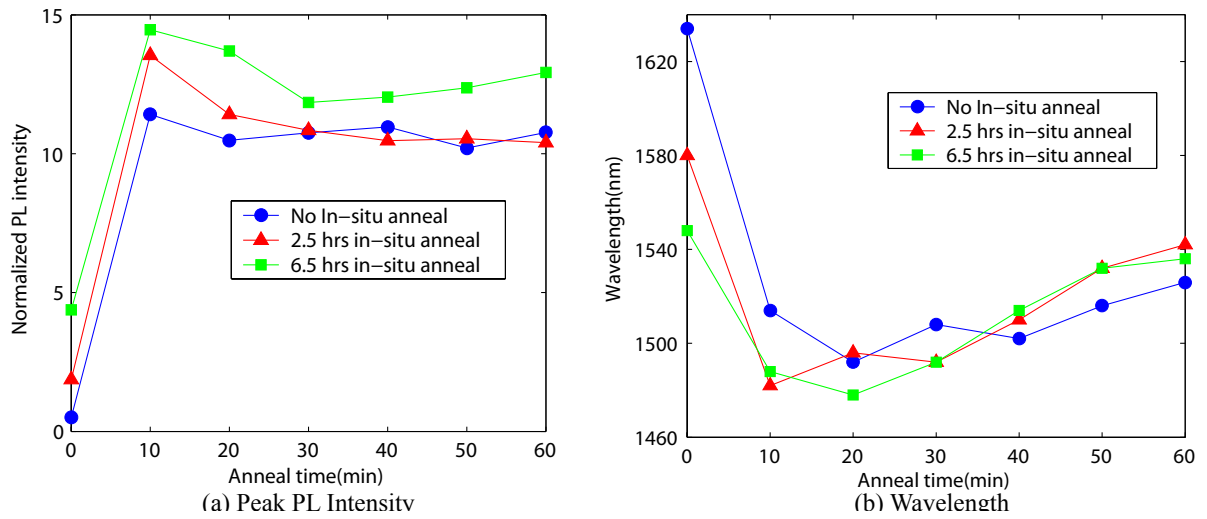


Figure 3.36: Results of long-annealing at 620°C on laser-like PL samples with 41%-In QW

within a few days. We determined the optimal annealing temperature and duration by annealing and measuring the laser-like PL sample, and applied the same annealing conditions to the laser wafers. This enabled us to determine the annealing conditions at the beginning of laser fabrication, instead of having to anneal different wafer pieces at a few different temperatures, fabricate them all into lasers, and then pick a good one by measuring the completed lasers. In addition, as discussed in 3.2, annealing at lower temperatures for long durations resulted in higher PL intensity and easier process control than the 1-minute annealing at a few randomly chosen temperatures, which had been previously administered. The results of edge-emitting lasers and VCSELs using the new growth and annealing conditions are presented in the following chapters.

Chapter 4

Edge-emitting lasers

4.1 Laser structure

Edge emitting lasers were grown using the new growth and annealing methods discussed in the previous chapter. The laser structure is shown in 4.2, which is a simple separate confinement heterostructure(SCH) ridge waveguide type. The active layer is embedded at the center of the 460nm-thick GaAs waveguide core region. The bottom and top cladding are 1.8 μ m-thick Al_{0.33}Ga_{0.67}As layers. The bottom cladding is doped n-type with Si, with the lower half doped at $3 \times 10^{18} \text{cm}^{-3}$ and the upper half at $7 \times 10^{17} \text{cm}^{-3}$. The upper cladding is doped p-type with C, with the upper half doped at $3 \times 10^{18} \text{cm}^{-3}$ and the lower half at $6 \times 10^{17} \text{cm}^{-3}$. 50-nm thick GaAs cap layer is doped with C at $1 \times 10^{20} \text{cm}^{-3}$, to facilitate the formation of low-resistance Ohmic contacts.

The active region is a 7-nm Ga_{0.59}In_{0.41}N_{0.028}As_{0.942}Sb_{0.03} QW embedded between a pair of 20-nm GaN_{0.03}As_{0.97} barrier layers. A laser-like PL sample, as discussed in the previous chapter, was first grown and annealed at 620°C for a number of different durations in the RTA chamber in the SNF(Stanford Nano-Fabrication) facility, to determine the appropriate annealing condition. As shown in Fig.4.1, the optimum PL intensity was achieved at about 10 minutes. To compare the effects of under-, optimum-, and over-annealing the lasers, the wafer was cleaved into quarters after growth and three of the quarter pieces were annealed at different durations (5,10, and

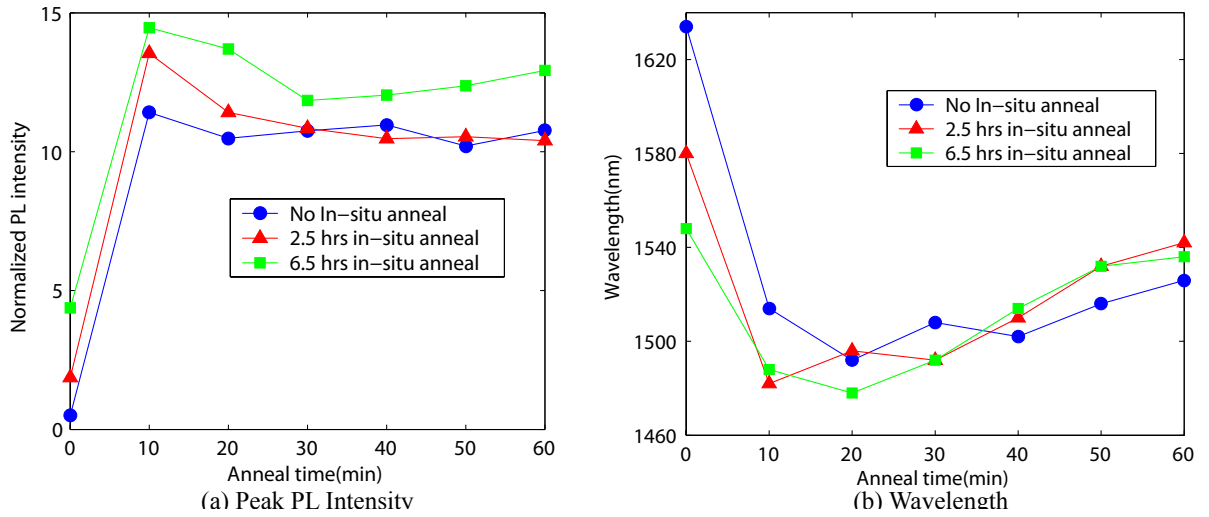


Figure 4.1: Results of long-annealing at 620°C on laser-like PL samples with 41%-In QW

15 minutes) at 620°C. Unfortunately, the 5-minute and 10-minute annealed samples were damaged during later fabrication due to sample mishandling.

After annealing, ridge widths of 5, 10, 20 μm were defined using a combination of lift-off of evaporated Ti/Au/Pt contact layer and a self-aligned etch was done through the active region to the top of the bottom AlGaAs cladding layer. The etch depth was monitored by reflectivity oscillations using an 820nm laser. The wafer was then thinned to 120 μm and Au/Ge/Ni/Au n-contact layer was deposited on the back side. Laser bars were manually cleaved, with the cleaved facets naturally forming mirrors. Lasers were mounted epitaxial-side up on an oxygen-free copper carrier with InSn solder and the copper carrier was mounted on a thermoelectric cooler, which in turn was mounted on a copper cooling block. More details about laser mounting and testing can be found in Ref. [55].

4.2 SQW laser performance

Figure 4.3 shows the LI curve for the laser under pulsed and CW mode operation at an ambient temperature of 15°C. The threshold current densities are 540A/cm² in pulsed

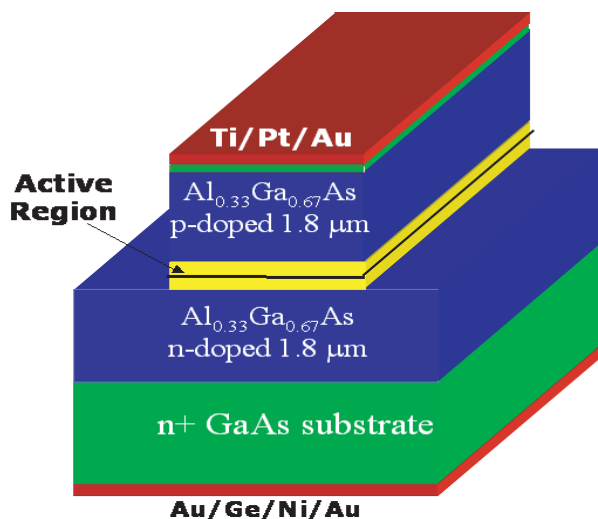


Figure 4.2: Schematic of the edge-emitting laser.

mode and $554\text{A}/\text{cm}^2$ in CW mode. The external efficiency was about 40%, although this number was a little noisy from sample to sample due to slight alignment errors between the laser and the detection optics. The maximum output power was 750mW (limited by the current supply, not the laser itself) in pulsed mode and 230mW in CW mode, and the lasing wavelength is about $1.49\mu\text{m}$ at thermal rollover, as shown in Fig.4.4.

The output powers and threshold current densities are on par with the results of previous generations of lasers (e.g., CW threshold density $370\text{A}/\text{cm}^2$, CW power 250mW, pulsed power 750mW for $1.55\mu\text{m}$), but admittedly, it is rather disappointing and surprising that the significant improvement in PL intensity as discussed in the previous chapter did not result in improvement in laser performance.

As shown in Fig.4.5 and reported by Infineon researchers [5], the PL intensity from GaInNAs(Sb) QWs and the laser threshold using such QWs have shown a strong negative correlation (i.e., higher PL intensity leads to lower threshold current). Our group has also observed such correlation multiple times in the past, and PL intensity has been a very reliable guide to the expected laser threshold current. One notable exception to this was encountered when we tried to increase the emission wavelength

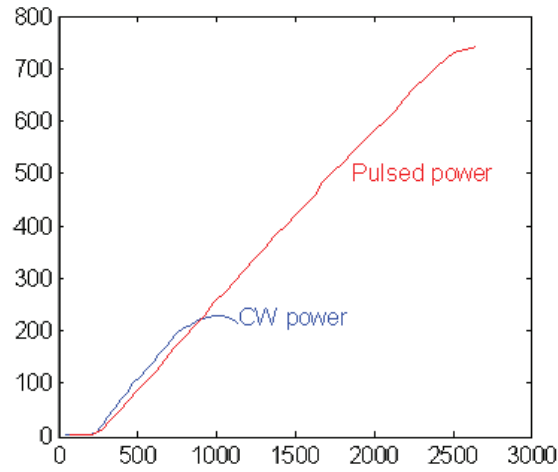


Figure 4.3: CW and Pulsed L-I curve for a $2050\mu\text{m}\times 20\mu\text{m}$ laser.

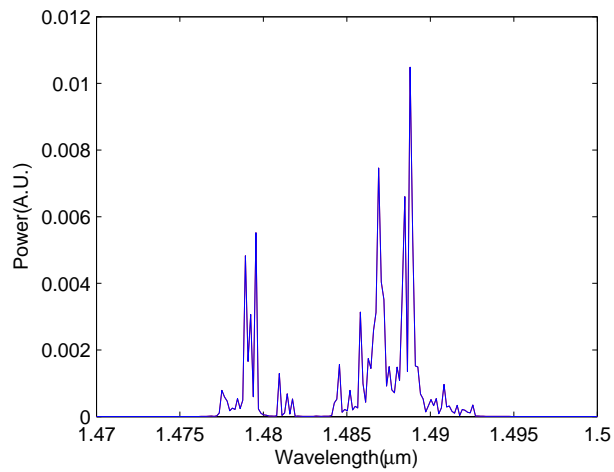


Figure 4.4: CW spectrum of the a $2050\mu\text{m}\times 20\mu\text{m}$ laser at thermal rollover at a chuck temperature of 15°C

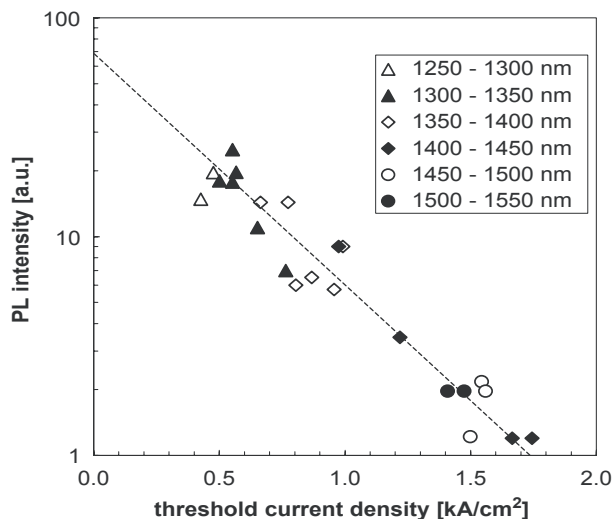


Figure 4.5: PL intensity versus laser threshold current density [5]

by adding more In to the QW [122]. The PL intensity was good but the laser threshold was quite high. High strain in the QW and the resultant low thermal robustness of the QW against 2.5 hours of self-annealing during cladding layer growth were suspected to be the cause of this departure from the previous correlation between PL and threshold. As we decided to have 41% In in the QW for this generation of lasers in order to compensate for the shorter wavelength from lower group-V flux growth, we were once again concerned about this thermal robustness problem. But the self-annealing experiments presented in the previous chapter assured us that the QWs are robust enough against the self-annealing during laser cladding growth. Now that the QW quality is not affected during laser growth, a new explanation has to be found as to why PL improvement did not translate into laser performance improvement.

Throughout previous optimizations of QW growth and annealing for better laser performance based on PL measurement (e.g., deflection plates, addition of Sb, and GaNAs barriers), the following assumptions were made, either explicitly or implicitly: 1) PL technique is sensitive to the defects in the QW material, and 2) laser threshold is most dependent on the number of defects of the GaInNAsSb QW. As a novel material with a large miscibility gap, GaInNAsSb seems to have satisfied these assumptions,

resulting in the observed strong correlation between PL intensity and laser threshold. In the following sections, we will investigate whether these two assumptions still hold for the GaInNAsSb QWs and lasers studied for this thesis. The second assumption is examined first.

4.3 Recombination mechanisms

Although recombination current due to defects has been an important factor for GaInNAsSb-based laser threshold, it is not the only component of threshold current. The threshold current for an edge-emitting semiconductor is usually expressed according to:

$$I_{th} = qVR(n_{th}) \quad (4.1)$$

$$R(n_{th}) = An_{th} + Bn_{th}^2 + Cn_{th}^3 + R_{leak} \quad (4.2)$$

where I_{th} is the threshold current, q is the charge of an electron, V is the volume of the active region, n_{th} is the carrier density in the active region, and R_{leak} is the leakage rate out of the active region. A, B, and C are coefficients for monomolecular, radiative, and Auger recombinations, respectively.

The first-order term is due to recombination through defects, i.e., Shockley-Read-Hall recombination. Assuming Boltzmann statistics, the defect recombination rate is given by: [123, 124]

$$R_d = \frac{np - n_i^2}{(n^* + n)\tau_h + (p^* + p)\tau_e} \quad (4.3)$$

$$n^* = N_c \exp\left(\frac{E_t - E_c}{kT}\right) \quad (4.4)$$

$$p^* = N_v \exp\left(\frac{E_v - E_t}{kT}\right), \quad (4.5)$$

where E_t , E_c , and E_v are the energy levels of the defects, the conduction band minimum, and the valence band maximum, respectively, and τ_e and τ_h are electron

and hole capture times, respectively. The capture times are related to the thermal velocity, the capture cross-section, and the defect concentration as follows:

$$\frac{1}{\tau_e} = v_{e,th}\sigma_e N_t \quad (4.6)$$

$$\frac{1}{\tau_h} = v_{h,th}\sigma_h N_t. \quad (4.7)$$

The most effective recombination centers are those with energy levels close to the middle of the gap, so-called deep-level traps. Assuming high injection and charge neutrality which is typical for laser applications (i.e., $n = p \gg n_i$) and deep-level traps such that $n = p \gg n^*, p^*$), Eq.4.3 reduces to:

$$R_d = \frac{n}{\tau_h + \tau_e}. \quad (4.8)$$

Thus, defect recombination follows a linear dependence on carrier density in the active region of lasers, and the defect recombination appears as $R_d = An_{th}$ in Eq.4.1 with $A = 1/(\tau_h + \tau_e)$.

Spontaneous recombination of electron-hole pairs gives rise to the second-order term Bn_{th}^2 when Boltzmann statistics is assumed, because, following Fermi's Golden Rule, the spontaneous recombination rate is proportional to the product of the electron and hole Boltzmann factors.

The third-order term (Cn_{th}^3) is due to Auger recombination, whereby an electron-hole pair recombines and transfers its energy to another carrier, exciting it to a higher energy state. Applying Fermi's Golden Rule to calculate the transition rate while assuming charge neutrality and Boltzmann statistics, the rate is proportional to the cube of the carrier density, thus giving the third order term. The Auger coefficient C is known to increase exponentially for smaller bandgaps [125], and it is also known that InGaAsP/InP-based long-wavelength lasers suffer from Auger recombination [126, 127]. Operating in the same wavelength range (therefore similar bandgap range) as InGaAsP/InP lasers, GaInNAsSb/GaNAs lasers are also very likely to suffer from significant Auger recombination in the QW.

The last term, leakage current, is due to the carrier leakage through thermionic

emission over a heterostructure barrier of finite height. The rate of carrier leakage is theoretically derived [128–130] to be:

$$J_{leak} = \frac{4\pi q k^2 T^2 m}{h^3} \exp\left(-\frac{E_b - E_f}{kT}\right) \quad (4.9)$$

This equation is straightforward, but it only gives an upper bound to the leakage current for a semiconductor laser, because this equation was derived assuming that carriers do not come back after going over the potential barrier, while in a semiconductor QW laser carriers may come back by diffusion or be recaptured before being lost by diffusing away or recombining. Actual leakage current is typically only 20%–30% of the value suggested by Eq.4.9 [125] and more complete analysis requires consideration of diffusion parameters [125]. However, despite this complication, the exponential dependence on temperature would always be valid.

In our GaInNAsSb/GaNAs QW lasers, there are three areas (layers) to which carriers can leak.

- AlGaAs cladding layers
- GaAs SCH region
- GaNAs barriers

For the Al_{0.33}Ga_{0.67}As cladding layers used for this study, the hetero-barrier between the GaAs SCH layer and the doped AlGaAs cladding layer is as high as 400meV [131], so leakage over to the AlGaAs claddings is expected to be very small (< 1A/cm²) [132].

The band offset between the GaAs SCH layer and the GaInNAsSb QW is ~500meV for electrons and ~160meV for heavy holes, as shown in Fig.4.6. This is larger than or at least as large as the band offsets for InGaAs/GaAs lasers (Fig.4.7), for which leakage to the GaAs SCH region is known to be not problematic [130]. Therefore, it is fair to assume that leakage to the GaAs SCH region is not an issue for GaInNAsSb/GaNAs lasers either.

The band offsets for the GaNAs/GaInNAsSb interface are however much lower, with ~160meV for electrons and <100meV for heavy holes. This can lead to a large

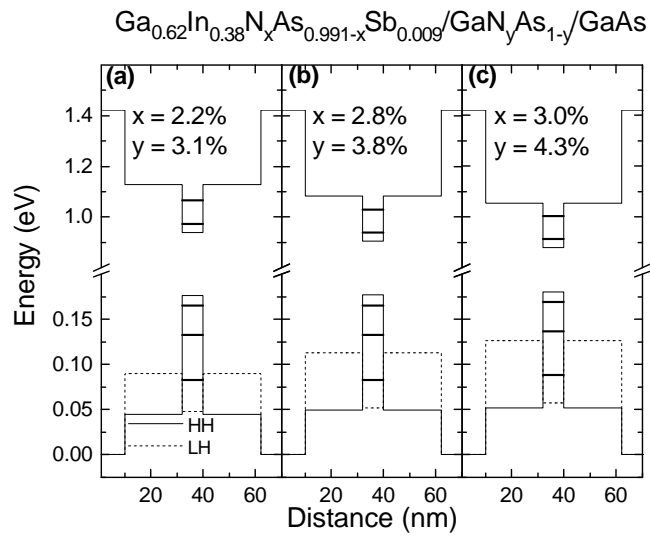


Figure 4.6: Band offsets of GaInNASb/GaNAs QWs measured by contactless electroreflectance. [133]

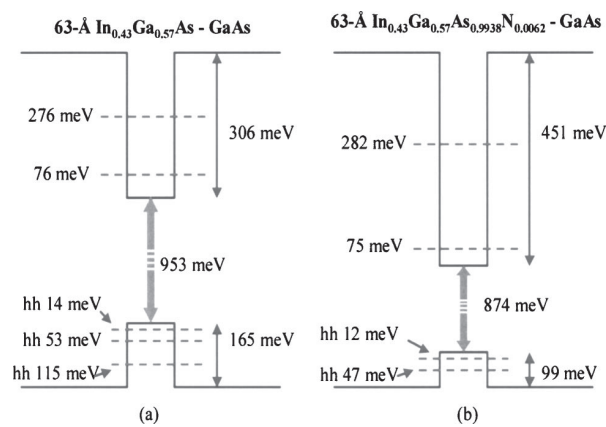


Figure 4.7: Band offsets of InGaAs/GaAs and InGaAsN/GaAs [6]

carrier population in the GaNAs barriers. This large population would not be a problem if the quality of GaNAs material is high, with most of the carriers eventually relaxing to lower QW energy levels from which they recombine radiatively to give rise to spontaneous emission or optical gain. On the other hand, if the quality of the GaNAs barriers is poor, the carriers in the barriers will recombine non-radiatively, giving rise to a 'leakage current'. This leakage current would be very sensitive to temperature, as the carrier population in the barrier has an exponential dependence on temperature through the Boltzmann factor in Eq.4.9. It has been found, unfortunately, that GaNAs layers are of relatively poor quality with a high concentration of defects [73,92,97], so it is expected that leakage to the GaNAs barriers is a significant component of threshold current [132]. From purely theoretical considerations, use of GaAs barriers instead of GaNAs would be a natural solution to this problem, but in practice GaNAs was introduced intentionally in order to overcome the material quality problem by providing strain compensation to the highly strained GaInNAsSb/GaAs QWs when emission wavelengths longer than $1.4\mu\text{m}$ are required [3,23,28,79].

A closer look at the strain and bandgap of a GaInNAsSb/GaNAs QW (Fig.4.6) reveals that the leakage problem is bigger than one might expect from the Boltzmann factor alone, because the in-plane light hole mass in the GaNAs layer is a few times larger than the in-plane heavy hole mass in the GaInNAsSb layer, due to the strain effects [134]. Because the in-plane mass is proportional to the density of states, the LH levels in the GaNAs barrier has a few times larger density of states compared to the HH levels in the GaInNAsSb. Larger width of confinement for the holes in the GaNAs barriers also increases the number of confined levels, further increasing the number of available hole states in the GaNAs barrier. A simplified simulation of the QW shows the severity of the situation, with the rapidly increasing density of states above the barrier leading to significant hole population in the higher energy levels (Fig.4.8).

Components of threshold current other than the spontaneous emission term represent unnecessary loss of carriers, increasing the threshold current and also degrading other performance metrics via increased junction temperature. For GaInNAsSb QWs, we have been focusing on the defect recombination term for minimization of

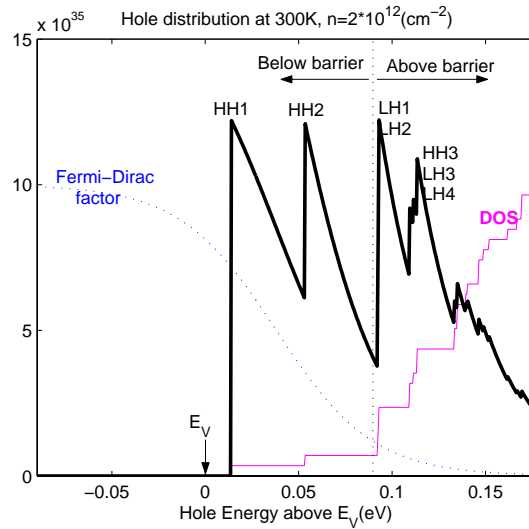


Figure 4.8: Hole distribution at 300K.

the threshold current, by measuring the PL intensity. However, other nonradiative terms (Auger and leakage) have to be considered to achieve lower laser threshold as discussed above. Moreover, Auger and leakage terms also degrade another important performance criteria, namely the temperature stability of lasers, so identification and reduction of these terms is even more important. On the other hand, poor temperature stability of a laser can be a sign of presence of Auger or leakage processes. The relationship between the components in the laser threshold and the temperature stability is discussed in the following sections.

4.4 Temperature stability : Theory

Temperature stability of laser threshold is a very important parameter for commercial viability of semiconductor lasers, because poor temperature stability often leads to requirements of additional temperature control or bias point control, driving the system cost higher. Poor temperature stability of InGaAsP/InP lasers due to their small conduction band offset and Auger recombination is one of the reasons of high cost of semiconductor laser systems for optical communications. The promise of

better temperature stability thanks to a higher conduction band offset was one of the important motivations for pursuing dilute nitride research [17]. This promise has been more or less realized for 1.3 μm lasers [30–35, 37–39, 130], but it has not been really realized for 1.5 μm lasers. Before jumping into our experimental results of temperature stability measurements, we first discuss the theory of temperature stability of laser threshold.

Temperature stability of threshold current is usually expressed by using the characteristic temperature T_0 , assuming the following exponential relationship [125]:

$$I_{th} = I_{th0} \exp\left(\frac{T}{T_0}\right). \quad (4.10)$$

T_0 can be calculated from measurements of threshold vs. temperature using the following equation [127]:

$$\frac{1}{T_0} = \frac{d[\ln(I_{th})]}{dT} \quad (4.11)$$

The threshold current can be decomposed into a few components according to Eq.4.1, and each component shows different characteristic temperature when it is dominant, as discussed below. Eq.4.1 is repeated here for easy reference.

$$I_{th} = qV(A n_{th} + B n_{th}^2 + C n_{th}^3 + R_{leak}) \quad (4.12)$$

The temperature dependence of the recombination coefficients A, B, and C is expected to be [135, 136]:

$$A \propto T^{1/2} \quad (4.13)$$

$$B \propto T^{-1} \quad (4.14)$$

$$C \propto \exp\left(-\frac{E_a}{kT}\right) \quad (4.15)$$

where E_a is the activation energy for the Auger process.

The threshold carrier density n_{th} follows a slightly super-linear dependence on temperature [127]:

$$n_{th} \propto T^{1+x} \quad (4.16)$$

where $x = 0$ in an ideal QW in an ideal semiconductor laser. For real QWs for which we have to consider occupation of higher subbands, carrier spillover, or temperature-dependent IVBA, x becomes positive, making n_{th} more sensitive to temperature.

If defect recombination (An_{th}) is dominant,

$$T_0 = \frac{T}{1.5 + x}. \quad (4.17)$$

If spontaneous recombination (Bn_{th}^2) is dominant,

$$T_0 = \frac{T}{1 + 2x}. \quad (4.18)$$

If Auger recombination (Cn_{th}^3) is dominant,

$$T_0 = \frac{T}{3 + 3x + E_a/kT} \quad (4.19)$$

where E_a is the activation energy for the Auger process. E_a is expected to be 20–30meV for phonon-assisted processes and ≤ 70 meV for direct processes [127].

On the other hand, the leakage current is proportional to $\exp(-\frac{E_{barrier}}{kT})$, which leads to

$$T_0 = T * \frac{kT}{E_{barrier}}. \quad (4.20)$$

if leakage current is dominating the threshold current. ($E_{barrier}$ is the effective height of the energy barrier.) T_0 is thus larger for lower barriers and smaller for higher barriers, although leakage current is less likely to be dominant for higher barriers. For ~ 100 meV barriers for holes in GaInNAsSb/GaNAs QWs, the leakage current could actually dominate the threshold current density, driving T_0 lower ($\sim T/4$).

In real semiconductor lasers, x is usually larger than 0, but smaller than 1 by enough margin, so that T_0 is relatively large when the threshold current is dominated by defect recombination or spontaneous recombination, and T_0 is smaller when the threshold is dominated by Auger or leakage processes. For example, GaAs/AlGaAs QW lasers and InGaAs/AlGaAs QW lasers show high T_0 values (150–180K for GaAs/AlGaAs lasers, and ≥ 200 K for InGaAs/AlGaAs QW lasers [125]) because

they are dominated by the spontaneous recombination term. On the other hand, InGaAsP/InP lasers in the 1.3–1.55 μm range exhibit low T_0 (50–70K) due to Auger recombination and leakage.

For 1.3 μm GaInNAs/GaAs QW lasers, T_0 values above 100K are routinely reported, along with low threshold current density (250–320A/cm²) [30, 31, 35, 39]. On the other hand, GaInNAsSb/GaNAs QW lasers for $\geq 1.5\mu\text{m}$ have shown an interesting tradeoff between low threshold current density and high temperature stability. Our first generation 1.5 μm laser had good temperature stability ($T_0=139\text{K}$) but high threshold current density (1.06kA/cm²) [51]. After improving the material quality based on PL intensity measurements, the second generation of 1.5 μm lasers showed significantly improved threshold current density(580A/cm²) but the temperature stability degraded more significantly ($T_0 = 73\text{K}$) [137]. This has been explained by reduction of the defect recombination term by improving the QW material quality. Before the improvement, the threshold was dominated by defect recombination leading to relatively high T_0 . If we reduce the defects in the QW, then Auger recombination or leakage seem to dominate the threshold current, leading to much lower T_0 .

It can be easily expected that 1.5 μm GaInNAsSb/GaNAs lasers would experience more Auger recombination (due to smaller bandgap) and more leakage current (due to lower GaNAs barrier than GaAs) than 1.3 μm GaInNAsSb/GaAs lasers. Therefore, lower T_0 for 1.55 μm lasers is not surprising. However, it has not been really clear whether Auger recombination or leakage is more responsible for the lower temperature stability, and this issue requires more research.

In order to gain more insight into which process is dominating the threshold current density, temperature stability measurement results are presented for the latest GaInNAsSb/GaNAs QW lasers in the next section. T_0 is an important parameter for its own right, too, as it is a measure of laser stability. A few different QW structures were tried looking for the possibility of improving T_0 without excessive increase in the threshold current density. In addition, measurement results from a segmented contact method [138, 139] are presented that gave us more clue about the origin of non-radiative recombination in the GaInNAsSb/GaNAs QW lasers.

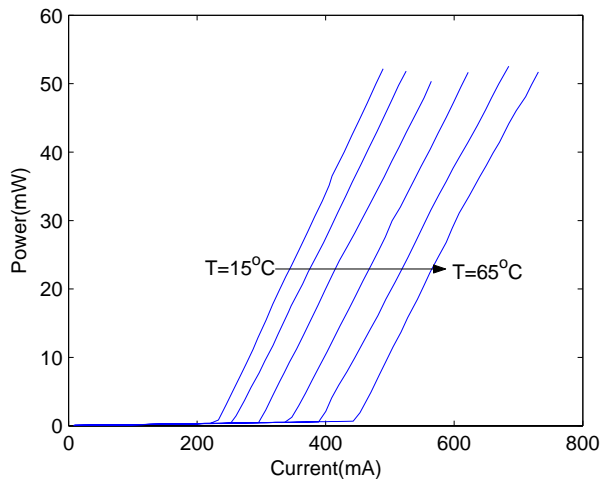


Figure 4.9: Pulsed L-I curve for a $2050\mu\text{m} \times 20\mu\text{m}$ laser.

4.5 Temperature stability measurements and Origin of nonradiative recombination

Temperature stability measurements for the same laser as in Fig.4.3 and Fig.4.4 are shown in Fig.4.9 and Fig.4.10.

Similar to previous low threshold $1.5\mu\text{m}$ or $1.55\mu\text{m}$ lasers, this laser has a relatively low T_0 value, which implies that the threshold current is mainly dominated by Auger or leakage processes. Low T_0 also means that the threshold current has a steep dependence on temperature. Fig.4.9 shows that the threshold nearly doubles as the temperature changes from 15° to 65°C . In an effort to improve temperature stability, we grew two more different QW structures as shown in Fig.4.11. In addition to the standard single QW with 20nm GaNAs barriers that we have been discussing up to this point, we also grew a 3QW laser and a SQW laser with thinner(10nm) GaNAs barriers. With the 3QW lasers, we wanted to reduce the required gain per QW, thus reducing n_{th} and Auger recombination. With the thin-barrier lasers, we wanted to reduce the amount of low-quality GaNAs material, in order to reduce the leakage problem. We did not go all the way to removing GaNAs layers altogether, because our previous attempts to use GaAs barriers resulted in very high laser threshold and

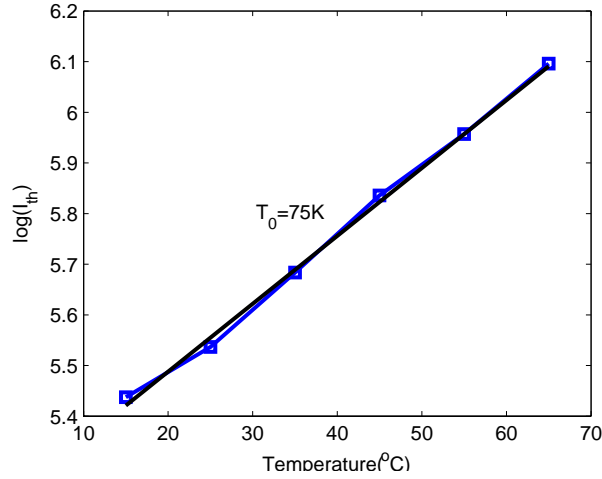


Figure 4.10: T_0 for a $2050\mu\text{m} \times 20\mu\text{m}$ laser.

high T_0 which indicated significantly degraded GaInNAsSb quality due to lack of strain compensation. It was hoped that 10nm GaNAs barriers would strike a right balance between reducing barrier material (to reduce leakage problem) and providing enough strain compensation (to improve GaInNAsSb quality).

T_0 measurements for 3QW and thin-barrier SQW lasers are shown in Fig.4.12 and Fig.4.13. 3QW and thin-barrier SQW lasers show improved T_0 compared to the standard SQW with 20nm GaNAs barriers, but the improvement is not large : only 10–15K, and 85–90K is still a relatively low T_0 with poor temperature stability, which implies that Auger and/or leakage processes are still dominant. Moreover, this marginal improvement in T_0 is obtained at the cost of higher threshold current density. The threshold current density of a thin-barrier SQW laser was $855\text{A}/\text{cm}^2$ in pulsed mode, and the 3QW laser showed threshold current density of $1263\text{A}/\text{cm}^2$ in pulsed mode. For practical purposes, thin-barrier SQW or 3QW structures provide no advantage over the standard SQW structure.

We also grew another 3 sets of lasers with the same standard SQW, 3QW, and thin-barrier QW structures, with the only difference of higher nitrogen content, in order to see the effect of higher nitrogen content: 3.1% instead of 2.8%. Their results are shown in Fig.4.14. The 3.1%-N QWs show a similar trend to the 2.8%-N QWs,

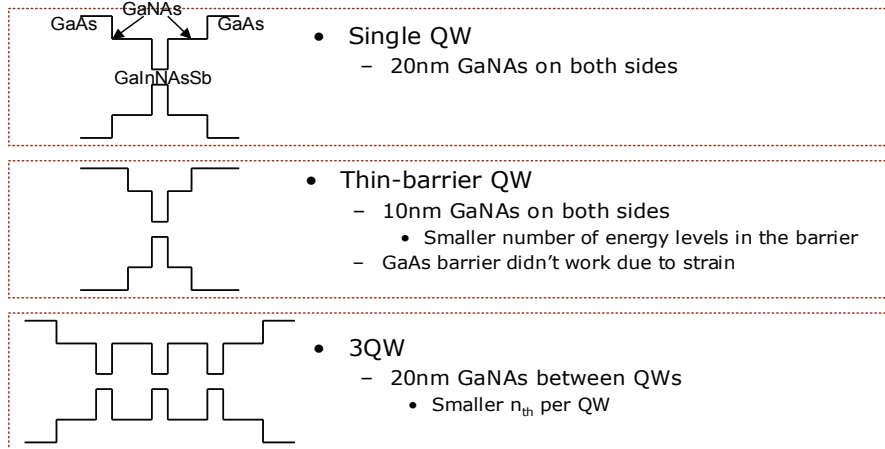
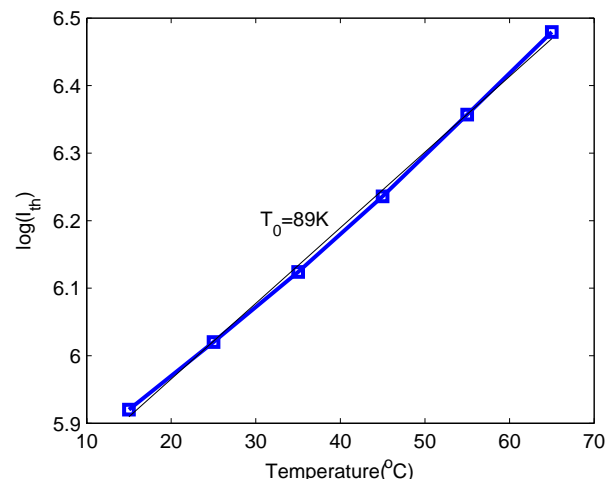


Figure 4.11: 3 different QW structures

Figure 4.12: T_0 for a thin-barrier laser, $2050\mu m \times 20\mu m$.

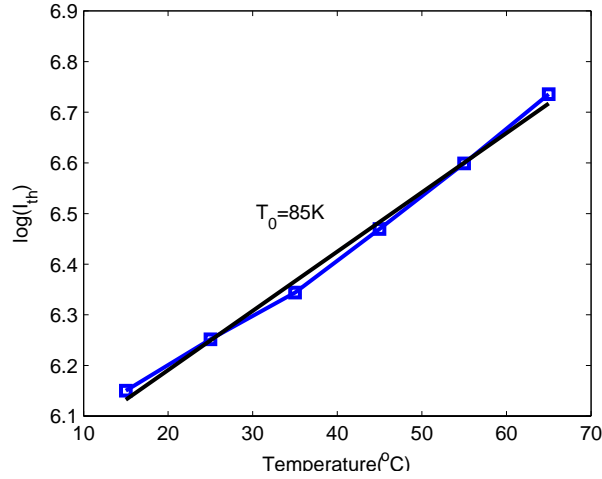


Figure 4.13: T_0 for a 3QW laser, $2050\mu\text{m} \times 20\mu\text{m}$.

with the 3QW and thin-barrier SQW lasers showing marginal (if at all) improvement in T_0 at the cost of a significant increase in the threshold. Higher nitrogen in the QWs generally led to higher threshold and lower T_0 . This can be explained equally well by increased Auger recombination due to a smaller bandgap, or by increased leakage due to decreased light-hole barrier¹.

Low T_0 for all three QW structures indicate that highly temperature-sensitive carrier loss mechanisms (i.e., Auger and leakage) are dominating the laser threshold. This same conclusion that Auger and/or leakage is dominant has been obtained on our previous generations of lasers [52, 55, 132], especially after improving QW quality and laser threshold by reducing defects in the QW. Unfortunately, we have not been able to clarify which one of the two mechanisms is dominating the laser performance. This has to be determined in order to further reduce laser threshold and increase T_0 .

In order to identify the most dominant mechanism in the laser threshold, the laser samples were characterized using segmented contact method by our collaborators at Cardiff University, UK. Under this method, an edge-emitting laser bar is fabricated

¹Due to limited number of effusion cells in the MBE growth chamber and the inverse proportionality of nitrogen incorporation with respect to the growth rate, we are forced to put more nitrogen in the GaNAs layer as we increase nitrogen in the GaInNAsSb layer. With more nitrogen, the tensile strain of the GaNAs layer increases.

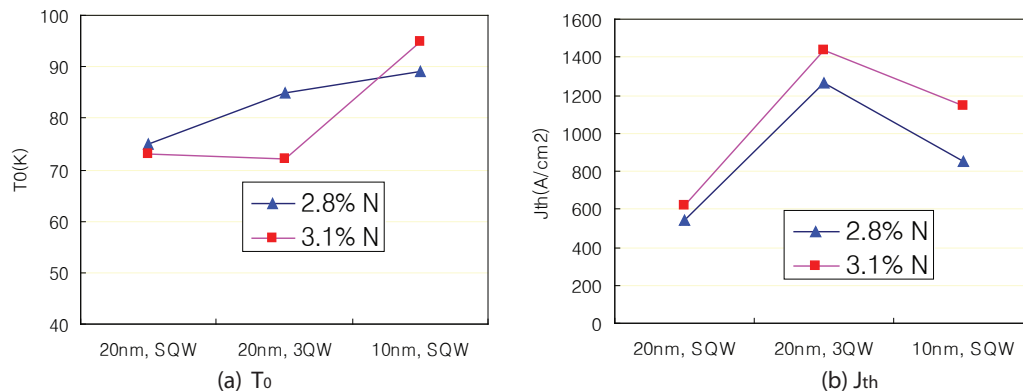


Figure 4.14: T_0 and J_{th} for all 6 sets of lasers.

with segmented contacts (i.e., the contact metal is a collection of equal-length segments, rather than one long metal line). The total amplified spontaneous emission (ASE) spectrum is measured as a function of the pumped stripe length, from which such parameters as spontaneous emission spectrum, internal loss and optical gain spectrum can be calculated. The most interesting parameter to be extracted from this measurement is the spontaneous emission current in real units, which is possible with proper calibration. With this information, non-radiative recombination current can be determined unambiguously. The details of the measurement can be found in [138, 139].

The most important results from the segmented contact measurements are shown in Fig.4.15 and Fig.4.16. In order to understand these two graphs, their x-axis parameter needs explanation, which is shown in Fig.4.17. The transparency point (TP) is the photon energy at which the optical gain is 0 at a given driving current. The absorption edge (AE) is the photon energy at which the net modal loss is $25cm^{-1}$ for a SQW and $75cm^{-1}$ for a 3QW (i.e., about half of the maximum modal loss for an unpumped QW). The separation between the TP and the AE is a measure of how hard the QW is driven. Two different QW samples with the same TP–AE difference can be considered to be being driven to the same separation of quasi-Fermi levels and therefore the same carrier density per QW.

Fig.4.15 shows the nonradiative current per QW, for all 6 different QW structures.

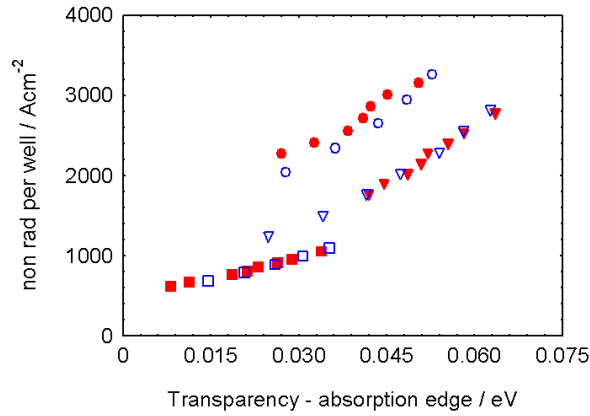


Figure 4.15: Non-radiative current divided by the number of wells. Closed red symbols 3.3%N, open blue symbols 3%N. Circles are thin barrier SQW, Triangles are thick barrier SQW and squares are 3QW

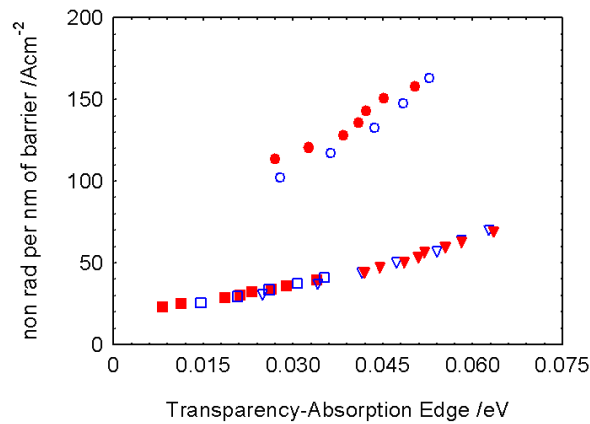


Figure 4.16: Non radiative current divided by total barrier width. Closed red symbols 3.3%N, open blue symbols 3%N. Circles are thin barrier SQW, Triangles are thick barrier SQW and Squares are 3QW

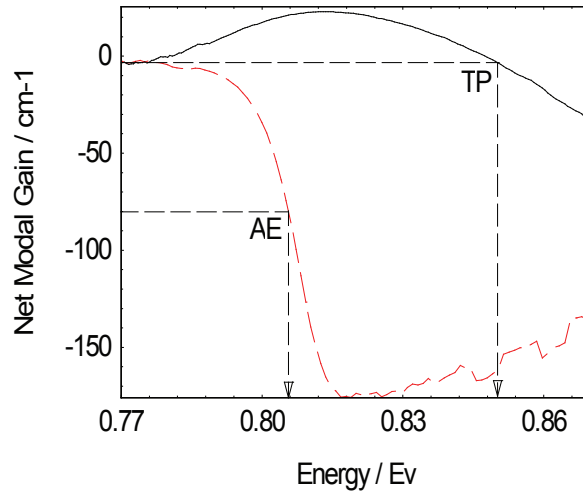


Figure 4.17: Definition of the absorption edge and transparency point extracted from the modal gain and loss spectra

The standard SQW (with 20nm GaNAs barrier), thin-barrier SQW, and 3QW lasers all have different nonradiative current per QW, which suggests that Auger recombination or defect recombination is probably not the dominant mechanism, because the non-radiative recombination current per QW would be independent of barrier thickness or number of QWs if defect or Auger recombination were dominant.

On the other hand, Fig.4.16 shows nonradiative current per nm of GaNAs barrier material. It is to be noted that the standard (thick-barrier) SQW, the thin-barrier SQW, and the 3QW have a total of 40nm, 20nm, and 80nm of GaNAs barrier material, respectively. In this figure, it is very interesting that the thick-barrier SQW and the 3QW lasers lie on the same line, indicating that for these two structures the non-radiative recombination is the same for the same thickness of GaNAs material, which in turn implies that the leakage into and non-radiative recombination in the GaNAs barriers is the most dominant non-radiative carrier loss mechanism.

It is interesting to note that in both Fig. 4.15 and Fig. 4.16, the thin-barrier SQW lies significantly higher in the graph, indicating disproportionately higher non-radiative current. It is well known that 20-nm GaNAs barriers result in much better QW quality than GaAs barriers due to strain compensation, and it is suspected that

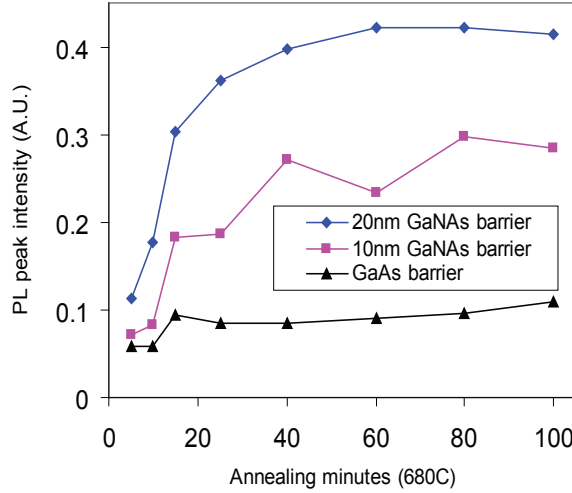


Figure 4.18: PL intensity of GaInNAsSb QW for 20nm, 10nm, and 0 GaNAs barrier thicknesses

10-nm GaNAs layers do not provide enough strain compensation, resulting in poorer material quality (i.e., more defects) in the QW. This hypothesis is corroborated in Fig.4.18, where PL intensity degrades as the thickness of GaNAs barriers is reduced.

Another interesting point is that the comparison between higher-nitrogen and lower-nitrogen samples does not show much difference in Fig.4.15 and Fig.4.16, which refutes the previously highly-held conception that more nitrogen leads to more defects in the QW and degraded laser performance. In this experiment, non-radiative recombination for a given TP–AE difference is the same, even for increased nitrogen content, indicating the same QW quality. On the other hand, higher-nitrogen QWs are found to have higher internal loss (12 vs. 6 cm^{-1} for thin-barrier SQW, and 18 vs. 14 cm^{-1} for 3QW [140]), leading to higher threshold current.

Now that leakage current appears to be the dominant carrier loss mechanism in the active layer of the GaInNAsSb/GaNAs QW lasers, further improvement of laser performance, including both T_0 and J_{th} , should come from a reduction of this carrier leakage component. As this leakage current results from the combination of low band offset and poor barrier material quality, it can be tackled by either improving the barrier material quality or increasing the band offset.

The quality of GaNAs barrier material was investigated by PL measurements of GaNAs/GaAs QWs [92] and was found to be rather insensitive to growth conditions. It is thus not clear whether the GaNAs quality has the potential for significant improvement. On the other hand, the addition of small amount of Sb to the GaNAs layer was found to improve the quality significantly, while addition of large amount of Sb degraded the material quality [92, 141]. This observation can be used to improve the barrier material quality by using GaNAsSb layer with the proper Sb composition. Unfortunately, in our system with a non-valved Sb cracker, it is not possible to change the Sb flux fast enough between the GaNAsSb barrier and the GaInNAsSb QW to adequately control the Sb composition. Thus, our growth process incorporates too much Sb in the GaNAsSb layer when the proper amount of Sb is incorporated in the GaInNAsSb QW. A valved Sb cracker or an additional Ga cell needs to be installed on the MBE chamber in order to obtain higher quality GaNAsSb barriers.

Increasing the barrier height appears to be a more feasible solution with the current configuration of our MBE chamber, as a phosphorous cell is already installed, which enables growth of GaAsP layers. GaAsP is tensily strained on GaAs and has a higher bandgap than GaAs, so it satisfies both requirements of high barrier height and strain compensation at the same time. This is a very promising opportunity for improving GaInNAsSb lasers, but growth of GaAsP barrier layers also has its challenges, especially with the unvalved GaP source we currently have. A significant amount of phosphorous goes around the shutter even when it is closed, so a significant amount of phosphorous incorporates into the GaInNAsSb layer, increasing its bandgap and possibly affecting its quality. The larger bandgap of GaAsP can also affect the carrier capture efficiency into the QW. This will affect the PL samples and lasers, reducing the observed PL intensity and/or the modulation speed of lasers. Despite these challenges, growth of high quality GaInNAsSb/GaAsP QWs is being attempted at the time of writing, which, if successful, can help realize low-threshold and high- T_0 lasers at $1.55\mu\text{m}$ on GaAs substrates.

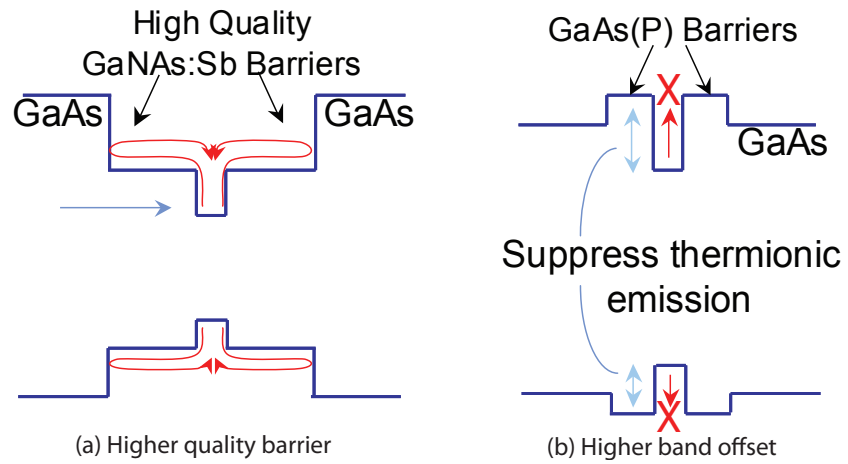


Figure 4.19: Two approaches to reduce leakage problem.

Chapter 5

1528nm VCSEL

Realization of vertical-cavity surface-emitting lasers (VCSELs) for communications wavelengths of 1.3–1.6 μm has been a very important motivation for the substantial research efforts for GaInNAs(Sb) material. The advantages of VCSELs compared to edge-emitting lasers include lower threshold current, better coupling with optical fibers, better temperature stability of emission wavelength, much easier testing, and the possibility of making 1-D or 2-D arrays for high-density interconnects.

However, VCSELs have not been available for some important wavelengths, especially the wavelengths appropriate for fiber communications. Like conventional edge-emitting lasers, VCSELs are composed of an active region and a pair of mirrors around the active region. Unlike the edge emitting lasers for which simple cleaved facets with or without dielectric coating are sufficient as the mirrors, much more complex distributed Bragg reflectors (DBRs) are necessary for the mirrors for a VCSEL. These are necessary because of the requirement to achieve very high reflectivity over 99%, and a vertical configuration for the cavity. DBRs require high quality deposition of many alternating layers of different refractive indices and GaAs provides the best substrate for making such DBRs, thanks to the availability of the AlGaAs alloy system which provides good index contrast, good electrical/thermal conductivities, and close lattice match to GaAs.

The challenge has been that emission in 1.3–1.6 μm wavelength range was not available from III-V alloys lattice-matched to GaAs substrates, until the discovery

of GaInNAs(Sb) [15, 17]. On the other hand, InGaAsP, which is lattice-matched to InP substrates, is able to emit in the 1.3–1.6 μm wavelength range, but it has lacked a simple, reliable, and commercially viable DBR material technology despite many efforts and some laboratory successes [142, 143].

GaInNAsSb material enables VCSELs in the communications wavelength range by providing the long-awaited optical gain. VCSELs around 1.3 μm wavelength were realized [67, 144] using GaInNAs QWs not long after the first reports of dilute nitrides [15, 16]. Since then, low threshold current (1–2mA), low threshold voltage (<2V), high output power (0.8mW or higher) [44–46], and 10Gbps direct modulation [47, 145, 146] have been reported.

On the other hand, GaInNAs(Sb) VCSELs over 1.5 μm wavelength have been very slow to be realized. The biggest hurdle has been the difficulty of achieving high-quality QWs for longer wavelengths, as more indium and nitrogen must be incorporated. This problem was greatly alleviated by the addition of antimony [91, 147], but it still took significant time and effort to improve the QW quality and achieve low-threshold edge-emitting lasers [96, 122, 148], the first VCSELs at 1.46 μm VCSEL [53] and then at 1.53 μm [54]. Despite significant efforts, these VCSELs have not achieved continuous wave (CW) operation at room temperature.

In addition to the QW quality problem, low loss DBRs also posed significant challenges for 1.5 μm or longer-wavelength VCSELs, because the index contrast between GaAs and AlGaAs layers is smaller and the free carrier absorption is larger for longer wavelengths. There also have been practical issues with our MBE system, such as the difficulty of thickness control due to flux fluctuation from the effusion cells and the random quality problems either due to the "mystery" pressure burps in the chamber and the instability of the plasma cell.

We were able to achieve CW operation near room-temperature and pulsed operation at room temperature for a 1528nm GaInNAsSb VCSEL by combining improvements in the MBE chamber, growth and annealing conditions that have been researched over many generations of graduate students and careful design and control of the thicknesses and doping of the epitaxial layers. The current VCSEL design, growth, fabrication, and results are described in the following sections.

5.1 Structure and design

The gain and loss in a VCSEL should satisfy the following equation for lasing to occur [149]:

$$\Gamma_z g_{th} = \Gamma_z \alpha_{ac} + (1 - \Gamma_z) \alpha_{SCH} + \frac{1}{2L} \ln \frac{1}{R_1 R_2} \quad (5.1)$$

where L is the length of the cavity, Γ_z is the longitudinal (i.e., vertical for a VCSEL) confinement factor, and α_{ac} and α_{SCH} are internal losses from the active region and the SCH region, respectively. According to [149], $\Gamma_z = \Gamma_r d/L$, where d is the thickness of the active layer and Γ_r is a relative confinement factor, which asymptotes to 2 when d is much smaller than L . Assuming $\Gamma_r = 2$ for simplicity as we are dealing with QW active layers, the equation can be rewritten by multiplying both sides by $2L$ to get an equation of gain and loss per round trip.

$$4dg_{th} = 4d\alpha_{ac} + 2(L - 2d)\alpha_{SCH} + \ln \frac{1}{R_1 R_2} \quad (5.2)$$

Assuming very high reflectivities for both mirrors, $\ln(1/R)$ can be approximated by $(1-R)$, so we have

$$4dg_{th} = 4d\alpha_{ac} + 2(L - 2d)\alpha_{SCH} + (1 - R_1) + (1 - R_2) \quad (5.3)$$

The material gain at threshold g_{th} follows the equation

$$g_{th} = g_0 \ln\left(\frac{\eta J}{J_{tr}}\right) \quad (5.4)$$

with g_0 around 1000 per cm and J_{tr}/η around $600A/cm^2$ measured by the segmented contact method [140] for the standard SQW lasers described in the previous chapter. Using this data and assuming a linear increase in gain and current density with increased number of QWs, the round-trip gain ($4dg_{th}$) is calculated and shown in Fig.5.1.

A SQW would be the best choice if we can guarantee very low round-trip loss, but more QWs would be a safer choice considering the challenges facing the design and

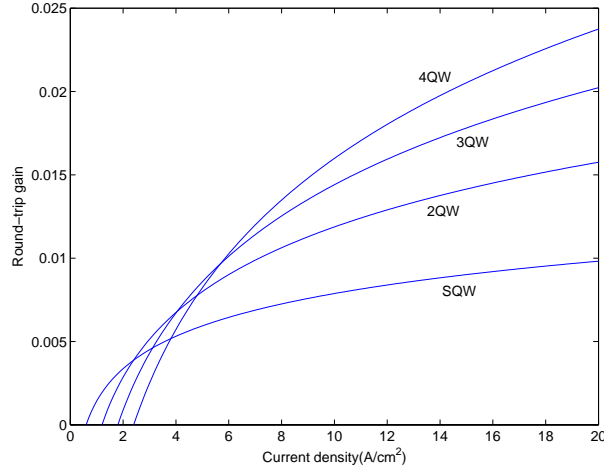


Figure 5.1: Round-trip gain for different number of QWs

growth of the DBR mirrors. On the other hand, too many QWs can be challenging to grow and may also break the assumption of $\Gamma_r = 2$ as the total active region thickness increases. We chose 3 QWs as a trade-off.

An upper-bound for α_{ac} can be found from the measurements of SQW edge-emitting lasers, where α_i is found to be around 5cm^{-1} [140]. This α_i contains losses from both the active layer and the cladding, but if we assume all the loss is from the active layer with confinement factor of 1.4% [55], α_{ac} can be estimated at 360cm^{-1} and $4d\alpha_{ac}$ is about 0.003, or 0.3%.

α_{SCH} can be assumed negligible as the SCH layer is undoped and the carrier density there would be quite small, even under strong forward bias thanks to the large bandgap offset of GaAs from the GaInNAsSb QW.

Although not explicitly shown in the equations above, there is also diffraction (or, scattering) loss due to the dielectric aperture when the aperture is defined by air or oxide, or due to lack of index guiding when the aperture is defined by proton implant. We chose to use oxide apertures defined by wet-oxidation of high-Al AlGaAs layer [150,151], as it has the advantage of providing both optical and electrical confinement at the same time. An analytical model for scattering loss due to dielectric apertures is provided in [152], according to which we get an effective cavity length $L_c = 2\mu\text{m}$

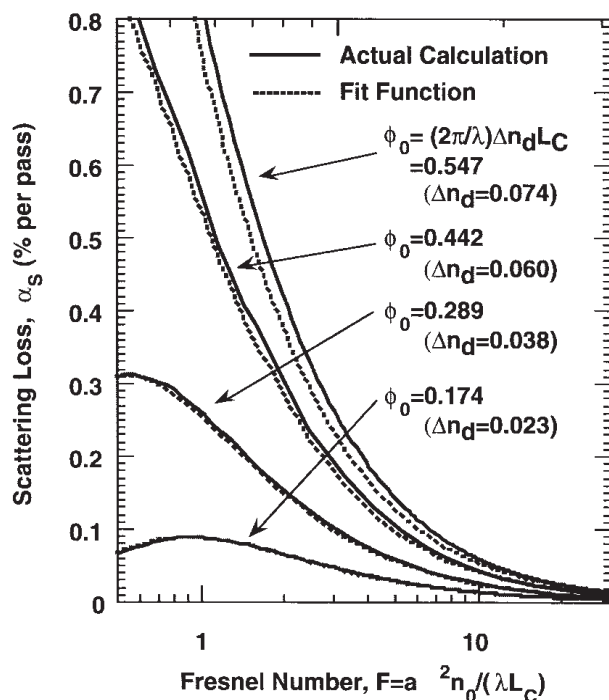


Figure 5.2: Results of the single-pass estimate for scattering loss for laterally abrupt aperture [152]. The graph should be read based on two numbers, ϕ_0 and F . 'a' means aperture radius.

and effective index step size $\Delta n_d = 0.07$, for a single-lambda cavity for $\lambda = 1.55\mu\text{m}$. Then, for an aperture radius of $1\mu\text{m}$ the diffraction loss could be quite high ($\sim 2\%$ per round-trip), but for a radius of $2\mu\text{m}$, it decreases to about 0.4% per round-trip. ($\phi_0 = 0.56$, and $F \sim 1$ for $a = 1\mu\text{m}$ and $F \sim 4$ for $a = 2\mu\text{m}$, to be looked up in Fig. 5.2)

Comparing the gain as shown in Fig.5.1 with the calculated loss components, we decided that we need to limit the round-trip mirror loss to less than 0.5% , as we wanted to keep the threshold current density below $10\text{kA}/\text{cm}^2$ to minimize heating for CW operation (thus limiting the round-trip gain below 1.5%) and have some margin for unexpected losses that arise from ignored factors in the theoretical calculations or from variations during growth or fabrication.

Although the GaAs/AlAs-based DBR technology is very well established for shorter-wavelength VCSELs on GaAs and its manufacturability and reliability are one of the

key motivations for GaInNAs(Sb) VCSEL research for 1.3 or 1.55 μm wavelength range, different optical properties of the DBR materials present additional challenges for long wavelength VCSELs. The contrast between the two materials becomes smaller for longer wavelengths, necessitating more mirror pairs to provide a given reflectivity. Another serious challenge is that the free carrier absorption and inter-valence-band absorption (IVBA) increase for longer wavelength, increasing mirror loss, especially for the p-doped DBR mirror¹. Lower doping has to be used to limit the optical loss, but then the electrical resistance increases (again, more severe for the p-doped mirror due to lower mobility), which leads to unnecessary device heating and degradation of laser performance. Longer wavelength also means that each mirror pair has to be thicker, which exacerbates all these optical, electrical and thermal problems. These problems have indeed made the realization of 1550nm VCSELs quite challenging, especially when combined with the growth challenges for GaInNAs(Sb) QWs for 1.55 μm emission.

It is possible to circumvent the challenges for DBR design at 1.55 μm by using alternative structures, such as intra-cavity contacts or a tunnel-junction, instead of the simplest structure with one n-DBR and one p-DBR illustrated in Fig. 5.3 as a conventional 'PIN' structure. The intra-cavity contact structure uses undoped layers for one or both of the DBR mirrors and currents are injected through highly-doped injection layers with electrical contacts placed between the active layer and the DBR(s) [47, 48, 145, 146, 154]. The design of DBR mirrors becomes significantly simpler, especially for the p-DBR, but it requires additional care and optimizations for the best tradeoff between uniform current injection vs. lower optical loss. A tunnel junction provides a conversion between n-type and p-type carriers with low additional resistance, allowing us to use two n-DBRs instead of one n-DBR and one p-DBR [42, 43, 155]. Without a high-optical-loss high-resistance p-DBR, it becomes much easier to design the DBR mirrors. But this structure also requires significant efforts to achieve high-quality growth with high doping confined to the thin tunnel

¹According to the experimental results in [153], the absorption coefficient for 10^{18}cm^{-3} p-type GaAs is 13cm^{-1} at 1.3 μm and 26cm^{-1} at 1.6 μm . Very similar numbers are observed for InP and $\text{In}_{.4}\text{Ga}_{.6}\text{As}$ [153]. On the other hand, the absorption coefficient is about 5cm^{-1} for n-type GaAs at 1.55 μm .

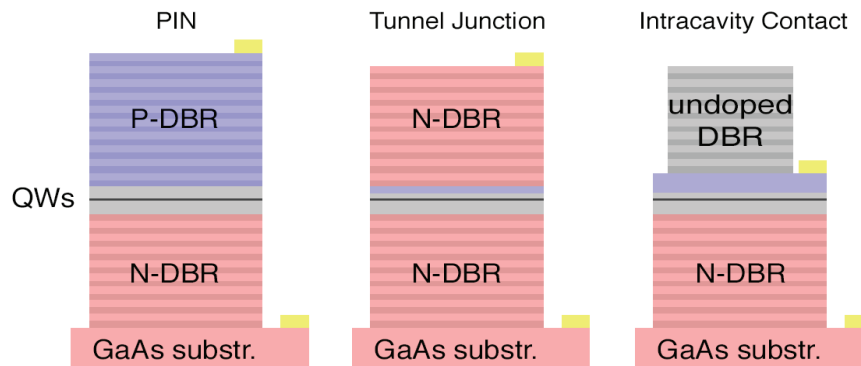


Figure 5.3: Conventional PIN, intra-cavity, and tunnel-junction VCSEL structures

junction and to test and optimize the electrical resistance.

Despite the challenges, we chose the simplest conventional structure composed of a p-DBR, an undoped cavity, and an n-DBR because of its simplicity for growth and fabrication, thus not having to worry about too many new factors at the same time for our attempt to achieve the first room-temperature CW $1.55\mu\text{m}$ VCSEL.

For this conventional PIN structure, the p-DBR poses the biggest challenge, due to larger absorption and lower mobility for p-doped layers than n-doped layers. The hetero-junction barrier between high-index and low-index layers is another important factor that increases electrical resistance significantly, degrading the carrier movement over or through the barrier exponentially with respect to the barrier height and thickness. This problem can be solved by using linear or parabolic composition grading with delta- or step-doping profiles at GaAs/AlAs interfaces, as discussed in [156–159]. This can be done relatively easily in OMVPE (Organo-Metallic Vapor-Phase Epitaxy) thanks to its capability of smooth compositional grading, but is not so easy in MBE because only a small set of discrete compositions are available for a given growth run, as the composition is controlled by opening/closing of the shutters in front of a limited number of effusion cells, for which it is very hard to change the temperatures reliably on the fly. It is possible to emulate the linear or parabolic grading using a process called ‘digital alloying’, whereby continuous grading is approximated by fast switching between two different compositions while slowly varying the duty

cycle. But this process requires a very large number of shutter operations, requiring hundreds or even over thousand shutter operations per DBR growth, which presents a significant reliability issue for the MBE machine. Especially problematic are the Ga shutters, which can get stuck to the chamber wall because of wetting by the Ga melt on them and then be bent out of shape when the shutter actuator tries to open/close it forcefully. Use of externally-adjustable shutters greatly reduced the repair time and the associated pain and risks of this shutter problem, but such a shutter problem during a VCSEL growth is still very costly to recover from, setting us back by a few days at best and a month or more in the worst case.

Therefore, we instead used step-wise composition grading for DBR interfaces to limit the number of shutter operations, while still trying to minimize the electrical resistance with minimum doping. The high-index layer is GaAs and the low-index layer is 91% AlGaAs. There are 2 Ga cells and 2 Al cells in our System4 MBE chamber used for DBR growth. To obtain the finest step-grading with minimum number of shutter operations, we set the growth rates of Al1, Al2, Ga1, and Ga2 cells at 0.47, 0.23, 0.64, and 0.07 $\mu\text{m}/\text{hr}$ respectively, and by following the sequence shown in Table 5.1, we get a 6-step grading in composition going from a GaAs to an $\text{Al}_{0.91}\text{Ga}_{0.09}\text{As}$ layer, over 30nm. Doping is higher in the graded interface (especially at the optical nodes) than in the GaAs or $\text{Al}_{0.91}\text{Ga}_{0.09}\text{As}$ layers, because the thermionic injection and tunneling processes occurring in the graded interfaces have a much steeper dependence on doping than the drift process occurring in a GaAs or $\text{Al}_{0.91}\text{Ga}_{0.09}\text{As}$ layer. The base doping level for the 91% AlGaAs layers was slowly increased from $3 * 10^{17}\text{cm}^{-3}$ for the innermost layers (i.e., closest to the cavity) to $2 * 10^{18}\text{cm}^{-3}$ for the outermost layers. Be was used to provide the slowly-varying low background p-doping for all the layers, while C was added to increase doping in the graded regions². On the other hand, much steeper 3-step grading over 5nm is chosen for the n-DBR (using only layer #0, 1, 4, and 6 from Table 5.1), as the resistance problem is much less severe for the n-DBR due to the higher mobility and the smaller effective mass for electrons than holes.

²The Be effusion cell is harder to control quickly than the CBr_4 source, and Be diffuses more readily than C at high concentrations and while the wafer is heated up, i.e., during growth or annealing.

Layer index	Al1	Al2	Ga1	Ga2	Al composition(x in $\text{Al}_x\text{Ga}_{1-x}\text{As}$)
0	c	c	o	o	0
1	c	o	o	o	0.25
2	o	c	o	o	0.40
3	o	o	o	o	0.50
4	c	o	c	o	0.77
5	o	c	c	o	0.87
6	o	o	c	o	0.91

Table 5.1: Shutter operations (o/c for open/closed) and composition grading. Special care was taken to reduce number of shutter operations, especially for the Ga shutters, which are more vulnerable.

We calculated the reflection, absorption, and transmission of the DBR mirrors using a multi-layer 1-D transmission matrix solver, while changing the number of layers until a proper level of reflectivity is attained. We first considered growing on a p-type substrate, thus placing the p-DBR at the bottom and the n-DBR at the top to help minimize the resistance of the p-DBR (the bottom DBR has a wider effective area, as the top DBR is etched down to form a cylindrical mesa, while the bottom DBR is not etched). But it was not possible to achieve less than 0.4% mirror loss (= absorption + transmission) for the p-DBR due to the wide 30-nm grading and the high IVBA, without reducing the doping level too much. Since there must be some transmission loss in the upper DBR to guarantee that the external efficiency does not suffer too much, we suspected that the total mirror loss might be too high with this structure. On the other hand, if we grow on an n-substrate, the bottom n-DBR can attain reflectivity over 99.97% (due to narrower grading region and lower absorption loss) and the upper p-DBR can attain 99.6% reflectivity. The bottom n-DBR has 35 layers, and the top p-DBR has 23 layers in our current design.

The first (closest to the cavity) $\text{Al}_{.91}\text{Ga}_{.09}\text{As}$ layer in the p-DBR also serves as the oxide aperture. The uppermost 40nm of this layer is $\text{Al}_{.98}\text{Ga}_{.02}\text{As}$, obtained by alternating $\text{Al}_{.91}\text{Ga}_{.09}\text{As}$ and AlAs layers 10 times (digital alloying). Because the oxidation rate is exponentially faster for higher Al content [160], the thin 98% AlGaAs layer oxidizes laterally first, and then the 92% AlGaAs layer oxidizes slowly

Chamber Name	Sources							
System4	Al1	Al2	Ga1	Ga2	As	C	Be	Si
System5	Ga	In	N	P	As	Sb	Be	Si

Table 5.2: Current cell configurations for the two MBE chambers used for this thesis work

downward. This results in a tapered profile of the oxide, with the aperture being the narrowest at the optical node [161], which helps to minimize the scattering loss.

5.2 Growth and fabrication

The VCSELs were grown in 3 steps in the two coupled MBE chambers. First, the bottom n-DBR is grown in System4, which is the DBR machine with 2 Al and 2 Ga cells, and Si(n-type), Be(p-type) and CBr₄(p-type) cells for doping. Second, the cavity, including 3QW, is grown in System5, which is the nitride machine with the N rf plasma cell. Finally, the top p-DBR is grown in System4. The current cell configurations for the two MBE chambers are shown in Table 5.2. Note that each chamber can have only up to 8 cells.

An apparently mundane, but very important challenge for the growth of VCSELs is the control of growth thickness. Just 1% error in the growth thickness of the DBRs or the cavity results in cavity/mirror wavelength error of 15nm, which can cause significant mismatch with the gain spectrum of the GaInNAsSb QWs, resulting in higher threshold or no lasing at all. To assure correct thicknesses, several growth calibrations were made immediately before VCSEL growth, with the sources at their final temperatures. The source temperatures are determined to get the desired growth rate, based on the previous calibration growths and the fluxes measured with the ion gauge. For each of the aluminum sources in System4, a 1000nm AlAs layer was grown on GaAs for calibration. Normal-incidence, white-light reflectivity spectrum of the wafer was taken and matched to simulation using the thin-film solver(mff), to get the actual AlAs growth thickness. Another 1000nm of GaAs is grown on top of the AlAs layer, and reflectivity measurements and simulations are repeated to calibrate

the GaAs growth rate.

Despite the growth rate calibration, the cells were found to be drifting with time. This growth rate fluctuation was more common when older trumpet-shaped crucibles were used, compared to newer SUMO cells from Veeco, which have a constriction at the neck that better isolates the cell from the surrounding MBE chamber. They also have a dual-zone heating system, with one heater at the tip and the other at the base of the crucible. The gallium cell stability was greatly improved by keeping the tip 150-180°C hotter than the base [56], and this improved stability was a critical factor in realizing previous 1.5 μ m-range GaInNAsSb VCSELs [53, 54]. On the other hand, the 150-180°C temperature offset resulted in too many oval defects on the wafer³, so we chose larger difference (210-240°C) for the growth of the VCSELs in this thesis. This reduced the oval defect density, but degraded the cell stability.

Moreover, the dual-zone heating can not be applied to the aluminum cells, because aluminum has an unfortunate property of creeping up the crucible wall (made of PBN, or pyrolytic boron nitride) and overflowing, which can short out the heater filament and destroy the cell permanently. The aluminum cells therefore are heated by a single heater at the base only. We found the flux instability of the aluminum cells quite significant, changing as much as 5% after a bottom DBR growth, which took as long as 14 hours. Because of the long growth time and the larger tip-base temperature difference, the stability of the gallium cells was not strikingly better than the aluminum cells, routinely showing 1–2% variation after each growth.

If two growths are done back-to-back without any adjustment in between, the cell may deviate in the opposite direction during the second growth cancelling out the deviation during the first growth, but it may also continue drifting in the same direction, resulting in 2–4% total deviation. The flux deviation after each growth tends to be one-way (i.e., downward) when there is little material left in the cell, but the deviation was more random when there is enough material in the cell, probably as the surface area of the melt sprawls and shrinks randomly over time. For other growths such as edge-emitting lasers, a few percent of flux variation is not so critical,

³Gallium condenses on the tip if the tip is not hot enough. When the condensed droplets fall into the gallium melt, small gallium droplets are spit onto the wafer [162]. Larger temperature difference between the tip and the base reduces the condensation and the oval defects.

but it is extremely critical for VCSELs. we thus chose to re-measure the growth rates of the cells before the growth of each region(i.e., bottom DBR, active region, and top DBR), so that we can adjust the cell temperatures in order to start the next growth with correct fluxes. However, we did not go as far as repeating 'calibration growths' between DBR growths, because one calibration run takes too long (2 days). Instead, we depended on the fluxes measured by the ion gague to estimate the actual growth rate at the moment, which turned out to be very accurate within 0.5%⁴.

Despite these efforts, the reflectivity spectrum of the DBRs and the cavity resonance wavelength showed some deviation (up to 1%) from design, because we were not able to monitor and control the growth rate on the fly⁵. To compensate for these deviations, we grew the GaAs SCH region above the active region intentionally thinner by 15nm than designed, so that compensation is possible even when the cavity is thicker than designed and some thickness has to be removed from upper layers. After cavity growth in System5 and before p-DBR growth in System4, the reflectivity spectrum is measured, and compared with simulation. Because the air/GaAs interface provides enough reflectivity, the cavity resonance can be easily observed. When there is any deviation between the measured cavity resonance and the expected resonance, the error in the thickness of the cavity can be estimated and compensated for by adding/removing an appropriate thickness from the first GaAs part of the upper p-DBR growth.

To further ensure against any unexpected problems during growth, including wavelength errors, we grew two VCSELs with two different resonance wavelengths, 1540nm and 1560nm. Each of them showed 15-25nm wavelength error (shorter than designed) right after the bottom DBR growth, so we decided to revise their resonance wavelengths to 1525nm and 1550nm, respectively, to ensure the bottom DBR reflectivity spectrum is not too far off from the resonance. After cavity and upper DBR growths using the corrections described above, each showed a cavity resonance at 1532nm and

⁴The reflectivity measurement and simulation used for the calibration growth can not provide better than 0.5% accuracy, either.

⁵We considered using RHEED oscillations or reflectivity measurement for in-situ growth rate monitoring, but both methods suffer too much from wafer wobble, the same problem that plagued the emissivity-compensated pyrometry (See Section 3.1.2).

1553nm, respectively, at the center of wafer. This is up to 0.5% deviation either from the original wavelength targets or from the revised targets.

One unfortunate problem that occurred during growth was that the CBr_4 source that provides the carbon doping for the p-DBR did not control the CBr_4 properly, doping the inner-most DBR layers at several 10^{18}cm^{-3} 's, which was 5-10 times higher than intended. We did not notice this problem until we had already grown a few p-DBR layers for the second VCSEL, which was too late to correct the problem. Without this problem, we expect the VCSELs would have shown better performance, such as lower threshold or higher output power, than reported here.

After growth of the VCSELs, they were annealed in an RTA for 7 minutes at 670°C , which was determined by finding the optimal annealing condition for a PL sample that was grown on the same day and treated with the same self-annealing in the MBE chamber as the VCSEL wafers. Ring-shaped Ti/Pt/Au contacts were first defined by lift-off method. Cylinder-shaped mesas ranging in diameter from 18 to $36\mu\text{m}$ were defined by lithography and DRIE etching down to the top of the bottom DBR. Wet oxidation of the oxide aperture was carried out in the GaAs oxidation furnace filled with N_2 gas saturated with water. Fabrication is completed with the deposition of Au/Ge/Ni/Au contact layer on the wafer backside, and the wafer is annealed at 420°C for 1 minute for Au/Ge/Ni/Au contact alloying.

5.3 Measurements

The VCSELs were mounted epi-side up on a copper chuck for testing. Below the copper chuck was a thermoelectric cooler (TEC), feedback-controlled to maintain a constant temperature. The n-side electrical connection is made through the copper chuck and the bottom n-contact of the VCSEL wafer, and the p-side electrical connection is made by placing a probe tip on top of a top ring contact. Optical output power is measured using an integrating sphere and a Thorlabs PDA400 amplified photodetector, and the emission spectrum is measured by coupling the light output into a $62.5\mu\text{m}$ multimode fiber through collimating lenses. The whole measurement

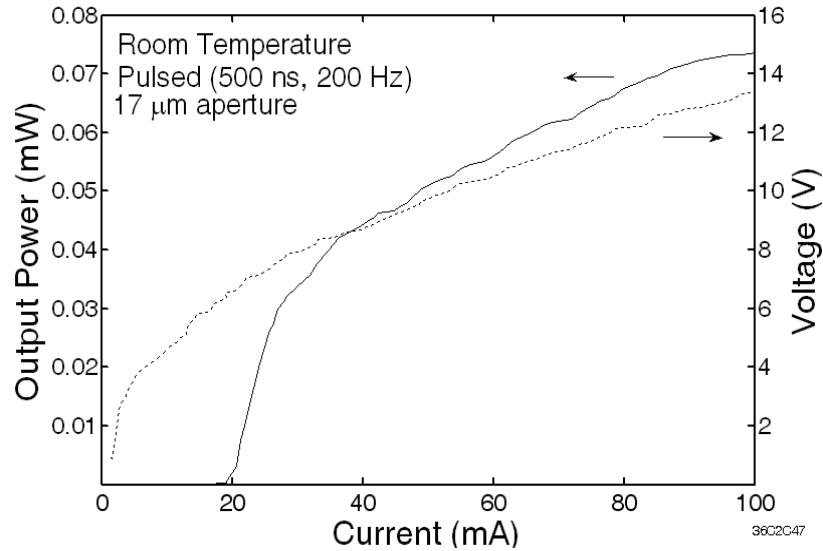


Figure 5.4: Pulsed LI curve for $17\mu\text{m}$ diameter aperture.

setup was wrapped in a plastic bag, which was purged with dry air to avoid moisture condensation on the devices when low temperatures below the due point were necessary.

We observed room-temperature pulsed-mode operation at 1528nm for a $17\mu\text{m}$ -diameter aperture VCSEL, as shown in Fig.5.4 and Fig.5.5. The threshold current is 20mA , and the bias voltage is about 6V at threshold. To the best of our knowledge, this is the first room-temperature 1528nm VCSEL monolithically grown on a GaAs substrate. Previous VCSEL reports from our group achieved the first monolithic GaAs-based VCSELs at 1460nm [53] and at 1534nm [54], which were all important milestones, but they all lased in pulsed mode only when cooled below -15°C , with significantly higher threshold current ($>60\text{mA}$) and higher voltage at the threshold (about 20V) [53].

We also observed near-room-temperature CW operation for a $7\mu\text{m}$ -diameter aperture VCSEL, as shown in Fig.5.6. The threshold current is very low at 3mA , and CW operation persists up to 15°C . We failed to measure a CW spectrum because the

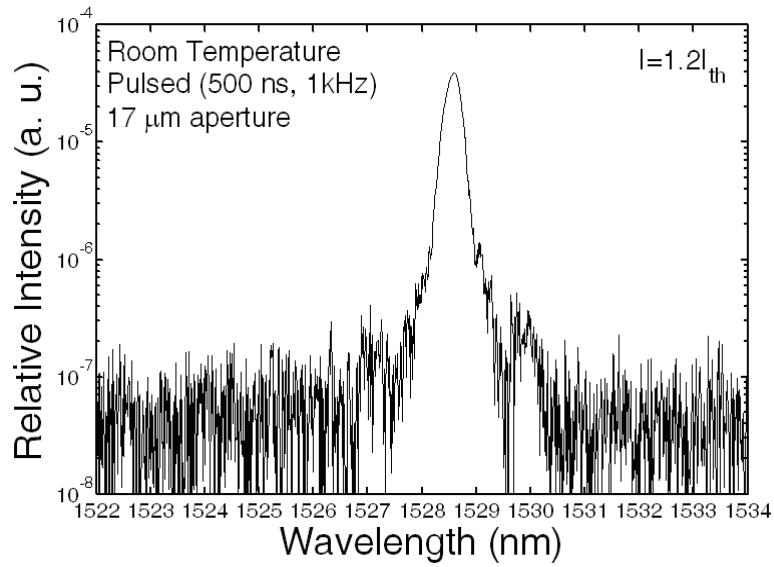


Figure 5.5: Spectrum of a pulsed 1528nm VCSEL at $1.2\times$ threshold.

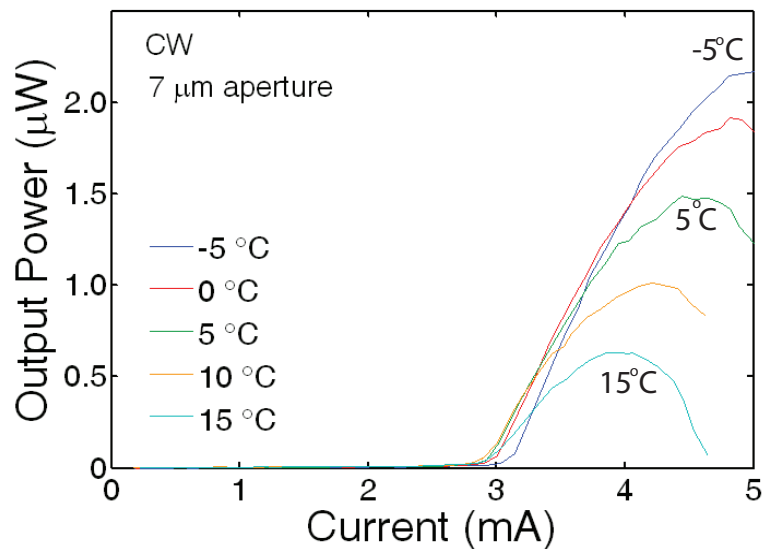


Figure 5.6: CW LI curve of a 7 μm -aperture VCSEL

probe tip was very unstable on the small top contact, slipping away at a small vibration of the testing setup. For future generations of VCSELs, it would be beneficial to apply planarization and provide a larger probe-landing area for the top contact, for easier testing as well as better heat-sinking.

This is the first-ever CW VCSEL on GaAs to the best of our knowledge, which is a very important milestone, even though the CW output power ($3\mu\text{W}$) is quite low. Part of the reason is believed to be the CBr_4 control problem that occurred during the p-DBR growth, resulting in much higher doping than intended. As this caused higher optical loss in the mirror, the external quantum efficiency is quite poor as more optical power is lost by absorption in the DBR mirror rather than emitted through the top mirror. (The slope efficiency shown in Fig.5.6 is quite low, 1.4mW/A.)

Another problem is that the voltage drop across the DBRs is still quite high. 6V bias voltage at threshold is much higher than the bandgap of the GaInNAsSb material, which means that about 5V is dropped across the DBRs, mainly the higher resistance p-DBR. Unintended higher doping due to the CBr_4 source problem might have slightly alleviated this resistance problem, but it is still clear that the 6-step grading used in our MBE growth is very far from being optimal, as abrupt hetero-barriers are still present severely limiting carrier transport. One possible way to solve this problem is to combine the strengths of OMVPE and MBE, by growing the DBRs (especially the p-DBR) in OMVPE for its superior ability of smooth grading and growing the GaInNAsSb QWs in MBE for its superior growth quality for GaInNAsSb, as has been demonstrated for $1.3\mu\text{m}$ VCSELs [49]. We actually have two p-type GaAs wafers ready with p-DBRs grown in MOVPE, so that we can grow QWs and the n-DBRs on top of them using MBE, to realize low operating voltage. This would be the first thing to try for a future generation of VCSELs.

Another possibility is using newer generations of MBE machines that have vertically instead of horizontally configured cells and have a dozen or more sources, so that smaller-increment multiple-step grading is possible with nearly the same effectiveness as grading in MOVPE, as reported for $1.3\mu\text{m}$ VCSELs [50]. Other possible approaches are intra-cavity contacts [47, 48, 145, 146, 154] and tunnel junctions [42, 43, 155] as illustrated in Fig. 5.3. These techniques have been successfully demonstrated for $1.3\mu\text{m}$

GaInNAs VCSELs, and there is no reason to expect these techniques would not work for 1.55 μm VCSELs. They will be explored for future generations of 1.55 μm VCSELs.

The high temperature sensitivity (i.e., low T_0) of the GaInNAsSb/GaNAs QWs discussed in the previous chapter is another important challenge that is limiting the output power and the temperature range of CW operation. As was discussed in the previous chapter, leakage of carriers into and recombination in the GaNAs barrier layers seem to be the dominant cause of this poor temperature-stability, and adoption of GaPAs barriers instead of GaNAs can alleviate this problem.

In summary, we demonstrated the first room-temperature pulsed operation and the first near-room-temperature CW operation for 1528nm VCSELs grown on GaAs. The output power and the operating temperature range is still inadequate for commercial deployment, but these VCSELs were limited by an one-time unexpected equipment problem and the simplistic PIN structure with sub-optimal step-graded DBRs due to limitations of our MBE chamber. None of these are fundamentally intractable problems. If we solve the high resistance problem of the p-DBR by better grading in the p-DBR layer interfaces, tunnel junctions, or intra-cavity contacts, and improve the temperature sensitivity of the QWs by employing a new barrier material, 1.5-1.55 μm VCSELs operating CW with higher output power and higher operating temperature will be possible and represent significant advance toward providing affordable, high-speed optical networking to every home.

Chapter 6

Conclusion

This thesis presented the efforts of the author and previous students to achieve low-threshold and high temperature-stability edge-emitting lasers, and room-temperature CW VCSELs at $1.55\mu\text{m}$ using GaInNAsSb on GaAs grown by MBE.

Very low threshold ($318\text{A}/\text{cm}^2$ pulsed, and $373\text{A}/\text{cm}^2$ CW) and high-power ($>1\text{W}$ pulsed, 430mW CW) edge-emitting lasers at $1.55\mu\text{m}$ [52], and the first $1.53\mu\text{m}$ VCSELs [54] had been realized through numerous growth optimizations by several generations of students over the years. However, the temperature stability of the edge-emitting lasers remained relatively poor (T_0 in the range of 60K), and the VCSELs worked only in pulsed mode at sub-zero temperatures.

A new annealing condition was found which increased the peak PL intensity after annealing by a factor 2, while also making the process control far easier by opening a very wide optimum-annealing window. A new growth condition (lower As and Sb fluxes) enabled the peak PL intensity to improve by a factor 2. These new annealing and growth conditions were found to combine with each other, resulting in a total improvement in the peak PL intensity by a factor of 4. This improved quality was found to persist through the self-annealing, which the QW experiences for several hours while upper cladding layers or upper DBRs are being grown.

The significantly improved peak PL intensity, however, did not lead to a significant improvement in the laser threshold or temperature stability. Poor temperature stability for 3 different QW structures indicate that the laser threshold current is dominated

by either Auger recombination or leakage current. Segmented contact measurements conducted by J. Ferguson [139] showed that the non-radiative current of the lasers is very closely proportional to the total amount of GaNAs material, which implies that the leakage current is the most dominant mechanism for the threshold current and the poor temperature stability. Either improvement in the barrier material quality or increase in its bandgap is needed to overcome this problem, and GaAsP material is currently being investigated as a candidate to provide large bandgap while also providing strain compensation to the highly compressively-strained GaInNAsSb QW.

The first-ever near-room-temperature CW VCSEL at 1528nm on GaAs is demonstrated, which is a significant milestone toward realizing very low-cost light sources for extending the high-speed optical network all the way to the end users. The CW output power is still low ($3\mu\text{W}$), but this VCSEL was affected by a few non-fundamental problems, such as the one-time unexpected equipment problem and the simplistic PIN structure with sub-optimal step-graded DBRs due to limitations of our MBE chamber. In addition to the efforts to improve the QWs, various approaches will be tried for future generations of VCSELs to reduce the electrical resistance in the p-DBR. As near-room-temperature CW operation is demonstrated with clearly sub-optimal DBR designs and unintended $\times 5$ -10 over-doping in the p-DBR layers, it seems clear that room-temperature CW $1.55\mu\text{m}$ VCSELs is very close to actually contributing to the development of inexpensive fiber communications networks.

Bibliography

- [1] “<http://www.jpix.ad.jp/en/technical/traffic.html>,” 2009.
- [2] S. R. Bank, H. B. Yuen, M. A. Wistey, V. Lordi, H. P. Bae, and J. James S. Harris, “Effects of growth temperature on the structural and optical properties of $1.55\mu\text{m}$ GaInNAsSb quantum wells grown on GaAs,” *Applied Physics Letters*, vol. 87, no. 2, p. 021908, 2005.
- [3] S. G. Spruytte, *MBE Growth of Nitride-Arsenides for Long-wavelength Optoelectronics*. PhD thesis, Stanford University, 2001.
- [4] H. Shimizu, K. Kumada, S. Uchiyana, and A. Kasukawa, “High-performance CW $1.26\text{-}\mu\text{m}$ GaInNAsSb-SQW ridge lasers,” *Selected Topics in Quantum Electronics, IEEE Journal of*, vol. 7, no. 2, pp. 355 – 364, 2001.
- [5] G. Jaschke, R. Averbeck, L. Geelhaar, and H. Riechert, “Low threshold InGaAsN/GaAs lasers beyond 1500 nm,” *Journal of Crystal Growth*, vol. 278, pp. 224–228, May 2005.
- [6] R. Kudrawiec, S. R. Bank, H. B. Yuen, H. Bae, M. A. Wistey, L. L. Goddard, J. S. H. Jr, M. Gladysiewicz, M. Motyka, and J. Misiewicz, “Conduction band offset for $\text{Ga}_{0.62}\text{In}_{0.38}\text{N}_x\text{As}_{0.991-x}\text{Sb}_{0.009}/\text{GaN}_y\text{As}_{1-y}/\text{GaAs}$ systems with the ground state transition at $1.5\text{--}1.65\ \mu\text{m}$,” *Applied Physics Letters*, vol. 90, no. 13, p. 131905, 2007.
- [7] “Surviving the Exaflood,” *Economist*, no. Dec 6-12, pp. 26–28, 2008.

- [8] H. Soda, K. i. Iga, C. Kitahara, and Y. Suematsu, "GaInAsP/InP Surface Emitting Injection Lasers," *Japanese Journal of Applied Physics*, vol. 18, no. 12, pp. 2329 – 2330, 1979.
- [9] V. Jayaraman, J. C. Geske, M. H. MacDougal, F. H. Peters, T. D. Lowes, and T. T. Char, "Uniform threshold current, continuous-wave, singlemode 1300 nm vertical cavity lasers from 0 to 70C," *Electronics Letters*, vol. 34, no. 14, pp. 1405 – 1407, 1998.
- [10] W. Yuen, G. S. Li, R. F. Nabiev, J. Boucart, P. Kner, R. J. Stone, D. Zhang, M. Beaudoin, T. Zheng, C. He, K. Yu, M. Jansen, D. P. Worland, and C. J. Chang-Hasnain, "High-performance 1.6 μm single-epitaxy top-emitting VCSEL," *Electronics Letters*, vol. 36, no. 13, pp. 1121 – 1123, 2000.
- [11] E. Hall, G. Almuneau, J. K. Kim, O. Sjolund, H. Kroemer, and L. A. Coldren, "Electrically-pumped, single-epitaxial VCSELs at 1.55 μm with Sb-based mirrors," *Electronics Letters*, vol. 35, no. 16, pp. 1337 – 1338, 1999.
- [12] S. Uchiyama, N. Yokouchi, and T. Ninomiya, "Continuous-wave operation up to 36C of 1.3- μm GaInAsP-InP vertical-cavity surface-emitting lasers," *Photonics Technology Letters, IEEE*, vol. 9, no. 2, pp. 141 – 142, 1997.
- [13] J. A. Lott, N. N. Ledentsov, V. M. Ustinov, N. A. Maleev, A. E. Zhukov, A. R. Kovsh, M. V. Maximov, B. V. Volovik, Z. I. Alferov, and D. Bimberg, "InAs-InGaAs quantum dot VCSELs on GaAs substrates emitting at 1.3 μm ," *Electronics Letters*, vol. 36, no. 16, pp. 1384 – 1385, 2000.
- [14] O. Blum and J. F. Klem, "Characteristics of GaAsSb single-quantum-well-lasers emitting near 1.3 μm ," *Photonics Technology Letters, IEEE*, vol. 12, no. 7, pp. 771 – 773, 2000.
- [15] M. Weyers, M. Sato, and H. Ando, "Red Shift of Photoluminescence and Absorption in Dilute GaAsN Alloy Layers," *Japanese Journal of Applied Physics*, vol. 31, no. Part 2, No. 7A, pp. L853 – L855, 1992.

- [16] M. Kondow, K. Uomi, K. Hosomi, and T. Mozume, "Gas-Source Molecular Beam Epitaxy of GaN_xAs_{1-x} Using a N Radical as the N Source," *Japanese Journal of Applied Physics*, vol. 33, no. Part 2, No. 8A, pp. L1056 – L1058, 1994.
- [17] M. Kondow, K. Uomi, A. Niwa, T. Kitatani, S. Watahiki, and Y. Yazawa, "GaInNAs: A Novel Material for Long-Wavelength-Range Laser Diodes with Excellent High-Temperature Performance," *Japanese Journal of Applied Physics*, vol. 35, no. Part - 1 - No - 2B, pp. 1273 – 1275, 1996.
- [18] W. Shan, W. Walukiewicz, J. W. Ager, E. E. Haller, J. F. Geisz, D. J. Friedman, J. M. Olson, and S. R. Kurtz, "Band Anticrossing in GaInNAs Alloys," *Physical Review Letters*, vol. 82, no. 6, pp. 1221 – 1224, 1999.
- [19] W. Shan, W. Walukiewicz, J. W. A. III, E. E. Haller, J. F. Geisz, D. J. Friedman, J. M. Olson, and S. R. Kurtz, "Effect of nitrogen on the band structure of GaInNAs alloys," *Journal of Applied Physics*, vol. 86, no. 4, pp. 2349 – 2351, 1999.
- [20] M. Kondow, S. Natatsuka, T. Kitatani, Y. Yazawa, and M. Okai, "Room-temperature continuous-wave operation of GaInNAs/GaAs laser diode," *Electronics Letters*, vol. 32, no. 24, pp. 2244 – 2245, 1996.
- [21] J. O. Neugebauer and C. G. V. de Walle, "Electronic structure and phase stability of $GaAs_{1-x}N_x$ alloys," *Phys. Rev. B*, vol. 51, no. 16, pp. 10568 – 10571, 1995.
- [22] I. H. Ho and G. B. Stringfellow, "Solubility of nitrogen in binary III-V systems," *Journal of Crystal Growth*, vol. 178, pp. 1 – 7, June 1997.
- [23] S. G. Spruytte, M. C. Larson, W. Wampler, C. W. Coldren, H. E. Petersen, and J. S. Harris, "Nitrogen incorporation in group III-nitride-arsenide materials grown by elemental source molecular beam epitaxy," *Journal of Crystal Growth*, vol. 227-228, pp. 506 – 515, 2001.

- [24] W. Stolz, "Alternative N-, P- and As-precursors for III/V-epitaxy," *Journal of Crystal Growth*, vol. 209, no. 2, pp. 272–278, 2000.
- [25] A. Hasse, K. Volz, A. K. Schaper, J. Koch, F. Höhnsdorf, and W. Stolz, "TEM Investigations of (GaIn)(NAs)/GaAs Multi-Quantum Wells grown by MOVPE," *Crystal Research and Technology*, vol. 35, no. 2000, p. 787, 2000.
- [26] M. Kawaguchi, T. Miyamoto, E. Gouardes, D. Schlenker, T. Kondo, F. Koyama, and K. Iga, "Lasing Characteristics of Low-Threshold GaInNAs Lasers Grown by Metalorganic Chemical Vapor Deposition," *Japanese Journal of Applied Physics*, vol. 40, pp. L744 – L746, 2001.
- [27] Z. Pan, T. Miyamoto, D. Schlenker, S. Sato, F. Koyama, and K. Iga, "Low temperature growth of GaInNAs/GaAs quantum wells by metalorganic chemical vapor deposition using tertiarybutylarsine," *Journal of Applied Physics*, vol. 84, no. 11, pp. 6409 – 6411, 1998.
- [28] S. G. Spruytte, C. W. Coldren, A. F. Marshall, M. C. Larson, and J. S. Harris, "MBE Growth of Nitride-Arsenide Materials for Long Wavelength Optoelectronics," *Spring MRS meeting*, vol. 5S1, p. W8.4, 2000.
- [29] M. A. Wistey, S. R. Bank, H. B. Yuen, H. Bae, J. S. H., and Jr, "Nitrogen plasma optimization for high-quality dilute nitrides," *Journal of Crystal Growth*, vol. 278, no. 1-4, pp. 229 – 233, 2005. 13th International Conference on Molecular Beam Epitaxy.
- [30] G. Adolfsson, W. Shumin, M. Sadeghi, J. Bengtsson, A. Larsson, J. L. Jun, V. Vilokinen, and P. Melanen, "Effects of Lateral Diffusion on the Temperature Sensitivity of the Threshold Current for 1.3- μm Double Quantum-Well GaInNAsGaAs Lasers," *Quantum Electronics, IEEE Journal of*, vol. 44, no. 7, pp. 607 – 616, 2008.
- [31] M. Hopkinson, C. Y. Jin, H. Y. Liu, P. Navaretti, and R. Airey, "1.34 μm GaInNAs quantum well lasers with low room-temperature threshold current density," *Electronics Letters*, vol. 42, no. 16, pp. 923 – 924, 2006.

- [32] J. Kasai, T. Kitatani, K. Adachi, K. Nakahara, and M. Aoki, "Growth of low-threshold GaInNAs/GaAs triple-quantum-well lasers," *Journal of Crystal Growth*, vol. 301-302, pp. 545 – 547, 2007. 14th International Conference on Molecular Beam Epitaxy - MBE XIV.
- [33] Y. Q. Wei, M. Sadeghi, S. M. Wang, P. Modh, and A. Larsson, "High performance 1.28 μm GaInNAs double quantum well lasers," *Electronics Letters*, vol. 41, no. 24, pp. 1328 – 1330, 2005.
- [34] D. Gollub, S. Moses, and A. Forchel, "Comparison of GaInNAs laser diodes based on two to five quantum wells," *Quantum Electronics, IEEE Journal of*, vol. 40, no. 4, pp. 337 – 342, 2004.
- [35] N. Tansu, N. J. Kirsch, and L. J. Mawst, "Low-threshold-current-density 1300-nm dilute-nitride quantum well lasers," *Applied Physics Letters*, vol. 81, no. 14, pp. 2523 – 2525, 2002.
- [36] S. Sato and S. Satoh, "High-temperature characteristic in 1.3- μm -range highly strained GaInNAs ridge stripe lasers grown by metal-organic chemical vapor deposition," *Photonics Technology Letters, IEEE*, vol. 11, no. 12, pp. 1560 – 1562, 1999.
- [37] M. R. Gokhale, P. V. Studenkov, J. Wei, and S. R. Forrest, "Low-threshold current, high-efficiency 1.3- μm wavelength aluminum-free InGaAsN-based quantum-well lasers," *Photonics Technology Letters, IEEE*, vol. 12, no. 2, pp. 131 – 133, 2000.
- [38] C. S. Peng, T. Jouhti, P. Laukkanen, E.-M. Pavelescu, J. Konttinen, W. Li, and M. Pessa, "1.32- μm GaInNAs-GaAs laser with a low threshold current density," *Photonics Technology Letters, IEEE*, vol. 14, no. 3, pp. 275 – 277, 2002.
- [39] Y. Wei, J. S. Gustavsson, M. Sadeghi, S. Wang, A. Larsson, P. Savolainen, P. Melanen, and P. Sipilä, "Uncooled 2.5 Gb/s operation of 1.3 μm GaInNAs DQW lasers over a wide temperature range," *Optics Express*, vol. 14, no. 7, pp. 2753 – 2759, 2006.

- [40] D. Bisping, D. Pucicki, S. Hofling, S. Habermann, D. Ewert, M. Fischer, J. Koeth, and A. Forchel, "High-Temperature High-Power Operation of GaInNAs Laser Diodes in the 1220-1240-nm Wavelength Range," *Photonics Technology Letters, IEEE*, vol. 20, no. 21, pp. 1766 – 1768, 2008.
- [41] M. C. Larson, C. W. Coldren, S. G. Spruytte, H. E. Petersen, and J. S. Harris, "Low-threshold oxide-confined GaInNAs long wavelength vertical cavity lasers," *Photonics Technology Letters, IEEE*, vol. 12, no. 12, pp. 1598 – 1600, 2000.
- [42] A. W. Jackson, R. L. Naone, M. J. Dalberth, J. M. Smith, K. J. Malone, D. W. Kisker, J. F. Klem, K. D. Choquette, D. K. Serkland, and K. M. Geib, "OC-48 capable InGaAsN vertical cavity lasers," *Electronics Letters*, vol. 37, no. 6, pp. 355 – 356, 2001.
- [43] Y. Onishi, N. Saga, K. Koyama, H. Doi, T. Ishizuka, T. Yamada, K. Fujii, H. Mori, J. Hashimoto, M. Shimazu, and T. Katsuyama, "High power and low resistive GaInNAs-VCSELs with buried tunnel junctions," *International Semiconductor Laser Conference*, p. TuB2, 2009.
- [44] C. S. Murray, F. D. Newman, S. Sun, J. B. Clevenger, D. J. Bossert, C. X. Wang, H. Q. Hou, and R. A. Stall, "Development of 1.3 μ m oxide-confined VCSELs grown by MOCVD," *Proceedings of SPIE*, vol. 4649, pp. 31 – 38, 2002.
- [45] T. Takeuchi, Y.-L. Chang, M. Leary, A. Tandon, H.-C. Luan, D. Bour, S. Corzine, R. Twist, and M. Tan, "1.3 μ m InGaAsN vertical cavity surface emitting lasers grown by MOCVD," *Electronics Letters*, vol. 38, no. 23, pp. 1438 – 1440, 2002.
- [46] A. Yue, K. Shen, R. Wang, and J. Shi, "Low threshold current 1.3- μ m GaInNAs VCSELs grown by MOVPE," *Photonics Technology Letters, IEEE*, vol. 16, no. 3, pp. 717 – 719, 2004.
- [47] R. H. Johnson, V. Blasingame, J. A. Tatum, B.-S. Chen, D. T. Mathes, J. D. Orenstein, T.-Y. Wang, J. K. Kim, H.-K. Kwon, J.-H. Ryou, G. Park,

- E. Kalweit, H. Chanhvongsak, M. D. Ringle, T. Marta, and J. Gieske, "Long-wavelength VCSELs at Honeywell," *Vertical-Cavity Surface-Emitting Lasers VII*, vol. 4994, no. 1, pp. 222 – 234, 2003.
- [48] S. R. Prakash, L. M. F. Chirovsky, R. L. Naone, D. Galt, D. W. Kisker, and A. W. Jackson, "Reliability of 1.3 micron VCSELs for metro area networks," *Proceedings of SPIE*, vol. 4994, pp. 44 – 54, 2003.
- [49] H. Shimizu, C. Setiagung, M. Ariga, Y. Ikenaga, K. Kumada, T. Hama, N. Ueda, N. Iwai, and A. Kasukawa, "1.3- μm -range GaInNAsSb-GaAs VCSELs," *Selected Topics in Quantum Electronics, IEEE Journal of*, vol. 9, no. 5, pp. 1214 – 1219, 2003.
- [50] D. A. Louderback, M. A. Fish, J. F. Klem, D. K. Serkland, K. D. Choquette, G. W. Pickrell, R. V. Stone, and P. S. Guilfoyle, "Development of bottom-emitting 1300-nm vertical-cavity surface-emitting lasers," *Photonics Technology Letters, IEEE*, vol. 16, no. 4, pp. 963 – 965, 2004.
- [51] S. R. Bank, M. A. Wistey, L. L. Goddard, H. B. Yuen, V. Lordi, and J. S. Harris, "Low Threshold, Continuous Wave, 1.5 μm GaInNAsSb Lasers Grown on GaAs," *IEEE Journal of Quantum Electronics*, vol. 40, no. 6, pp. 656 – 664, 2004.
- [52] S. R. Bank, B. Hopil, L. L. Goddard, H. B. Yuen, M. A. Wistey, R. Kudrawiec, and J. S. Harris, "Recent Progress on 1.55- μm Dilute-Nitride Lasers," *Quantum Electronics, IEEE Journal of*, vol. 43, no. 9, pp. 773 – 785, 2007.
- [53] M. A. Wistey, S. R. Bank, H. B. Yuen, L. L. Goddard, and J. S. Harris, "Monolithic, GaInNAsSb VCSELs at 1.46 μm on GaAs by MBE," *Electronics Letters*, vol. 39, no. 25, pp. 1822 – 1823, 2003.
- [54] M. A. Wistey, S. R. Bank, H. P. Bae, H. B. Yuen, E. R. Pickett, L. L. Goddard, and J. S. Harris, "GaInNAsSb/GaAs vertical cavity surface emitting lasers at 1534[emsp4 1/4-em space]nm," *Electronics Letters*, vol. 42, no. 5, pp. 282 – 283, 2006.

- [55] L. L. Goddard, *Characterization and Modeling of the Intrinsic Properties of 1.5 μ m GaInNAsSb/GaAs Lasers*. PhD thesis, Stanford University, 2005.
- [56] M. A. Wistey, *Growth of 1.5 μ m GaInNAsSb Vertical Cavity Surface Emitting Lasers by Molecular Beam Epitaxy*. PhD thesis, Stanford University, 2004.
- [57] S. R. Bank, *High-performance 1.55 μ m GaInNAsSb lasers grown on GaAs*. PhD thesis, Stanford University, 2006.
- [58] H. Yuen, *Growth And Characterization of Dilute Nitride Antimonides for Long-Wavelength Optoelectronics*. PhD thesis, Stanford University, 2006.
- [59] V. Gambin, *Long Wavelength Luminescence from GaInNAsSb on GaAs*. PhD thesis, Stanford University, 2002.
- [60] J. R. Arthur, "Interaction of Ga and As₂ Molecular Beams with GaAs Surfaces," *Journal of Applied Physics*, vol. 39, no. 8, pp. 4032 – 4034, 1968.
- [61] A. Polimeni, H. G. Baldassarri, H. M. Bissiri, M. Capizzi, M. Fischer, M. Reinhardt, and A. Forchel, "Effect of hydrogen on the electronic properties of *In_xGa_{1-x}As_{1-y}N_y/GaAs* quantum wells," *Phys. Rev. B*, vol. 63, no. 20, p. 201304, 2001.
- [62] I. A. Buyanova, M. Izadifard, W. M. Chen, A. Polimeni, M. Capizzi, H. P. Xin, and C. W. Tu, "Hydrogen-induced improvements in optical quality of GaNAs alloys," *Applied Physics Letters*, vol. 82, pp. 3662 – 3664, 2003.
- [63] A. J. Ptak, S. W. Johnston, S. Kurtz, D. J. Friedman, and W. K. Metzger, "A comparison of MBE- and MOCVD-grown GaInNAs," *Journal of Crystal Growth*, vol. 251, no. 1 - 4, pp. 392 – 398, 2003. Proceedings of the Twelfth International Conference on Molecular Beam Epitaxy.
- [64] J. A. Gupta, P. J. Barrios, G. J. Pakulski, G. C. Aers, J. A. Caballero, D. Poitras, and X. Wu, "Properties of GaInNAsSb narrow ridge waveguide laser diodes in continuous-wave operation at 1.55 μ m," *Novel In-Plane Semiconductor Lasers VI*, vol. 6485, no. 1, p. 64850S, 2007.

- [65] Y. Fedorenko, T. Jouhti, E.-M. Pavelescu, S. Karirinne, J. Kontinnen, and M. Pessa, "Optimisation of growth temperature and post-growth annealing for GaInNAs/GaNAs/GaAs quantum-well structures emitting at 1.3 μm ," *Thin Solid Films*, vol. 440, no. 1-2, pp. 195 – 197, 2003.
- [66] M. Fischer, M. Reinhardt, and A. Forchel, "GaInAsN/GaAs laser diodes operating at 1.52 μm ," *Electronics Letters*, vol. 36, no. 14, pp. 1208 – 1209, 2000.
- [67] C. W. Coldren, M. C. Larson, S. G. Spruytte, and J. S. Harris, "1200 nm GaAs-based vertical cavity lasers employing GaInNAs multiquantum well active regions," *Electronics Letters*, vol. 36, no. 11, pp. 951 – 952, 2000.
- [68] W. C. Hughes, W. H. R. Jr, M. A. L. Johnson, S. Fujita, J. W. C. Jr, J. F. Schetzina, J. Ren, and J. A. Edmond, "Molecular beam epitaxy growth and properties of GaN films on GaN/SiC substrates," vol. 13, pp. 1571 – 1577, AVS, 1995.
- [69] A. E. Zhukov, R. Zhao, P. Specht, V. M. Ustinov, A. Anders, and E. R. Weber, "MBE growth of (In)GaAsN on GaAs using a constricted DC plasma source," *Semiconductor Science and Technology*, vol. 16, no. 5, pp. 413 – 419, 2001.
- [70] H. B. Yuen, M. A. Wistey, S. R. Bank, H. Bae, and J. S. H. Jr, "Investigation of nitrogen flow variation into a radio frequency plasma cell on plasma properties and GaInNAs grown by molecular beam epitaxy," vol. 23, pp. 1328 – 1332, AVS, 2005.
- [71] P. Jin, S. H. Pan, Y. G. Li, C. Z. Zhang, and Z. G. Wang, "A comparison between contactless electroreflectance and photorefectance spectra from n-doped GaAs on a semi-insulating GaAs substrate," *Semiconductor Science and Technology*, vol. 21, no. 10, pp. 1467 – 1471, 2006.
- [72] T. Kageyama, T. Miyamoto, S. Makino, F. Koyama, and K. Iga, "Thermal Annealing of GaInNAs/GaAs Quantum Wells Grown by Chemical Beam Epitaxy and Its Effect on Photoluminescence," *Japanese Journal of Applied Physics*, vol. 38, no. Part 2, No. 3B, pp. L298 – L300, 1999.

- [73] P. Krispin, V. Gambin, J. S. Harris, and K. H. Ploog, “Nitrogen-related electron traps in Ga(As,N) layers (<3Physics, vol. 93, pp. 6095–6099, 2003.
- [74] P. Krispin, S. G. Spruytte, J. S. Harris, and K. H. Ploog, “Origin and annealing of deep-level defects in p-type GaAs/Ga(As,N)/GaAs heterostructures grown by molecular beam epitaxy,” *Journal of Applied Physics*, vol. 89, pp. 6294 – 6298, 2001.
- [75] M. Ramsteiner, D. S. Jiang, J. S. Harris, and K. H. Ploog, “Nonradiative recombination centers in Ga(As,N) and their annealing behavior studied by Raman spectroscopy,” *Applied Physics Letters*, vol. 84, no. 11, pp. 1859 – 1861, 2004.
- [76] S. R. Bank, H. B. Yuen, H. Bae, M. A. Wistey, A. Moto, and J. S. Harris, “Enhanced luminescence in GaInNAsSb quantum wells through variation of the arsenic and antimony fluxes,” *Applied Physics Letters*, vol. 88, no. 24, p. 241923, 2006.
- [77] G. Mussler, J.-M. Chauveau, A. Trampert, M. Ramsteiner, L. Däweritz, and K. H. Ploog, “Nitrogen-dependent optimum annealing temperature of Ga(As,N),” *Journal of Crystal Growth*, vol. 267, no. 1-2, pp. 60 – 66, 2004.
- [78] J. S. Harris, “GaInNAs long-wavelength lasers: progress and challenges,” *Semiconductor Science and Technology*, vol. 17, no. 8, pp. 880 – 891, 2002.
- [79] E.-M. Pavelescu, T. Jouhti, C. S. Peng, W. Li, J. Konttinen, M. Dumitrescu, P. Laukkanen, and M. Pessa, “Enhanced optical performances of strain-compensated 1.3- μm GaInNAs/GaNAs/GaAs quantum-well structures,” *Journal of Crystal Growth*, vol. 241, no. 1-2, pp. 31 – 38, 2002.
- [80] E.-M. Pavelescu, C. S. Peng, T. Jouhti, J. Konttinen, W. Li, M. Pessa, M. Dumitrescu, and S. Spânulescu, “Effects of insertion of strain-mediating layers on luminescence properties of 1.3- μm GaInNAs/GaNAs/GaAs quantum-well structures,” *Applied Physics Letters*, vol. 80, no. 17, pp. 3054 – 3056, 2002.

- [81] L. Wei, M. Pessa, T. Ahlgren, and J. Decker, "Origin of improved luminescence efficiency after annealing of Ga(In)NAs materials grown by molecular-beam epitaxy," *Applied Physics Letters*, vol. 79, pp. 1094 – 1096, 2001.
- [82] S. Kurtz, J. F. Geisz, D. J. Friedman, W. K. Metzger, R. R. King, and N. H. Karam, "Annealing-induced-type conversion of GaInNAs," *Journal of Applied Physics*, vol. 95, no. 5, pp. 2505 – 2508, 2004.
- [83] A. Janotti, S.-H. Wei, S. B. Zhang, S. Kurtz, and C. G. van de Walle, "Interactions between nitrogen, hydrogen, and gallium vacancies in GaAs_{1-x}N_x alloys," *Physical Review B*, vol. 67, no. 16, p. 161201, 2003.
- [84] A. J. Ptak, S. Kurtz, M. H. Weber, and K. G. Lynn, "Positron annihilation study of vacancies in GaInNAs," *Journal of Vacuum Science & Technology B: Microelectronics and Nanometer Structures*, vol. 22, no. 3, pp. 1584 – 1587, 2004.
- [85] V. Lordi, V. Gambin, S. Friedrich, T. Funk, T. Takizawa, K. Uno, and J. S. Harris, "Nearest-Neighbor Configuration in (GaIn)(NAs) Probed by X-Ray Absorption Spectroscopy," *Physical Review Letters*, vol. 90, no. 14, p. 145505, 2003.
- [86] S. Kurtz, J. Webb, L. Gedvilas, D. Friedman, J. Geisz, J. Olson, R. King, D. Joslin, and N. Karam, "Structural changes during annealing of GaInAsN," *Applied Physics Letters*, vol. 78, no. 6, pp. 748 – 750, 2001.
- [87] J. L. Harris, A. C. Bryce, O. Kowalski, J. Marsh, T. Jouhti, M. Pessa, and M. Hopkinson, "Selective quantum well intermixing of 1.22 and 1.55 μ m GaInNAs laser material," in *Conference on Lasers and Electro-Optics/International Quantum Electronics Conference and Photonic Applications Systems Technologies*, p. CTuJ7, Optical Society of America, 2004.
- [88] R. Macaluso, H. D. Sun, M. D. Dawson, F. Robert, A. C. Bryce, J. H. Marsh, and H. Riechert, "Selective modification of band gap in GaInNAs/GaAs structures by quantum-well intermixing," *Applied Physics Letters*, vol. 82, no. 24, pp. 4259 – 4261, 2003.

- [89] O. M. Khreis, W. P. Gillin, and K. P. Homewood, "Interdiffusion: A probe of vacancy diffusion in III-V materials," *Physical Review B*, vol. 55, pp. 15813 – 15818, 1997.
- [90] J. Massies and N. Grandjean, "Surfactant effect on the surface diffusion length in epitaxial growth," *Phys. Rev. B*, vol. 48, no. 11, pp. 8502 – 8505, 1993.
- [91] K. Volz, V. Gambin, W. Ha, M. A. Wistey, H. Yuen, S. Bank, and J. S. Harris, "The role of Sb in the MBE growth of (GaIn)(NAsSb)," *Journal of Crystal Growth*, vol. 251, no. 1-4, pp. 360 – 366, 2003. Proceedings of the Twelfth International Conference on Molecular Beam Epitaxy.
- [92] H. B. Yuen, S. R. Bank, M. A. Wistey, J. S. H. Jr, and A. Moto, "Comparison of GaNAsSb and GaNAs as quantum-well barriers for GaInNAsSb optoelectronic devices operating at 1.3–1.55 μm ," *Journal of Applied Physics*, vol. 96, no. 11, pp. 6375 – 6381, 2004.
- [93] H. B. Yuen, S. R. Bank, H. Bae, M. A. Wistey, and J. S. H. Jr, "The role of antimony on properties of widely varying GaInNAsSb compositions," *Journal of Applied Physics*, vol. 99, no. 9, p. 093504, 2006.
- [94] A. Y. Egorov, D. Bernklau, B. Borchert, S. Illek, D. Livshits, A. Rucki, M. Schuster, A. Kaschner, A. Hoffmann, G. Dumitras, M. C. Amann, and H. Riechert, "Growth of high quality InGaAsN heterostructures and their laser application," *Journal of Crystal Growth*, vol. 227-228, pp. 545 – 552, 2001.
- [95] T. Sarmiento, H. Bae, T. D. O'Sullivan, and J. S. Harris, "1528 nm GaInNAsSb/GaAs Vertical Cavity Surface Emitting Lasers," *Conference on Lasers and Electro-Optics*, p. CTuY4, 2009.
- [96] W. Ha, V. Gambin, S. Bank, M. Wistey, H. Yuen, K. Seongsin, and J. S. J. Harris, "Long-wavelength GaInNAs(Sb) lasers on GaAs," *Quantum Electronics, IEEE Journal of*, vol. 38, no. 9, pp. 1260 – 1267, 2002.

- [97] J. S. Wang, A. R. Kovsh, L. Wei, J. Y. Chi, Y. T. Wu, P. Y. Wang, and V. M. Ustinov, "MBE growth of high-quality GaAsN bulk layers," *Nanotechnology*, vol. 12, pp. 430 – 433, 2001.
- [98] M. A. Wistey, S. R. Bank, H. B. Yuen, J. S. H. Jr, M. M. Oye, and A. L. H. Jr, "Using beam flux monitor as Langmuir probe for plasma-assisted molecular beam epitaxy," *Journal of Vacuum Science & Technology A: Vacuum, Surfaces, and Films*, vol. 23, no. 3, pp. 460 – 464, 2005.
- [99] M. A. Wistey, S. R. Bank, H. B. Yuen, L. L. Goddard, T. Gugov, and J. S. H. Jr, "Protecting wafer surface during plasma ignition using an arsenic cap," vol. 23, pp. 1324 – 1327, AVS, 2005.
- [100] A. Y. Cho, "Growth of III-V semiconductors by molecular beam epitaxy and their properties," *Thin Solid Films*, vol. 100, no. 4, pp. 291–317, 1983.
- [101] D. L. Smith and V. Y. Pickhardt, "Molecular beam epitaxy of II-VI compounds," *Journal of Applied Physics*, vol. 46, no. 6, pp. 2366–2374, 1975.
- [102] M. Kondow and T. Kitatani, "Molecular beam epitaxy of GaNAs and GaInNAs," *Semiconductor Science and Technology*, vol. 17, no. 8, pp. 746 – 754, 2002.
- [103] *Thermocouples Part 2: Tolerances (IEC 584-2 : 1982 + A1: 1989)*. European Committee for Electrotechnical Standardization, 1993.
- [104] A. J. SpringThorpe, S. J. Ingre, B. Emmerstorfer, P. Mandeville, and W. T. Moore, "Measurement of GaAs surface oxide desorption temperatures," *Applied Physics Letters*, vol. 50, no. 2, pp. 77–79, 1987.
- [105] E. Hellman and J. S. Harris, "Infra-red transmission spectroscopy of GaAs during molecular beam epitaxy," *Journal of Crystal Growth*, vol. 81, pp. 38–42, Feb. 1987.
- [106] J. Hu *Private Communication*, p. Luxtron Corporation.

- [107] D. A. Allwood, P. C. Klipstein, N. J. Mason, R. J. Nicholas, and P. J. Walker, “GaAs high temperature optical constants and application to optical monitoring within the MOVPE environment,” *Journal of Electronic Materials*, vol. 29, no. 1, pp. 99–105, 2000.
- [108] J. S. Blakemore, “Semiconducting and other major properties of gallium arsenide,” *Journal of Applied Physics*, vol. 53, no. 10, pp. R123–R181, 1982.
- [109] E. V. K. Rao, A. Ougazzaden, Y. L. Bellego, and M. Juhel, “Optical properties of low band gap GaAs_(1-x)N_x layers: Influence of post-growth treatments,” *Applied Physics Letters*, vol. 72, no. 12, pp. 1409 – 1411, 1998.
- [110] L. Grenouillet, C. Bru-Chevallier, G. Guillot, P. Gilet, P. Ballet, P. Duvaut, G. Rolland, and A. Million, “Rapid thermal annealing in GaN_xAs_{1-x}/GaAs structures: Effect of nitrogen reorganization on optical properties,” *Journal of Applied Physics*, vol. 91, no. 9, pp. 5902 – 5908, 2002.
- [111] E.-M. Pavelescu, T. Jouhti, M. Dumitrescu, P. J. Klar, S. Karirinne, Y. Fedorenko, and M. Pessa, “Growth-temperature-dependent (self-)annealing-induced blueshift of photoluminescence from 1.3 μ m GaInNAs/GaAs quantum wells,” *Applied Physics Letters*, vol. 83, no. 8, pp. 1497 – 1499, 2003.
- [112] G. Mussler, L. Däweritz, K. H. Ploog, J. W. Tomm, and V. Talalaev, “Optimized annealing conditions identified by analysis of radiative recombination in dilute Ga(As,N),” *Applied Physics Letters*, vol. 83, no. 7, pp. 1343 – 1345, 2003.
- [113] M. Kondow, T. Kitatani, and S. Shirakata, “Annealing in GaInNAs system,” *Journal of Physics: Condensed Matter*, vol. 16, no. 31, pp. S3229 – S3244, 2004.
- [114] H. B. Yuen, S. R. Bank, H. Bae, M. A. Wistey, and J. S. H. Jr, “Effects of strain on the optimal annealing temperature of GaInNAsSb quantum wells,” *Applied Physics Letters*, vol. 88, no. 22, p. 221913, 2006.

- [115] S. Govindaraju, J. M. Reifsnider, M. M. Oye, and A. L. Holmes, “Time and temperature dependence on rapid thermal annealing of molecular beam epitaxy grown Ga_{0.8}In_{0.2}N_{0.01}As_{0.99} quantum wells analyzed using photoluminescence,” *Journal of Electronic Materials*, vol. 32, no. 1, pp. 29 – 33, 2003.
- [116] W. Li, M. Pessa, T. Ahlgren, and J. Decker, “Origin of improved luminescence efficiency after annealing of Ga(In)NAs materials grown by molecular-beam epitaxy,” *Applied Physics Letters*, vol. 79, no. 8, pp. 1094 – 1096, 2001.
- [117] H. F. Liu, V. Dixit, and N. Xiang, “Anneal-induced interdiffusion in 1.3 μ m GaInNAs/GaAs quantum well structures grown by molecular-beam epitaxy,” *Journal of Applied Physics*, vol. 99, no. 1, p. 013503, 2006.
- [118] Y. Qiu, S. A. Nikishin, H. Temkin, V. A. Elyukhin, and Y. A. Kudriavtsev, “Thermodynamic considerations in epitaxial growth of GaAs_{1-x}N_x solid solutions,” *Applied Physics Letters*, vol. 70, no. 21, pp. 2831 – 2833, 1997.
- [119] B. Damilano, J. Barjon, J.-Y. Duboz, J. Massies, A. Hierro, J.-M. Ulloa, and E. Calleja, “Growth and in situ annealing conditions for long-wavelength (Ga, In)(N, As)/GaAs lasers,” *Applied Physics Letters*, vol. 86, no. 7, p. 071105, 2005.
- [120] W. Ha, V. Gambin, M. Wistey, S. Bank, K. Seongsin, and J. S. J. Harris, “Multiple-quantum-well GaInNAs-GaNAs ridge-waveguide laser diodes operating out to 1.4 μ m,” *Photonics Technology Letters, IEEE*, vol. 14, no. 5, pp. 591 – 593, 2002.
- [121] M. Wistey *Private communication*, 2009.
- [122] S. R. Bank, H. B. Yuen, H. Bae, M. A. Wistey, and J. S. H. Jr, “Overannealing effects in GaInNAs(Sb) alloys and their importance to laser applications,” *Applied Physics Letters*, vol. 88, no. 22, p. 221115, 2006.
- [123] W. Shockley and W. T. Read, “Statistics of the Recombinations of Holes and Electrons,” *Phys. Rev.*, vol. 87, no. 5, pp. 835 – 842, 1952.

- [124] R. N. Hall, "Electron-Hole Recombination in Germanium," *Phys. Rev.*, vol. 87, no. 2, p. 387, 1952.
- [125] L. A. Coldren and S. W. Corzine, *Diode lasers and photonic integrated circuits*. John Wiley & Sons, Inc, 1995.
- [126] N. K. Dutta and R. J. Nelson, "The case for Auger recombination in $\text{In}_{1-x}\text{Ga}_x\text{As}_y\text{P}_{1-y}$," *Journal of Applied Physics*, vol. 53, no. 1, pp. 74 – 92, 1982.
- [127] E. P. O'Reilly and M. Silver, "Temperature sensitivity and high temperature operation of long wavelength semiconductor lasers," *Applied Physics Letters*, vol. 63, no. 24, pp. 3318 – 3320, 1993.
- [128] D. A. Neamen, *Semiconductor physics and devices*. Irwin, Inc, 1992.
- [129] H. Schneider and K. Klitzing, "Thermionic emission and Gaussian transport of holes in a $\text{GaAs}/\text{Al}_x\text{Ga}_{1-x}\text{As}$ multiple-quantum-well structure," *Phys. Rev. B*, vol. 38, no. 9, pp. 6160 – 6165, 1988.
- [130] N. Tansu and L. J. Mawst, "Current injection efficiency of InGaAsN quantum-well lasers," *Journal of Applied Physics*, vol. 97, no. 5, p. 054502, 2005.
- [131] S. Adachi, *GaAs and Related Materials*. World Scientific Publishing Co., 1994.
- [132] S. R. Bank, L. L. Goddard, M. A. Wistey, H. B. Yuen, and J. S. J. Harris, "On the temperature sensitivity of 1.5- μm GaInNAsSb lasers," *Selected Topics in Quantum Electronics, IEEE Journal of*, vol. 11, no. 5, pp. 1089 – 1098, 2005.
- [133] J. S. Harris, R. Kudrawiec, H. B. Yuen, S. R. Bank, H. P. Bae, M. A. Wistey, D. Jackrel, E. R. Pickett, T. Sarmiento, L. L. Goddard, V. Lordi, and T. Gugov, "Development of GaInNAsSb alloys: Growth, band structure, optical properties and applications," *Physica Status Solidi (b)*, vol. 244, no. 8, pp. 2707 – 2729, 2007.
- [134] S. L. Chuang, *Physics of Optoelectronic Devices*. John Wiley & Sons, 1995.

- [135] R. Fehse, S. Tomic, A. R. Adams, S. J. Sweeney, E. P. O'Reilly, A. Andreev, and H. Riechert, "A quantitative study of radiative, Auger, and defect related recombination processes in 1.3- μm GaInNAs-based quantum-well lasers," *Selected Topics in Quantum Electronics, IEEE Journal of*, vol. 8, no. 4, pp. 801 – 810, 2002.
- [136] A. Haug, "Relations between the T_0 values of bulk and quantum-well GaAs," *Applied Physics B*, vol. 44, no. 3, pp. 151 – 153, 1987.
- [137] S. R. Bank, M. A. Wistey, L. L. Goddard, H. B. Yuen, H. P. Bae, and J. S. Harris, "High-Performance 1.5 μm GaInNAsSb Lasers on GaAs," *Electronics Letters*, vol. 40, no. 19, pp. 1186 – 1187, 2004.
- [138] P. Blood, G. M. Lewis, P. M. Snowton, H. Summers, J. Thomson, and J. Lutti, "Characterization of semiconductor laser gain media by the segmented contact method," *Selected Topics in Quantum Electronics, IEEE Journal of*, vol. 9, no. 5, pp. 1275 – 1282, 2003.
- [139] J. W. Ferguson, P. M. Snowton, P. Blood, H. Bae, T. Sarmiento, and J. S. Harris, "Origin of Non Radiative recombination in GaInNAsSb/GaNAs Quantum Well Lasers," *submitted to Conference on Lasers and Electro-Optics (CLEO)*, 2009.
- [140] J. Ferguson *Private communication*, 2008.
- [141] H. B. Yuen, S. R. Bank, M. A. Wistey, J. S. H. Jr, M.-J. Seong, S. Yoon, R. Kudrawiec, and J. Misiewicz, "Improved optical quality of GaNAsSb in the dilute Sb limit," *Journal of Applied Physics*, vol. 97, no. 11, p. 113510, 2005.
- [142] T. Asano, D. Feezell, R. Koda, M. H. M. Reddy, D. A. Buell, A. S. Huntington, E. Hall, S. Nakagawa, and L. A. Coldren, "InP-based all-epitaxial 1.3- μm VCSELs with selectively etched AlInAs apertures and Sb-based DBRs," *Photonics Technology Letters, IEEE*, vol. 15, no. 10, pp. 1333 – 1335, 2003.

- [143] L. Goldstein, C. Fortin, C. Starck, A. Plais, J. Jacquet, J. Boucart, A. Rocher, and C. Poussou, "GaAlAs/GaAs metamorphic Bragg mirror for long wavelength VCSELs," *Electronics Letters*, vol. 34, no. 3, pp. 268 – 270, 1998.
- [144] M. C. Larson, M. Kondow, T. Kitatani, K. Nakahara, K. Tamura, H. Inoue, and K. Uomi, "GaInNAs-GaAs long-wavelength vertical-cavity surface-emitting laser diodes," *Photonics Technology Letters, IEEE*, vol. 10, no. 2, pp. 188 – 190, 1998.
- [145] G. Steinle, F. Mederer, M. Kicherer, R. Michalzik, G. Kristen, A. Y. Egorov, H. Riechert, H. D. Wolf, and K. J. Ebeling, "Data transmission up to 10 Gbit/s with 1.3 μm wavelength InGaAsN VCSELs," *Electronics Letters*, vol. 37, no. 10, pp. 632 – 634, 2001.
- [146] A. Ramakrishnan, G. Steinle, D. Supper, C. Degen, and G. Ebbinghaus, "Electrically pumped 10 Gbit/s MOVPE-grown monolithic 1.3 μm VCSEL with GaInNAs active region," *Electronics Letters*, vol. 38, no. 7, pp. 322 – 324, 2002.
- [147] X. Yang, M. J. Jurkovic, J. B. Heroux, and W. I. Wang, "Molecular beam epitaxial growth of InGaAsN:Sb/GaAs quantum wells for long-wavelength semiconductor lasers," *Applied Physics Letters*, vol. 75, p. 178, 1999.
- [148] H. Bae, T. Sarmiento, and J. S. Harris, "Experimental investigation of temperature dependence of 1.55 μm GaInNAsSb/GaNAs QW lasers grown in MBE," *ISLC*, pp. 59 – 60, 2008.
- [149] S. F. Yu, "Analysis and Design of Vertical Cavity Surface Emitting Lasers," 2003.
- [150] D. L. Huffaker, D. G. Deppe, K. Kumar, and T. J. Rogers, "Native-oxide defined ring contact for low threshold vertical-cavity lasers," *Applied Physics Letters*, vol. 65, no. 1, pp. 97 – 99, 1994.
- [151] J. M. Dallesasse, N. H. Jr, A. R. Sugg, T. A. Richard, and N. El-Zein, "Hydrolyzation oxidation of $\text{Al}_x\text{Ga}_{1-x}\text{As}$ -AlAs-GaAs quantum well heterostructures

- and superlattices,” *Applied Physics Letters*, vol. 57, no. 26, pp. 2844 – 2846, 1990.
- [152] E. R. Hegblom, D. I. Babic, B. J. Thibeault, and L. A. Coldren, “Scattering losses from dielectric apertures in vertical-cavity lasers,” *Selected Topics in Quantum Electronics, IEEE Journal of*, vol. 3, no. 2, pp. 379 – 389, 1997.
- [153] C. Henry, R. Logan, F. Merritt, and J. Luongo, “The effect of intervalence band absorption on the thermal behavior of InGaAsP lasers,” *Quantum Electronics, IEEE Journal of*, vol. 19, no. 6, pp. 947 – 952, 1983.
- [154] L. R. Thompson, L. M. F. Chirovsky, A. W. Jackson, R. L. Naone, D. Galt, S. R. Prakash, S. A. Feld, M. V. Crom, J. G. Wasserbauer, M. D. Lange, B. Mayer, and D. W. Kisker, “Performance of monolithic 1.3 μm VCSELs in telecom applications,” *Proceedings of SPIE*, vol. 4649, pp. 25 – 30, 2002.
- [155] K. D. Choquette, J. F. Klem, A. J. Fischer, O. Blum, A. A. Allerman, I. J. Fritz, S. R. Kurtz, W. G. Breiland, R. Sieg, K. M. Geib, J. W. Scott, and R. L. Naone, “Room temperature continuous wave InGaAsN quantum well vertical-cavity lasers emitting at 1.3 μm ,” *Electronics Letters*, vol. 36, no. 16, pp. 1388 – 1390, 2000.
- [156] E. F. Schubert, L. W. Tu, G. J. Zyzdik, R. F. Kopf, A. Benvenuti, and M. R. Pinto, “Elimination of heterojunction band discontinuities by modulation doping,” *Applied Physics Letters*, vol. 60, no. 4, pp. 466 – 468, 1992.
- [157] R. F. Kopf, E. F. Schubert, S. W. Downey, and A. B. Emerson, “N- and P-type dopant profiles in distributed Bragg reflector structures and their effect on resistance,” *Applied Physics Letters*, vol. 61, no. 15, pp. 1820 – 1822, 1992.
- [158] M. G. Peters, B. J. Thibeault, D. B. Young, A. C. Gossard, and L. A. Coldren, “Growth of beryllium doped $\text{Al}_x\text{Ga}_{1-x}\text{As}/\text{GaAs}$ mirrors for vertical-cavity surface-emitting lasers,” *Journal of Vacuum Science & Technology B: Microelectronics and Nanometer Structures*, vol. 12, no. 6, pp. 3075 – 3083, 1994.

- [159] D. W. Winston and R. E. Hayes, "Optoelectronic device simulation of Bragg reflectors and their influence on surface-emitting laser characteristics," *Quantum Electronics, IEEE Journal of*, vol. 34, no. 4, pp. 707 – 715, 1998.
- [160] K. D. Choquette, K. M. Geib, C. I. H. Ashby, R. D. Twesten, O. Blum, H. Q. Hou, D. M. Follstaedt, B. E. Hammons, D. Mathes, and R. Hull, "Advances in selective wet oxidation of AlGaAs alloys," *Selected Topics in Quantum Electronics, IEEE Journal of*, vol. 3, no. 3, pp. 916 – 926, 1997.
- [161] E. R. Hegblom, B. J. Thibeault, R. L. Naone, and L. A. Coldren, "Vertical cavity lasers with tapered oxide apertures for low scattering loss," *Electronics Letters*, vol. 33, no. 10, pp. 869 – 871, 1997.
- [162] D. G. Schlom, W. S. Lee, T. Ma, and J. S. Harris, "Reduction of gallium-related oval defects," *Journal of Vacuum Science & Technology B: Microelectronics and Nanometer Structures*, vol. 7, no. 2, pp. 296 – 298, 1989.